

Electrical gating effects on the magnetic properties of (Ga,Mn)As diluted magnetic semiconductors



Man Hon Samuel Owen

Department of Physics

University of Cambridge

A dissertation submitted for the degree of

Doctor of Philosophy

Churchill College, September 2010

To my family

'... in Him all things hold together.'

- Colossians 1:17

ABSTRACT

Electrical gating effects on the magnetic properties of (Ga,Mn)As diluted magnetic semiconductors

by Man Hon Samuel Owen

The aim of the research project presented in this thesis is to investigate the effects of electrostatic gating on the magnetic properties of carrier-mediated ferromagnetic $\text{Ga}_{1-x}\text{Mn}_x\text{As}$ diluted magnetic semiconductors. (Ga,Mn)As can be regarded as a prototype material because of its strong spin-orbit coupling and its crystalline properties which can be described within a simple band structure model. Compressively strained (Ga,Mn)As epilayer with more complex in-plane competing cubic and uniaxial magnetic anisotropies is of particular interest since a small variation of these competing anisotropy fields provide a means for the manipulation of its magnetization via external electric field.

An all-semiconductor epitaxial p-n junction field-effect transistor (FET) based on low-doped $\text{Ga}_{0.975}\text{Mn}_{0.025}\text{As}$ was fabricated. It has an in-built n-GaAs back-gate, which, in addition to being a normal gate, enhances the gating effects, especially in the depletion of the epilayer, by decreasing the effective channel thickness by means of a depletion region. A shift in the Curie temperature of ~ 2 K and enhanced anisotropic magnetoresistance (AMR) (which at saturation reaches $\sim 30\%$) is achieved with a depletion of a few volts. Persistent magnetization switchings with short electric field pulses are also observed. The magnitude of the switching field is found to decrease with increasing depletion of the (Ga,Mn)As layer. By employing the $\mathbf{k} \cdot \mathbf{p}$ semiconductor theory approach (performed by our collaborators in Institute of Physics, ASCR, Prague), including strong spin-orbit coupling effects in the host semiconductor valence band, a change in sign of K_c at hole density of approximately $1.5 \times 10^{20} \text{ cm}^{-3}$ is observed. Below this density, the $[110]/[1\bar{1}0]$ magnetization directions are favoured, consistent with experimental data.

A double-gated FET, with an ionic-gel top-gate coupled with a p-n junction back-gate based on the same material, was also employed in an attempt to achieve larger effects through gating. It reaffirms the results obtained and demonstrates enhanced gating effects on the magnetic properties of (Ga,Mn)As.

Contents

1	Introduction	1
2	Background	4
2.1	(Ga,Mn)As and its properties	4
2.1.1	Elemental structure of (Ga,Mn)As	5
2.1.2	Defects in (Ga,Mn)As	5
	Interstitial Mn	7
	As antisites	7
2.1.3	Post-growth annealing	8
2.2	Carrier-mediated ferromagnetism	8
2.2.1	Exchange interactions	9
	Direct exchange	9
	Kramer's superexchange	9
	Zener's double exchange	10
	Zener's indirect exchange	10
2.2.2	Qualitative picture of ferromagnetism	12
2.3	Magnetic anisotropy	13
2.3.1	Effects of strain on magnetic anisotropy	14
2.3.2	Effects of hole density on magnetic anisotropy and Curie temperature	17
2.3.3	Magnetocrystalline anisotropy	22
	Uniaxial anisotropy	23
	Cubic anisotropy	24
2.3.4	The Stoner-Wohlfarth Model	24

2.4	Magneto-transport	26
2.4.1	Isotropic Magnetoresistance	26
2.4.2	Anisotropic Magnetoresistance	28
	Phenomenology of AMR	28
	Microscopic Origin of AMR	31
	Experimental studies on AMR in (Ga,Mn)As	33
2.5	Electrical control through gating	37
2.5.1	Field-effect Transistor	37
2.5.2	P-N junction gating	38
	P-I-N Junction	41
2.5.3	Polyelectrolyte gating	42
	Electric double layer	43
	Mechanisms of transistor action	45
	Ionic gel	47
2.6	Curie temperature	48
2.6.1	Curie point singularity in $d\rho/dT$ of (Ga,Mn)As	48
3	Materials and experimental methods	52
3.1	Materials used	53
3.2	Device fabrication	54
3.2.1	Designing the devices	55
3.2.2	Making the device	55
	Optical lithography	57
	Etching	58
	Metal deposition	58
3.2.3	Packaging the device	60
3.2.4	Making the top-gate	60
	Preparation of ionic gel	60
	Top-gate electrode	61
3.3	Measurement methods	62
3.3.1	Cryogenic systems	62

3.3.2	Electrical measurements	63
	Resistance vs. temperature	64
	Magnetic field sweeps	64
	Rotation experiments	65
	Voltage-pulse measurements	65
4	Low-voltage back-gating and oxide removal	67
4.1	Sample structure	68
4.2	Characterization of the FET	69
4.2.1	Leakage current	69
4.2.2	Magnetic characteristics	71
4.3	Temperature and voltage dependence of AMR	74
4.3.1	In-plane magnetic field rotation	74
	Temperature and voltage dependence	75
4.3.2	Perpendicular-to-plane magnetic field rotation	76
4.3.3	In-plane and out-of-plane magnetic field sweeps	78
4.4	Surface oxide etching	80
4.4.1	Channel Resistances	80
4.5	Summary and Conclusions	81
5	Persistent switching by voltage pulses	84
5.1	Device Structure and Simulations	84
5.2	Voltage Control of Curie temperature and magnetoresistance	87
5.3	Persistent Magnetization Switching with Short Voltage Pulse	91
5.4	Theoretical Discussion	93
5.5	Summary and Conclusions	97
6	Double-gating: Ionic gel top-gate in addition to n-type built-in back-gate	99
6.1	Device structure	100
6.2	Ionic gel gating	101
6.3	Channel Resistances and Curie Temperatures	103

6.4	Anisotropic Magnetoresistance	105
6.5	Persistent Switching with voltage pulses	107
6.6	General remarks	116
6.7	Summary and Conclusions	117
7	Conclusions and Future Outlook	118
7.1	Conclusions	118
7.1.1	P-N Junction gating	118
7.1.2	Persistent magnetization reversal with voltage pulses	119
7.1.3	Double-gating	119
7.2	Outlook and Future Work	120
7.2.1	Voltage-pulse magnetization switching	120
7.2.2	Electrolyte-gating	121
A	Fabrication steps	122
A.1	Processes for fabrication of FET	123
A.1.1	Mesa	123
A.1.2	Bond Pads	123
A.1.3	Scribing and Packaging	124
B	Publications	125
	Bibliography	127

Preface

The experimental work presented in this dissertation was performed under the supervision of Prof. Henning Sirringhaus and Dr. Jörg Wunderlich over the period between October 2006 and September 2010 at the Cavendish Laboratory, University of Cambridge, and Hitachi Cambridge Laboratory, for the awarding of the degree of Doctor of Philosophy.

The research has been funded by the following organizations: The Cambridge Commonwealth Trusts, Hitachi Cambridge Laboratory, Churchill College, and Lundgren Research Award (Board of Graduate Studies).

Overview

A general scope of the field of spin electronics, together with the motivation of this work, is presented in Chapter 1. In Chapter 2, a review of the structural and magnetic properties of (Ga,Mn)As, including the origin of ferromagnetism in this material, is given. Background information on p-n junction as well as electrolytes are also presented, providing information on the nature of gating used in the devices measured. In Chapter 3, the materials and experimental methods employed for the fabrication and characterization of the devices under study are discussed. The techniques include standard fabrication processes for the III-V semiconductors, as well as low-temperature transport measurements made with applied magnetic fields.

Preliminary study on an all-semiconductor, epitaxial p-n junction field-effect transistor (FET) is presented in Chapter 4. Introduction of a p-n junction back-gate (as compared to top-gated FET studied previously [1–3]) allows the possibility of large depletion of (Ga,Mn)As thin film at a few volts with the extension of the depletion layer. Device characteristics are measured, with the leakage current through the back-gate being of particular interest. Effects of gating on its anisotropic magnetoresistance (AMR) in both in-plane and out-of-plane magnetic field sweeps, as well as rotation AMR in a saturation magnetic field are investigated. Surface oxide etching procedure is subsequently applied to controllably thin the (Ga,Mn)As layer in a fabricated transistor, resulting in the observation of a further enhancement of the field effect on the channel resistance due to a thinner epilayer channel [4].

Further investigation on the effects of gating on (Ga,Mn)As is carried out in Chapter 5, on an improved wafer, after learning from the initial study in Chapter 4. The improved wafer consists of a 2 nm GaAs protective layer (to protect the (Ga,Mn)As epilayer from unnecessary etching during chemical processing), low-doped $\text{Ga}_{0.975}\text{Mn}_{0.025}\text{As}$ (to provide a larger gating effect) and a graded back-gate barrier (to minimize leakage current) as compared to that used in Chapter 4. A shift in the Curie temperature, T_C , of ~ 2 K and enhanced AMR (which at saturation reaches $\sim 30\%$) is achieved with a depletion of a few volts. Persistent magnetization switchings with short electric field pulses are also shown. The switching fields are found to decrease in magnitude with increasing positive gate voltages (or deple-

tion of the epilayer). Theoretical modelling using the $\mathbf{k} \cdot \mathbf{p}$ semiconductor theory approach, with the consideration of strong spin-orbit coupling effects in the host semiconductor valence band and the zinc-blende crystal structure of GaAs, shows a change in sign of K_c at hole density of approximately $1.5 \times 10^{20} \text{ cm}^{-3}$. Below this density, the $[110]/[1\bar{1}0]$ magnetization directions are favoured, consistent with experimental data [5].

Larger gating effects are desired and this can be realized with the introduction of a double-gated FET in Chapter 6. Ionic-gel top-gate was tested and found to be applicable within a range of $\pm 1 \text{ V}$. Any larger voltages would induce electro-chemical reactions at the interface of the (Ga,Mn)As epilayer and the ionic gel, resulting in a permanent degradation of the epilayer. The results obtained re-affirmed the conclusions made in Chapter 5, since the same wafer is used in both Chapter 5 and 6. Independent gate actions are observed, giving more flexibility to the electrical control since the top-gate can now act as a pre-bias while the back-gate can be used to alter the carrier density in the device in-situ at low temperatures. The combined actions of the two electrical gates also provide enhanced gating effects on the magnetic properties of (Ga,Mn)As when compared with Chapter 5.

Finally, the overall conclusions of this research project are summarized in Chapter 7, together with a proposal of potential future work based on the results obtained.

Declaration

This dissertation is the result of my own work and includes nothing which is the outcome of work done in collaboration except where specifically indicated in the text. It has not been submitted in whole or in part for the award of a degree at this or any other University, and does not exceed 60,000 words in length.

Man Hon Samuel Owen

Churchill College, September 2010

Acknowledgements

Firstly, I would like to thank my supervisors Jörg Wunderlich and Henning Sirringhaus for their great support over the past 4 years. I have always been grateful to Henning for giving me the opportunity to study and research in his research group. This joint project with Hitachi Cambridge Laboratory has given me the chance to work closely with the industry. Jörg has always been a truly inspiring teacher and a friend. His passion for physics is very contagious, and he has been encouraging and patient with me through the difficult times during my PhD research.

My sincere thanks go to the people I have been working with at the Cavendish Laboratory, who have contributed to the completion of my PhD in one way or another. I would like to thank Andy Irvine and Radoslav Chakalov for all their help in the clean room. Radoslav is always the one to look for when there is anything wrong with any of the equipment in the clean room, and Andy is always very kind to give me tips in the fabrication of my devices. Andrew Ferguson, for always being insightful and for his invaluable advice. Hidekazu Kurebayashi, who is a friend and is especially helpful in making his time available for me for any discussion I needed during my time of writing up. Byong-Guk, Janice Jermy and David Williams in Hitachi for always being nice and supportive.

I am thankful for the opportunity I have had to collaborate with the Institute of Physics in Prague. I am most grateful to all the people I worked with, in particular Karel Výborný, Kamil Olejník, Zdenek Výborný, Jan Zemen, Vit Novák and Tomas Jungwirth.

I would also like to thank all the PhD students in the group, who have been there on this journey with me at one stage or another. In particular Elisa, who is always there with her smile when I needed her help and advice. A special thanks goes out to Dong and George, who have had to face me in the office for the past 3 years, listening to all my complaints and who have become my close friends. Another special thanks to Jenny and Mijung, inmates of the Pen with me for all my past 4 years in the laboratory. We have all tunneled through this difficult journey together and I am glad that we have all made it to the end.

I thank also all my friends from outside the lab who have made my life in Cam-

bridge so full and rewarding in between experiments. I would like to thank all my fellow brothers and sisters in the Cambridge Chinese Christian Fellowship for making my time here in Cambridge exciting and enjoyable. And to Joshua, who has been there before me treading the same path, thank you for your friendship during my past 8 years here in Cambridge.

I am also grateful to Churchill College for admitting me for my undergraduate as well as my post-graduate study, without which all these will not be possible. The college has provided me with not only affordable housing but also extra funding for conference travel and my tenth term. Sincere thanks also go to the Cambridge Commonwealth Trusts, Hitachi Cambridge Laboratory, Churchill College, and Lundgren Research Award (Board of Graduate Studies) for funding my PhD and the research I have carried out in the group.

Finally, the biggest thanks goes to my family - my dad, my mum, my sister, my grandma and all of my relatives, for all of their love and continual support, and for providing me with the education which has allowed me to get here. They are the reason for who I am and I love them! Last but not least, I would like to thank God for all his blessings which have made my life in Cambridge an enjoyable one!

Samuel

Chapter 1

Introduction

”One shouldn’t work on semiconductors, that is a filthy mess; who knows whether any semiconductors exist.” This was the opinion of Wolfgang Pauli some seven decades ago [6]. Fast forward to today and we have an array of intricate technology which makes use of these previously bothersome impurities. Their use is indisputably wide ranging – from data storage in computers and communication via mobile phones, to electronic systems in trains and aircrafts. Semiconductors have infiltrated every corner of our lives. Since the introduction of computers in the mid-20th century, coupled with the birth of the internet dating back to the 1960s, computers and the World Wide Web (WWW) have transformed our lives and have become an essential part of communications. The demand for cheaper, faster and more compact computers has increased dramatically in the past decades. In line with the prediction of Moore’s law, we are now at the bottle-neck for computing performance, largely due to technological limitations in further down-scaling transistors which are already nanometres in size. With the extensive use of semiconductors and the strong driving force of the computing industry, efforts have been put into exploring other technological options – one of which is spin electronics. Researchers are now geared towards introducing magnetism into semiconductors, adding a new page to an already successful story.

Spin electronics, or spintronics, is based on the spin degree of freedom of electrons. Ferromagnetic semiconductors, which are able to exhibit ferromagnetism while retaining their useful semiconducting properties, can be grown by doping a

semiconductor host (such as GaAs) with magnetic impurities (such as Mn). These material systems, called diluted magnetic semiconductors (DMS), exhibit carrier-mediated ferromagnetism which provides a means for electrical control of their magnetic properties. Recent developments of a relatively high Curie temperature ($T_C > 100\text{K}$) DMS based on GaAs [7, 8] has again sparked interest in pursuing applicable devices based on these materials. Spintronics incorporated with DMS might have the advantage of non-volatility with increased data processing speed, decreased electric power consumption, and increased integration densities as compared to mainstream charge-based electronics. The ability to electrically control the properties of these magnetic semiconductors would thus be highly desirable from both a technological and a fundamental physics point of view.

In this report, the magnetic properties of DMS (Ga,Mn)As, based on a common semiconductor GaAs with incorporated Mn ions, under the influence of an applied electric field, were studied. (Ga,Mn)As can be regarded as a prototype material for investigating potential device applications for ferromagnetic semiconductors. The strong spin-orbit mediated coupling of magnetic and semiconductor properties in this material gives rise to many novel transport-related phenomena, such as very large anomalous Hall effect, anisotropic magnetoresistance (AMR), tunneling anisotropic magnetoresistance (TAMR) [9–12] and Coulomb blockade AMR (CBAMR) [13]. The CBAMR is a precedent example for a novel gated spintronics device concept combining nonvolatile memory with transistor functionalities in a single nano-scale element.

Electrical manipulation of a DMS (In,Mn)As was first reported by Ohno and co-workers a decade ago [1]. They demonstrated electric-field control of ferromagnetism in a 5-nm thick (In,Mn)As, using an insulating-gate field-effect transistor (FET) structure. Their results showed changes in anomalous Hall signal (proportional to magnetization), and the Curie temperatures, T_C , of ± 1 K as indicated by Arrott plots, with applied gate voltages. The method has been extended recently to tensile-strained (Ga,Mn)As with perpendicular magnetic anisotropy [3], where they have again realized electrical manipulation of T_C and coercive field, via gating, with a much thinner 50 nm SiO₂ dielectric. They reported a change in the induced hole

density of $2 \times 10^{19} \text{cm}^{-3}$ with the application of $\pm 25 \text{ V}$.

Motivated by the potential to externally control the properties of magnetic materials, investigation of the effects of gating is extended to compressively strained (Ga,Mn)As epilayers, which have more complex in-plane competing cubic and uniaxial magnetic anisotropies. The much richer magnetic properties depend crucially not only on the charge carrier density but also on extremely small strain variations [14, 15], which can be locally induced by nano-lithography and may be modulated by an electrostatic gate. Curie temperature variations as shown previously provide the key physical demonstration of the low-voltage control of magnetization. Nevertheless, for most spintronic functionalities it is not required to destroy the ordered state of spins but only to change their collective orientation. The effects of gating on the in-plane magnetic anisotropies of (Ga,Mn)As are thus of special interest in this project, as it potentially provides a means to manipulate the orientation of the magnetization in this material electrically.

Similar to Ohno's approach, initial study was done by fabricating FET structures containing ultra-thin GaMnAs epilayers. An all-semiconductor, epitaxial p-n junction field-effect transistor of compressive-strained (Ga,Mn)As was fabricated and measured preliminarily as shown in Chapter 4. Detailed investigation of the effects of gating on its in-plane magnetic anisotropies was then carried out (refer to Chapter 5). Lastly, an attempt to increase the effects by gating was made by using a double-gated FET structure with an ionic gel top-gate. The effects of the independent gate actions were looked into in Chapter 6.

Chapter 2

Background

Background knowledge fundamental to the understanding of the experiments described in this thesis is presented in this chapter. Basic magnetic and electrical-transport properties of (Ga,Mn)As as well as fundamental workings of field effect transistor are introduced. Information on p-n junction and ionic gel gating is also included in this chapter.

2.1 (Ga,Mn)As and its properties

Traditionally, the study of dilute magnetic semiconductors (DMS) is concentrated mainly on the II-VI based materials since these materials can be doped by a transition metal to very high concentrations [16]. Conversely, III-V based semiconductors have very low equilibrium solubilities for transition metals. However, in III-V based semiconductors, for example (Ga,Mn)As, the Mn substituting the trivalent cation Ga provides both a hole and a local magnetic moment. Long-range hole-mediated ferromagnetism in these systems has potential for high Curie temperatures. The first III-V based DMS, (In,Mn)As, was produced using low temperature molecular beam epitaxy (LT-MBE) which allows for the growth of epitaxial (In,Mn)As layers without phase separating into the thermodynamically more stable MnAs phase [17]. More recently, epitaxial (Ga,Mn)As was successfully grown on semi-insulating (001) GaAs substrates [18]. It shows well-ordered in-plane ferromagnetism with increasing lattice constant as the concentration of Mn atoms increases. Due to the lattice mis-

match between (Ga,Mn)As and GaAs substrates, compressive strain is induced into the epitaxial layer which brought about the in-plane magnetization in the epitaxial layer [19].

2.1.1 Elemental structure of (Ga,Mn)As

The elements in (Ga,Mn)As have nominal atomic structures $[\text{Ar}]3d^{10}4s^2p^1$ for Ga, $[\text{Ar}]3d^54s^2$ for Mn, and $[\text{Ar}]3d^{10}4s^2p^3$ for As. In zinc-blende (Ga,Mn)As, magnetic transition ion Mn in substitution sites are responsible for both donating holes to mediate long-range ferromagnetic interactions between Mn d-orbitals core spins, and for providing the local magnetic moments. The substituted Mn, Mn_{Ga} , participate in crystal bonding with As via its two 4s-electrons, similar to the substituted Ga. In its electrically neutral state, Mn_{Ga} forms a $[\text{Mn}^{2+}(\text{d}^5) + \text{hole}]$ complex, which is characterized by a local moment with zero orbital angular momentum ($L = 0$) and $S = 5/2$ state, accompanied by a moderately bound hole [20]. This gives (Ga,Mn)As its p-type semiconductor character. The local moment is formed by three occupied sp-d bonding states with dominant t_{2g} ($3d_{xy}$, $3d_{xz}$, $3d_{yz}$) character and by two occupied e_g orbitals that are split from the t_{2g} states by the tetrahedral crystal field and do not strongly hybridize with the sp-orbitals (as shown in Figure 2.1). The weakly bound hole occupies one of the three anti-bonding sp-d levels with dominant As 4p character.

2.1.2 Defects in (Ga,Mn)As

Due to the non-equilibrium growth of (Ga,Mn)As by low-temperature MBE, a substantial number of meta-stable impurity states are formed during the growth of these epilayers. The two defects with the largest effects on the electric and magnetic properties of the DMS systems are interstitial Mn ions, Mn_{I} , and As atoms on cation sites (anti-site defects). Both of them act as donors and are detrimental to the onset of hole-mediated ferromagnetism of these DMS epilayers. The number of such unintended defects increases with higher Mn doping because of the tendency of the material, even under non-equilibrium growth conditions, towards

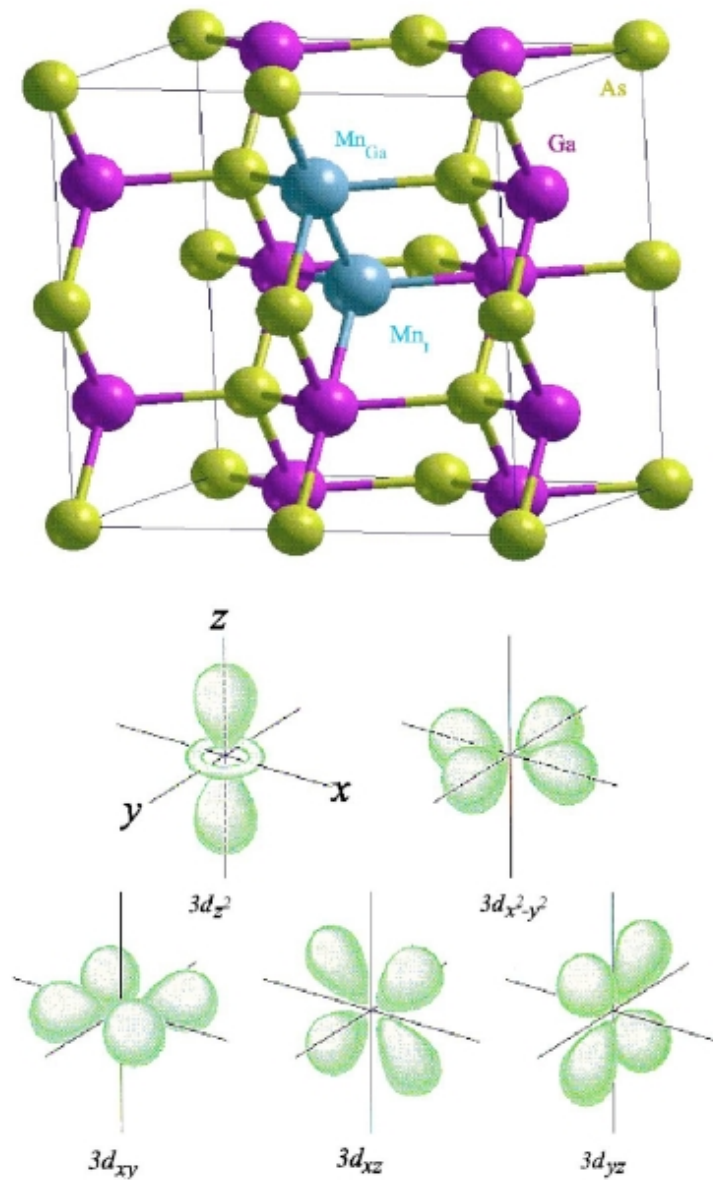


Figure 2.1: Top Diagram: Zinc-blende structure of GaMnAs with substitutional Mn_{Ga} and interstitial Mn_I embedded. Bottom Diagram: Two e_g 3d-orbitals and three t_{2g} 3d-orbitals in Mn. (after Jungwirth *et. al.* [20]).

self-compensation [20].

Interstitial Mn

Direct experimental evidence for Mn dopants occupying tetrahedral interstitial sites rather than the substitutional Ga sites were obtained by combined channeling Rutherford backscattering and particle-induced x-ray emission experiments [21]. This is done by counting relative number of exposed Mn atoms and the ones shadowed by lattice site host atoms at different channeling angles. The density of these defects decreases substantially upon post-growth annealing of the samples close to the growth temperature, suggesting that they are only metastable states [7, 8, 22, 23]. In addition, detailed resistance-monitored annealing studies combined with Auger surface analysis established that Mn_I impurities diffused towards the free DMS epilayer surface during annealing [24].

Interstitial Mn defects play a major role in the ferromagnetism of (Ga,Mn)As. Similar to any divalent impurities on interstitial sites, they become double donors, donating two electrons per interstitial ion and compensating two substitutional Mn acceptors [25]. This results in a decrease in the effective hole densities which is responsible for the mediation of long range ferromagnetic order in (Ga,Mn)As. On top of this, they couple with the local substitutional Mn moments during growth [26] to give rise to short-range anti-ferromagnetic interactions within the pair [27], thereby negating the ferromagnetic interactions in (Ga,Mn)As further. Beside these compensation effects, Mn_I defects also induce a lattice-matching compressive strain in the (Ga,Mn)As epilayers that induces a large uniaxial magnetic anisotropy [28].

As antisites

In addition to Mn occupying interstitial sites, As antisite double-donor defects are formed as a result of non-equilibrium growth at low temperature as well as the overpressure of As used in MBE systems to ensure 2D growth mode. These defects are stable up to 450°C [29] and therefore, cannot be removed by post-growth annealing (since at this high temperature, MnAs phase would dominate in the (Ga,Mn)As epilayers [30]). It was recently shown that the detrimental effects of As antisites on

the magnetic properties of (Ga,Mn)As can be reduced by using As₂ dimers instead of As₄ tetramers and by maintaining a strictly stoichiometric growth mode [31].

2.1.3 Post-growth annealing

Over the past years, many experiments centred on the annealing of (Ga,Mn)As layers were performed to provide a better understanding of the nature of these compensating defects. A good understanding is critical since the removal of these defects could mean a higher achievable Curie temperature (T_C). Early experiments showed that for long annealing times and high temperatures (close to or above MBE growth temperature), a reduction of T_C was observed [32–34]. A possible explanation for the reduction of T_C under such conditions may be due to the removal of Mn from the electrically active Ga sites, for which the activation energy is much higher than that of the interstitial sites [7]. A much lower annealing temperature of 175°C [7] compared with 250°C or 282°C employed previously, can therefore lead to an almost complete inhibition of this unwanted mechanism while still allowing for the precipitation of Mn interstitials, leading to a higher T_C than earlier reported. The highest T_C obtained with annealed (Ga,Mn)As to date is ~ 180 K [4]. It is however noted that the growth and post-growth annealing process has yet to be optimized. In order to utilize this material for spintronics devices, the Curie temperature must well exceed room temperature. A combination of optimized fabrication processes and high concentration of Mn dopants will be needed to lead to room temperature ferromagnetism.

2.2 Carrier-mediated ferromagnetism

The origin of ferromagnetism is almost always the interplay between the electronic spin degree of freedom, repulsive Coulomb interactions between electrons, and Pauli's exclusion of electronic states. The Coulomb electrostatic interactions arise because charges of the same sign require more energy to stay close together than when they are apart. The Pauli exclusion principle correlates the spin and orbital parts of the many-electron wave function by requiring the total wave function to be anti-

symmetric under particle exchange. The coupling between these two interactions is fundamental in any exchange interaction.

Magnetism in (Ga,Mn)As originates from the Mn local moments, which are affected by the doping level as well as any as-grown crystal defects. The relative orientation of the Mn moments to attain a configuration of lowest energy is achieved through exchange interactions which originated mainly from electrostatic interactions and fermionic statistics of electrons. Several causes that lead to exchange interactions can be separately identified qualitatively when addressing magnetic order in (Ga,Mn)As. These exchange interactions are discussed in the following section.

2.2.1 Exchange interactions

The exchange interactions fundamental to the ferromagnetism in (Ga,Mn)As are discussed in this section. In particular, Zener's indirect exchange interaction, which is the basis for the long-range carrier mediated ferromagnetism in (Ga,Mn)As, is explained.

Direct exchange

Direct exchange involves electrons on neighbouring magnetic atoms interacting directly with one another without any intermediary. The origin of this is the difference between the Coulomb energy of a symmetric orbital wave function (antisymmetric spin singlet state) and an antisymmetric orbital wave function (symmetric spin triplet state). This is often not an important mechanism in controlling the magnetic properties in (Ga,Mn)As because there is insufficient direct overlap between neighbouring magnetic orbitals.

Kramer's superexchange

Kramer's superexchange is an indirect exchange interaction between non-neighbouring magnetic ions, mediated by a non-magnetic ion that is placed in between the magnetic ions. Superexchange is a second-order process that is derived from second-order perturbation theory. It gives an antiferromagnetic contribution in (Ga,Mn)As

and comes about because there is a kinetic energy advantage as antiferromagnetic coupling lowers the energy of the system by allowing these electrons to become delocalized over the whole structure. However, according to the two-fluid model of electronic states near the metal-insulator transition [35], to gain Coulomb energy, the bound magnetic polarons (formed by carriers which are trapped on strongly localized impurity states) are formed around close pairs of ionized acceptors which lead to a ferromagnetic coupling between them. This leads, via Zener's double exchange, to a ferromagnetic order and minimizes the short-range antiferromagnetic contribution in (Ga,Mn)As.

Zener's double exchange

Zener's double exchange mechanism is an interaction between the magnetic ions with mixed valency (capable of two or more different valence states) via electrons hopping through the intermediate non-magnetic ion within the magnetic shells. Together with Hund's rule, it favours ferromagnetism since parallel spin alignment increases the hopping probability and therefore decreases the kinetic energy of spin-polarized electrons. A version of this is in which the Mn acceptor states form an impurity band with mixed *spd* character [20]. In this case, electrical conduction and Mn-Mn exchange coupling are both realized through hopping within an impurity band. The potential importance of double exchange is greater for (Ga,Mn)As with low Mn doping.

Zener's indirect exchange

Indirect exchange interaction between local moments can occur through the mediation of the itinerant carriers in the s- or p- band. In (Ga,Mn)As, the valence band hole states and the local Mn spins couple antiferromagnetically through p-d exchange. Since Mn_{Ga} and As belong to different sublattices, direct exchange between holes near the top of the band and localized Mn d electrons is weak. This allows p-d hybridization to dominate. The antiferromagnetic sign of the p-d exchange interaction [36] seen in experiment [37] can be explained by the simple picture in Figure 2.2.

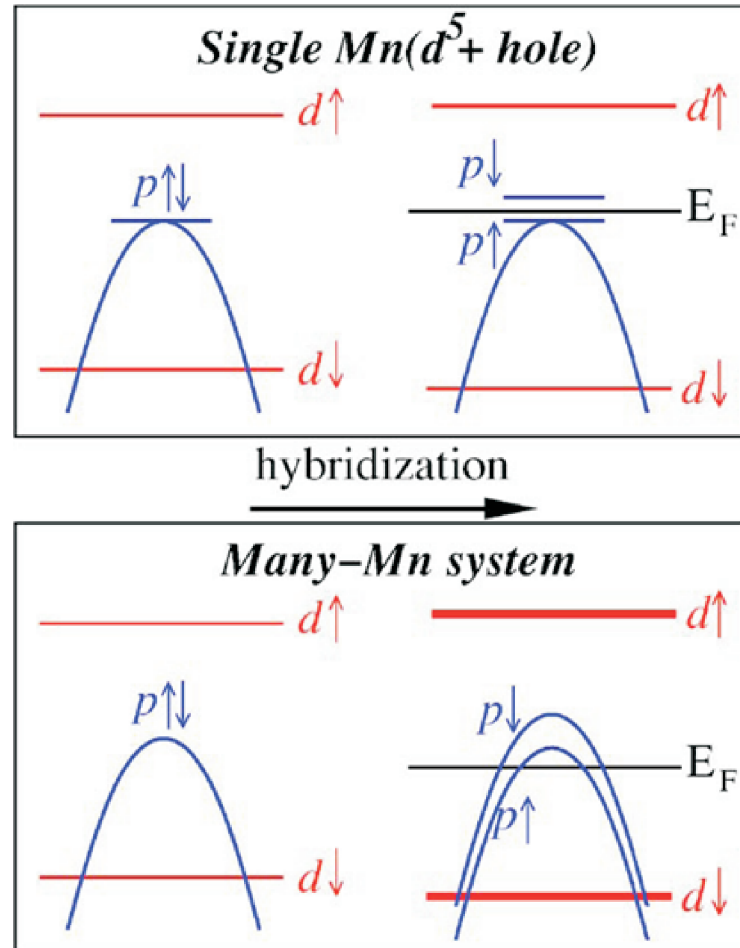


Figure 2.2: A simple picture illustrating the antiferromagnetic coupling between valence band states and local Mn moments due to p-d hybridization for an isolated Mn acceptor state (top) and for the many Mn-atom system (bottom). (after Jungwirth *et. al.* [20])

Figure 2.2 gives a simple physical picture of the p-d exchange interaction, assuming mean-field approximation. Consider first a single Mn neutral complex ($d^5 + \text{hole}$). The energy of the spin-up and spin-down valence band states in the p-shell is split as a result of the p-d hybridization (level repulsion of like-spin states) with the Mn d-shell level (for example, say the filled, spin-down, Mn d-shell level is deep in the valence band while the empty spin-up d level is high in the conduction band above the Fermi level). This results in an antiferromagnetic coupling between the localized Mn spins and the hole spins. The aligned itinerant valence-band holes will then line up the overlapped Mn moments.

When the coupling is weak (the band carrier polarization is weak e.g. at temperatures near T_C), the effect is described by RKKY (Ruderman, Kittel, Kasuya, and Yosida) theory (calculation based on delta functions which simulate the localized nuclear moments and act as perturbation in an electron gas). The range of this interaction (RKKY) can be long, and interactions between separate local moments can vary between ferromagnetic or antiferromagnetic in space depending on the length scale of the itinerant band's Fermi wavelength. Zener's indirect exchange plays an important role and is likely to dominate in the case of strongly metallic (Ga,Mn)As, where a high density of itinerant holes is present. There is no sharp distinction between impurity band double-exchange and kinetic-exchange interactions; the former is simply a strong-coupling, narrow band limit of the latter.

2.2.2 Qualitative picture of ferromagnetism

Several types of qualitative effects which lead to exchange interactions in (Ga,Mn)As can be identified and the relative importance of each effect is dependent on the doping level of the Mn in the host GaAs material. A clear picture of this is painted in Reference [20].

At very low concentration of the doping Mn ions, the average distance between Mn impurities is much larger than the size of the bound hole characterized approximately by the impurity effective Bohr radius. For this very diluted insulating limit, ferromagnetic exchange interaction between Mn moments is mediated by thermally activated band carriers [38].

At higher concentrations of substituting Mn ions, above approximately 1% of Mn as shown experimentally [34, 39, 40], the system is near the Mott-insulator-to-metal transition. The localization length of the impurity band states of these systems is extended to a degree that allows them to mediate ferromagnetic exchange interactions between Mn moments. In this case, Zener's double-exchange mechanism prevails. The Mn acceptor states form an impurity band with a mixed spd character, and electrical conduction and Mn-Mn exchange coupling occur through hopping within this impurity band.

At even higher concentration of Mn ions, the impurity band gradually merges with the valence band [41] and the impurity states delocalize. In these metallic (Ga,Mn)As ferromagnets, the coupling between Mn local moments is mediated by the p-d kinetic exchange interactions between the d-shell Mn moments and the p-band itinerant holes [42–45], as illustrated in Figure 2.2.

The transition between the impurity band regime and the valence band regime is a gradual one. It is controlled not only by the Mn density, but also by the carrier density. The latter will be an important aspect for magnetization switching by electrical means.

2.3 Magnetic anisotropy

The preference for the magnetization to lie in a particular direction, with respect to crystallographic axes in a sample, is called magnetic anisotropy. Magnetic anisotropy can have its origin in sample shape, crystalline symmetry, stress, directed atomic pair ordering etc.

The magnetic dipolar anisotropy, or shape anisotropy, is mediated by dipolar interactions. It is long-range, and its contribution depends on the shape of the sample. For example, in a long and thin sample, in-plane alignment of magnetic moments usually prevails since the perpendicular magnetic anisotropy (PMA) will result in a higher energy state with a larger demagnetization field. However, the observation of PMA in some (Ga,Mn)As layers points to the existence of an anisotropy which is stronger than the shape anisotropy. This puts the focus on the epitaxial strain

caused by the lattice mismatch from the substrate or defects in the LT-MBE growth.

(Ga,Mn)As grown epitaxially in LT-MBE allows strain engineering through lattice matching of (Ga,Mn)As with the substrate. During LT-MBE growth, (Ga,Mn)As films have their lattices locked to those of their substrates in the plane perpendicular to the growth axis. For a (Ga,Mn)As film grown on a (Ga,As) substrate, compressive strain prevails since the lattice constant of relaxed (Ga,Mn)As is larger than the lattice constant of GaAs, especially so if interstitial Mn_I or As_{Ga} antisites are present in the DMS crystal. The effects of strain on the magnetic anisotropy in (Ga,Mn)As is discussed in Section 2.3.1.

Another factor affecting the magnetic anisotropy in (Ga,Mn)As is its hole density, which will be discussed in more details in section 2.3.2. Also, the experiments included in the thesis are based mainly on Corbino devices. An understanding of magnetocrystalline anisotropy for this geometry is essential and is included in the following section 2.3.3.

2.3.1 Effects of strain on magnetic anisotropy

To understand the effects of strain on magnetic anisotropy, it is helpful to consider a simple picture of a model for a nearly empty top of the valence band (low hole concentration) in compressively strained compounds with a zinc-blende crystalline structure, such as (Ga,Mn)As and p-type (Cd,Mn)Te [46]. This is illustrated in Figure 2.3. Due to strong spin-orbit interaction, $s_{||}$ for holes with $j = 3/2$ (heavy holes) resides above the $j = 1/2$ level (light holes). For the case with biaxial compressive strain, the ground state subband assumes a heavy-hole character with $j_z = 3/2$. Provided that only the ground state subband is occupied, the hole spins are oriented along the growth direction, z . Now, since the p-d exchange interaction has a scalar form, $H_{pd} \sim s \cdot S$, where s is the hole spin and S is the spin of the Mn ions, the energy of the holes can be maximally lowered through p-d exchange interaction with the Mn spin magnetization M if s and S are aligned parallel to each other. Hence, perpendicular magnetic anisotropy is favoured if the ground state assumes a heavy-hole character.

However, the energetic distance between the heavy hole $j_z = 3/2$ and light hole

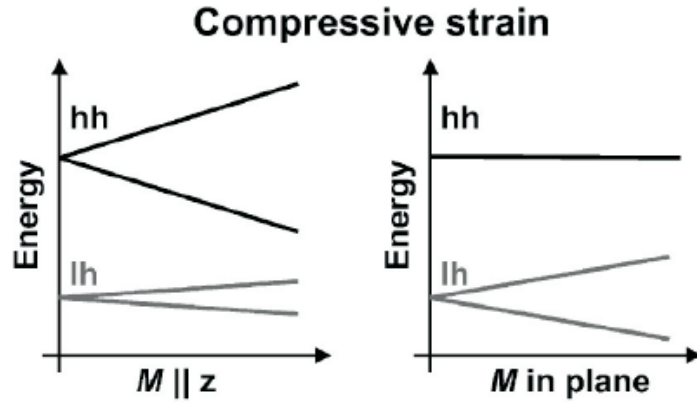


Figure 2.3: Valence band splitting in compressively strained tetrahedrally coordinated semiconductors for two orientations of magnetization M - perpendicular to plane (left) and in-plane (right). z is the growth direction perpendicular to the sample plane. (after Sawicki *et. al.* [46])

$j_z = 1/2$ subbands depends on strain. In particular, the ground state subband can acquire a light-hole character for a sufficiently large magnitude of biaxial tensile strain. In the latter case, the in-plane component of the hole spin is greater than the perpendicular component, so that a stronger exchange splitting will occur for the in-plane orientation of M . Hence, in-plane anisotropy is expected if only the light-hole subband remains occupied.

However, this is not readily observed in the case of (Ga,Mn)As, since by nature, (Ga,Mn)As systems are heavily populated with holes. Consider the same picture in Figure 2.3. With increasing hole concentration in the system, the light hole subband is populated. Moreover, the heavy holes begin to acquire a light hole character as the Fermi energy increases with increasing hole concentration. Since the light-hole subband is associated with in-plane anisotropy, the effect of isothermal increase in hole concentration can result in a reorientation of the magnetic anisotropy from out-of-plane to in-plane even for compressively strained systems. This is shown in Figure 2.4 theoretically using the p-d Zener model (refer to Section 2.3.2).

Figure 2.4 shows the hole concentration dependence of the computed anisotropy field for different spin-splitting parameter B_G (which corresponds to saturation

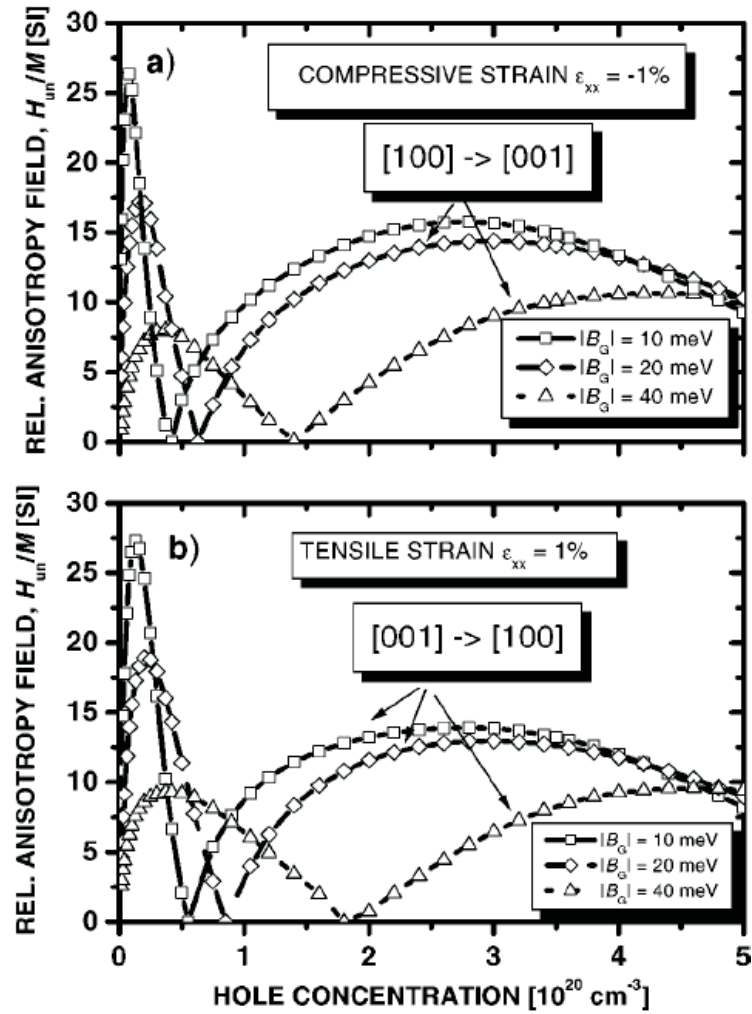


Figure 2.4: Computed minimum field H_u (divided by M) necessary to align magnetization M along the hard axis for (a) compressive and (b) tensile biaxial strain in $(\text{Ga},\text{Mn})\text{As}$ films for various values of the spin-splitting parameter B_G . For compressive strain, the easy axis is along the $[001]$ direction and in the (001) plane at low and high hole concentrations, respectively. The opposite behaviour is observed for tensile strain. The symbol $[100] \rightarrow [001]$ means that the easy axis is along $[100]$, so that H is applied along $[001]$. The value of $B_G = 30$ meV corresponds to the saturation value of M for $\text{Ga}_{0.95}\text{Mn}_{0.05}\text{As}$. (after Dietl *et al.* [35])

value for Mn magnetization, M and is related to the p-d exchange interaction) of (Ga,Mn)As films under compressive and tensile strains [35]. The results shown are in agreement with the simple picture, where the perpendicular and in-plane magnetization is expected for compressively and tensile strained systems with low hole concentration respectively. Beyond a critical hole concentration, depending on the exchange splitting energy, a reorientation of the easy axis direction is expected.

It is also observed experimentally that the easy-axis is in-plane for compressive strain and out-of-plane for tensile strain [18, 19]. Figure 2.5 plots the magnetization M for Ga_{0.97}Mn_{0.03}As thin films as a function of magnetic field H . Sample No. 1 was grown directly on a [001] GaAs substrate under compressive strain, inducing an easy-axis along [110] in-plane, while sample No. 2 was grown on an Ga_{0.85}In_{0.15}As buffer and is under tensile strain, resulting in an easy-axis along [001] which is perpendicular to the sample plane.

2.3.2 Effects of hole density on magnetic anisotropy and Curie temperature

To understand the effects of hole density on the magnetic anisotropy and Curie temperature, T_C , of (Ga,Mn)As in greater detail, the p-d Zener model is discussed briefly here.

According to the model [20, 35, 43], ferromagnetism is driven by exchange coupling of the carriers and the localized spins (refer to Section 2.2.1). However, the Zener model does not take into account the itinerant character of the magnetic electrons and the quantum (Friedel) oscillations of the electron spin polarization around the localized spins which are essential for magnetic metals. In particular, the resulting competition between ferromagnetic and antiferromagnetic interactions in metals leads to a spin-glass rather than to a ferromagnetic ground state. In the case of semiconductors with lower concentration of carriers, the mean distance between the carriers is usually much greater than that between the spins. Under such conditions, the exchange interaction mediated by the carriers is ferromagnetic for most of the spin pairs, which reduces the tendency toward spin-glass freezing. In fact, for a

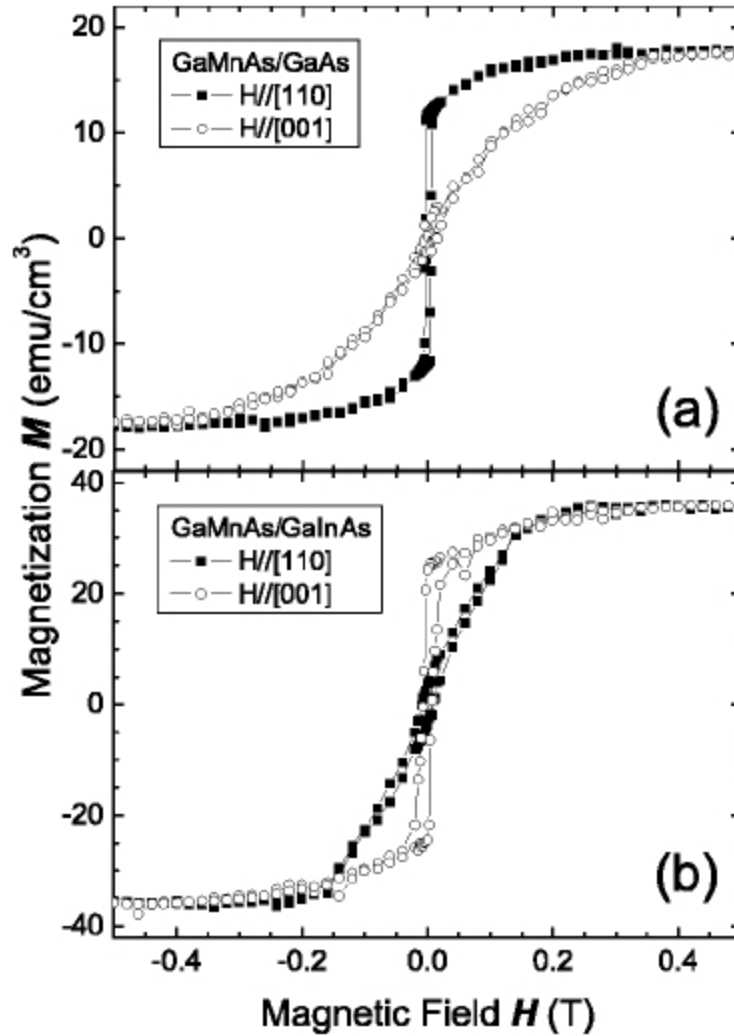


Figure 2.5: Magnetization M as a function of magnetic field H for $\text{Ga}_{0.97}\text{Mn}_{0.03}\text{As}$ thin films, measured at 55 K by SQUID for sample No. 1 at the top panel and sample No. 2 at the bottom panel. The magnetic field is applied either in the [110] or in the [001] direction. (Ga,Mn)As sample No. 1, grown directly on a [001] GaAs substrate, is under compressive strain in the layer plane while sample No. 2, grown on an $\text{Ga}_{0.85}\text{In}_{0.15}\text{As}$ buffer, is under tensile strain. Note that the easy axis is different for the two samples. (after Liu *et. al.* [19])

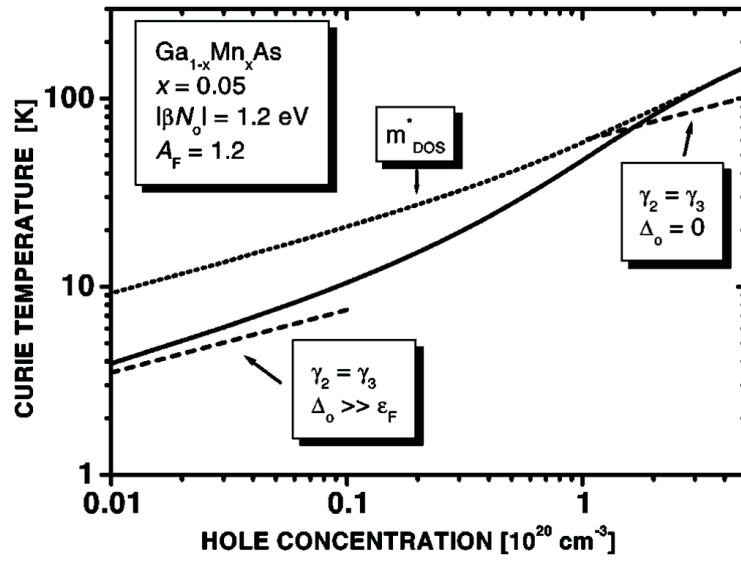


Figure 2.6: Curie temperature as a function of the hole concentration for $\text{Ga}_{0.95}\text{Mn}_{0.05}\text{As}$ computed from the 6×6 Luttinger model (solid line). Straight dashed lines represent results obtained assuming a large and a small value of the spin-orbit splitting Δ_0 , respectively. The dotted line is calculated neglecting the effect of the spin-orbit interaction on the hole spin susceptibility (after Dietl *et al.* [35]).

random distribution of the localized spins, the mean-field value of T_C deduced from the Zener model is equal to that obtained from the RKKY approach in which the presence of the Friedel oscillations is explicitly taken into account. This validates the use of the Zener model in (Ga,Mn)As which takes into account the effects of spin-orbit coupling in the host material, a task technically difficult for the RKKY approach.

In the Zener model, Mn moments adjust their orientation to minimize the total energy of the carriers required to support ferromagnetic ordering of the Mn ions. In particular, depending on the Fermi level position within the valence band or the value of the exchange splitting (that is depending on magnetization and thus also on temperature) different orientations of magnetization can be required to drive the system to its energy minimum. Therefore, by changing hole concentration or temperature, the corresponding changes of the overall orbital momentum of the hole liquid may force a spontaneous reorientation of magnetization.

A detailed calculation using the Zener model, taking into consideration the band structure effects, is done by Dietl *et. al.* in [43]. The model starts with a mean-field approach to determine how the Ginzburg-Landau free-energy functional F depends on the magnetization M of the local spins. There are two contributions to F ; (a) the hole contribution $F_c[M]$ (computed by diagonalizing the 6×6 Kohn-Luttinger matrix together with the p-d exchange contribution, and by subsequent computation of the partition function Z) and (b) the contribution of the localized spin $F_s[M]$. The free-energy functional is then given by $F = F_c[M] + F_s[M]$. By minimizing F with respect to M at given temperature T and hole concentration p , T_C can be computed within the mean-field approximation. Here T_C contains both the ferromagnetic (T_F) and antiferromagnetic contribution (T_{AF}) [35].

$$T_C = x_{eff} N_0 S(S+1) \beta^2 A_F \rho_s(T_C) / 12 K_B - T_{AF} \quad (2.1)$$

where A_F is the Fermi-liquid parameter, x_{eff} is the effective Mn concentration, β is the p-d exchange integral, N_0 is the concentration of cation sites and ρ_s is the spin density of states.

Figure 2.6 plotted the values of T_C as a function of the hole concentration p for $\text{Ga}_{0.95}\text{Mn}_{0.05}\text{As}$ using the above model. The Luttinger parameter γ_2 is taken to be equal to γ_3 (neglecting band warping) for the small and large values of the spin-orbit splitting Δ_0 . The values of $x_{eff} \sim x$ and $T_{AF} \sim 0$ as approximated using the two-fluid model.

For a strongly degenerate carrier liquid, $|\mathcal{E}_f|/k_B T \gg 1$, and neglecting the spin-orbit interaction, ρ_s becomes equal to the total density of states ρ for intraband charge excitations, where $\rho = m_{DOS}^* k_F / \pi^2 \hbar^2$. This gives a generalized relationship between T_C and the hole concentration p as [20, 47]

$$T_C = C x p^{1/3} \quad (2.2)$$

where C is a constant specific to the host material, x is the mole fraction of substituted Mn^{2+} .

Using the above model and considering an unstrained thin film with the [001] crystal direction perpendicular to its plane, the hole energies $E_c[M]$ can be computed

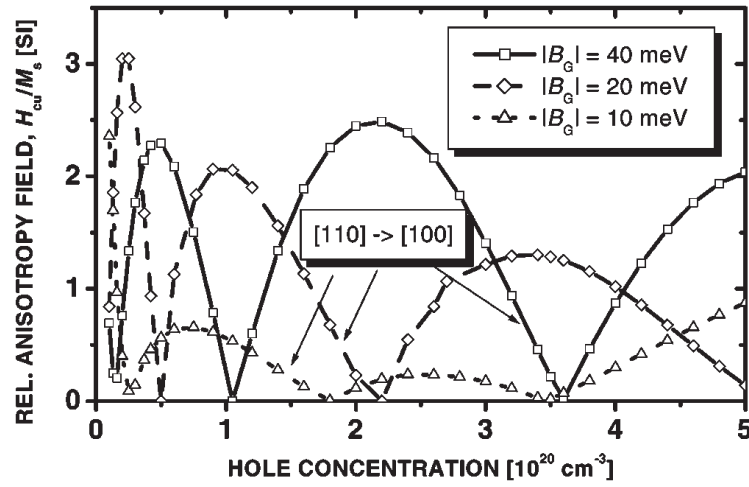


Figure 2.7: Computed minimum magnetic field H_{cu} (divided by M) necessary to align magnetization M along the hard axis for cubic (unstrained) $\text{Ga}_{1-x}\text{Mn}_x\text{As}$ film. As a function of the hole concentration and the spin-splitting parameter B_G , the easy and hard axes fluctuate alternately between $[110]$ and $[100]$ (or equivalent) directions in the plane of the film. The symbol $[110] \rightarrow [100]$ means that the easy axis is along $[110]$, so that H_{cu} is applied along $[100]$ ($B_G = 30$ meV corresponds to the saturation value of M for $\text{Ga}_{0.95}\text{Mn}_{0.05}\text{As}$) (after Dietl *et. al.* [35]).

for relevant parameters for the orientation of M along the [100], [110] and [111] directions, taking into account the stray field energy E_d and considering the lowest order of the cubic anisotropy [35].

$$E_c(M, \theta, \phi) - E_c(M, \pi/2, 0) = K_d(M) \cos^2 \theta + K_{c1}(M) (\sin^4 \theta \sin^2 \phi \cos^2 \phi + \sin^2 \theta \cos^2 \theta) \quad (2.3)$$

where the angle θ is between M and the normal to the film surface and ϕ the angle between M and the crystalline axes. For the usual parameters of (Ga,Mn)As, M lies in the (001) plane, and the easy axis is directed along the [100] for $K_{c1} > 0$ or along the [110] (or equivalent) crystal axis in the opposite case [35]. It turns out that the sign of K_{c1} depends on the degree of occupation of the hole subbands as well as on their mixing by the p-d and k.p interactions. As a result, the easy axis fluctuates between [100] and [110] as a function of p.

To quantify the strength of the cubic anisotropy in (Ga,Mn)As, $K_{c1}(M)$ is computed, and then the minimum magnitude of an external magnetic field $H_{cu} = 2|K_{c1}/M|$ (or $\mu_0 H_{cu} = 2|K_{c1}/M|$ in SI units), that aligns the spontaneous magnetization M along the hard direction is calculated.

Figure 2.7 shows the computed minimum magnetic field H_{cu}/M necessary to align magnetization M along the hard axis for cubic (unstrained) $\text{Ga}_{1-x}\text{Mn}_x\text{As}$ film. It reveals that the easy axis is expected to switch between [100] and [110] (or equivalent) in-plane cubic directions as a function of holes density. In addition to the cubic in-plane anisotropy, experimental data [19, 46, 48] points to a non-equivalence of [110] and $[\bar{1}10]$ directions, which unveils the existence of an in-plane uniaxial magnetic anisotropy in (Ga,Mn)As.

2.3.3 Magnetocrystalline anisotropy

Magnetocrystalline anisotropy is a spin-orbit effect often associated with localized electrons in magnetic d or f-shells. Local Mn moments in (Ga,Mn)As, however, are treated in the Kohn-Luttinger (KL) kinetic exchange model as pure spins $S = 5/2$ with angular momentum $L = 0$ and therefore do not contribute to the anisotropy. The physical origin of the anisotropy energy in this model is spin-orbit coupling in

the valence band [49]. A large number of experimental observations in the (III,Mn)V DMSs, including easy axis orientations dependent on hole densities, temperature, or strains in the lattice [19,46,48,50] are explained within the mean-field approximation to the KL kinetic-energy model.

A quantitative measure of the strength of the magnetocrystalline (or any other) anisotropy is the field, H_a , needed to saturate the magnetization in the hard direction. This field is called the anisotropy field. The energy needed to saturate a material in a particular direction is given by the equation [51]:

$$u_a = \mu_0 \int_0^{M_s} H(M) dM \quad (2.4)$$

where M_s is the saturation magnetization.

The magnetocrystalline anisotropy in (Ga,Mn)As can be broken down into uniaxial anisotropy and cubic anisotropy. The cubic anisotropy scales with the magnetization M as M^4 , whereas the uniaxial term scale with M^2 . It is therefore expected that the cubic magnetocrystalline anisotropy dominates at low temperatures and there is a cross-over where the uniaxial anisotropy take over as temperature increases towards T_C [52].

Uniaxial anisotropy

A material is described as having uniaxial anisotropy when it has a preference for magnetization along a single axis. The free energy of a uniaxial magnetic material must depend on the magnetization vector such that it minimizes the energy when it lies along the easy axis. This energy can be approximated as an energy function. The uniaxial crystal anisotropy energy density can be expressed as a power series of the form [51]:

$$u_a = U_0/V_0 = \sum_n K_{un} \sin^{2n} \theta \quad (2.5)$$

For most purposes, it is sufficient to keep only the first three terms:

$$u_a = K_{u0} + K_{u1} \sin^2 \theta + K_{u2} \sin^4 \theta + \dots \quad (2.6)$$

where K_{u0} does not carry any anisotropic property since it is independent of the orientation of the magnetization. $K_{u1} > 0$ implies an easy axis [51].

Cubic anisotropy

As compared to the uniaxial anisotropy, the energy surfaces for cubic crystals are not as straight forward. An instructive way to write out the anisotropy of a cubic system will be to expand the free energy in powers of the direction cosines, α_1 , α_2 , α_3 , of the magnetization along the three coordinate axes and apply symmetry operations to reduce the number of independent terms. (Here, $\alpha_i = m_i = M_i/M_s$). Of all the possible terms in the expansion, only those that leave the energy invariant under the symmetry operations of the crystal can be kept.

The anisotropy of a cubic system [51] is then written as

$$u_a = K_{c0} + K_{c1}(\alpha_1^2\alpha_2^2 + \alpha_2^2\alpha_3^2 + \alpha_3^2\alpha_1^2) + K_{c2}(\alpha_1^2\alpha_2^2\alpha_3^2) + \dots \quad (2.7)$$

Using the trigonometric functions of spherical coordinates (θ, ϕ) , the coefficient of K_{c1} in equation 2.7 reduces to

$$\sin^4 \theta \cos^2 \phi \sin^2 \phi + \cos^2 \theta \sin^2 \theta = 1/4(\sin^4 \theta \sin^2 2\phi + \sin^2 2\theta) \quad (2.8)$$

2.3.4 The Stoner-Wohlfarth Model

For a single-domain particle, one can calculate the magnetization curve using the Stoner-Wohlfarth model. Since the particle is assumed to be single-domain, there are no domain walls and only coherent domain rotation needs to be considered.

Taking only the first order term for both the uniaxial and cubic anisotropy, the energy of the system can be written as

$$E(\theta, \phi) = K_u \sin^2 \phi - K_c \sin^2 2\phi/4 - MH \cos(\theta - \phi) \quad (2.9)$$

where H and M are the magnitudes of the external field and magnetization, respectively, and ϕ is the direction of the magnetization to the external magnetic field, and θ is the angle of the magnetic field to the easy axis of the sample. K_u is the uniaxial anisotropy constant and K_c is the cubic anisotropy constant.

The energy can be minimized to find the direction of the magnetization at any given value of the applied magnetic field. Analytical solutions can be found using this model for values of θ at 0 and $\pi/2$. This model is assumed and used in Chapters 5 and 6 to calculate the values of the anisotropy constants K_u and K_c .

Starting with the Equation 2.9, the first derivative of the energy, $E(\theta, \phi)$ with respect to ϕ is given by:

$$\frac{\delta E(\theta, \phi)}{\delta \phi} = K_u \sin 2\phi - \frac{1}{2}K_c \sin 4\phi - MH \sin(\theta - \phi) \quad (2.10)$$

The second derivative can also be expressed as:

$$\frac{\delta^2 E(\theta, \phi)}{\delta^2 \phi} = 2K_u \cos 2\phi - 2K_c \cos 4\phi + MH \cos(\theta - \phi) \quad (2.11)$$

Considering the switching fields for the easy axes at $\theta = 0^\circ$ and $\theta = 90^\circ$, and minimizing the energy density to find the lowest energy state, we obtain:

For $\theta = 0^\circ$, $\frac{\delta E(\theta, \phi)}{\delta \phi}$ becomes

$$\frac{\delta E(\theta, \phi)}{\delta \phi} = K_u \sin 2\phi - \frac{1}{2}K_c \sin 4\phi + MH \sin \phi = 0 \quad (2.12)$$

giving

$$2K_u \cos \phi - 2K_c \cos \phi \cos 2\phi = -MH_{C(\theta=0^\circ)} \quad (2.13)$$

Similarly for $\theta = 90^\circ$,

$$\frac{\delta E(\theta, \phi)}{\delta \phi} = K_u \sin 2\phi - \frac{1}{2}K_c \sin 4\phi - MH \cos \phi = 0 \quad (2.14)$$

$$2K_u \sin \phi - 2K_c \sin \phi \cos 2\phi = MH_{C(\theta=90^\circ)} \quad (2.15)$$

Assuming that the magnetization is aligned by the external magnetic field just before switching at the switching field, H_C , then at that point $\theta = \phi$. This gives:

For $\theta = 0^\circ$,

$$2K_u - 2K_c = -MH_{C(\theta=0^\circ)} \quad (2.16)$$

For $\theta = 90^\circ$,

$$2K_u + 2K_c = MH_{C(\theta=90^\circ)} \quad (2.17)$$

Solving the simultaneous Equations 2.16 and 2.17, the anisotropy constants K_c and K_u can be expressed as:

$$K_c = \frac{1}{4}M(H_{C(\theta=90^\circ)} + H_{C(\theta=0^\circ)}) \quad (2.18)$$

$$K_u = \frac{1}{4}M(H_{C(\theta=90^\circ)} - H_{C(\theta=0^\circ)}) \quad (2.19)$$

The values of K_c and K_u can thus be found for the different gate voltages using the above equations.

2.4 Magneto-transport

Magneto-transport can be broken down into ordinary effects which depend on the applied magnetic field, H , and extraordinary effects which depend also on the orientation of the magnetization M present only in magnetically polarized materials.

The ordinary Hall effect is a familiar phenomenon in which a transverse electric field E_H appears across a sample when an applied magnetic field H has a component perpendicular to the current density J as a result of the Lorentz force acting on the charge carrier. It is often described by the Hall resistivity, $\rho_H = E_H/J_x = R_0H$, where R_0 is the ordinary Hall coefficient. The anomalous Hall effect in ferromagnetic materials can then be extended to include the effect in response to the magnetization, and the Hall resistivity can be rewritten as $\rho_H = (R_0H + R_sM)$ where the second term is the spontaneous effect proportional to the magnetization M and R_s is the anomalous Hall coefficient.

More important to the discussion in this thesis is the change in the resistance of a conductive material in the presence of an applied magnetic field. The result of this effect is called magnetoresistance (MR). Magnetoresistance can be further categorized into isotropic MR (IMR), anisotropic MR (AMR), tunneling MR (TMR), tunneling AMR (TAMR) and Coulomb blockade AMR (CBAMR). As IMR and AMR are both measured and used as a probe for the magnetic anisotropy in (Ga,Mn)As in later chapters, they will be discussed in detail in the following sections.

2.4.1 Isotropic Magnetoresistance

For (Ga,Mn)As, its resistivity decreases with increasing magnetic field strength, $|H|$. This effect can be referred to as negative isotropic magnetoresistance (IMR). The IMR is approximately linear with $|H|$ at low fields and it does not saturate even at high magnetic fields of up to 10 - 20 T [53, 54].

Figure 2.8 shows a typical magnetoresistance plot with an applied magnetic field perpendicular to the sample plane. The easy axis of the sample is not aligned with the field direction. At temperatures below T_C with a small applied field, a positive magnetoresistance is seen. The peaking of the magnetoresistance corresponds to a

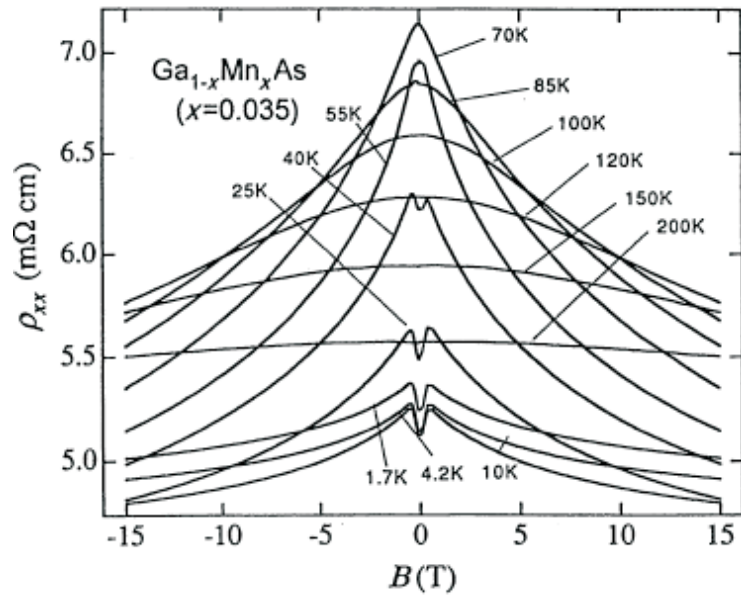


Figure 2.8: Longitudinal resistivity ρ_{xx} in $\text{Ga}_{0.965}\text{Mn}_{0.035}\text{As}$ at different temperatures. The applied magnetic field is along the direction perpendicular to the sample plane. (after Iye *et. al.* [55])

rotation of the magnetization direction in the sample as a result of a competition between the anisotropy field in the ferromagnetic sample and the applied magnetic field. This positive magnetoresistance is present only in the ferromagnetic phase and is found to be sensitive to the magnetic field orientation with respect to the transport current, as well as to the crystalline directions (refer to Chapter 5). This is a result of the AMR effect observed in ferromagnetic materials. As H increases, the magnetization in the sample aligns with the direction of the applied field and a negative magnetoresistance is observed. This negative magnetoresistance is a result of the IMR in the sample since AMR is already saturated at high field.

The presence of the large negative IMR can be explained by two basic mechanisms [45, 55, 56]. At high temperatures near T_C of the sample, the negative IMR can be attributed to a decrease in scattering due to a field-induced reduction in the spin disorder which is responsible for much of the resistance near T_C . For lower temperatures, the spins are already mostly aligned. The negative magnetoresistance which appears in this case is a result of the destructive influence of the magnetic

field on interference of scattered waves [56].

2.4.2 Anisotropic Magnetoresistance

As discussed briefly in the previous section, anisotropic magnetoresistance (AMR) is the relative change in the resistance of a ferromagnetic material in response to a change in the orientation of its magnetization. It can be defined as the difference between the magnetoresistance (MR) for fields applied perpendicular to the current and that for a field applied along the current [57]. Phenomenologically, AMR has a non-crystalline component, arising from the lower symmetry for a specific current direction, and crystalline components arising from the crystal symmetries. In (Ga,Mn)As, it has been observed that the AMR consists of a non-crystalline component of the opposite sign (compared to most ferromagnetic metals) and typically much weaker crystalline terms reflecting the underlying magnetocrystalline anisotropies [58, 59].

Phenomenology of AMR

The phenomenology of AMR for (Ga,Mn)As can be written by extending the standard phenomenology [60] to systems with cubic [100] and uniaxial [110] anisotropy. The longitudinal AMR can then be written as [58, 59],

$$\frac{\Delta\rho_{xx}}{\rho_{av}} = C_I \cos 2\phi + C_U \cos 2\psi + C_C \cos 4\psi + C_{I,C} \cos(4\psi - 2\phi) \quad (2.20)$$

and the transverse AMR can be written as,

$$\frac{\Delta\rho_{xy}}{\rho_{av}} = C_I \sin 2\phi - C_{I,C} \cos(4\psi - 2\phi) \quad (2.21)$$

where $\Delta\rho_{xx} = \rho_{xx} - \rho_{av}$, ρ_{av} is the longitudinal resistance averaged over 360° in the plane of the film, ϕ is the angle between the magnetization unit vector \hat{M} and the current, and ψ is the angle between \hat{M} and the [110] crystal direction. The four contributions to the longitudinal AMR are the non-crystalline term, the lowest order uniaxial and cubic crystalline terms, and a crossed non-crystalline/crystalline term (in the same order as in Equation 2.20). The higher order terms in the expressions are neglected here. For the transverse AMR, the purely crystalline terms are

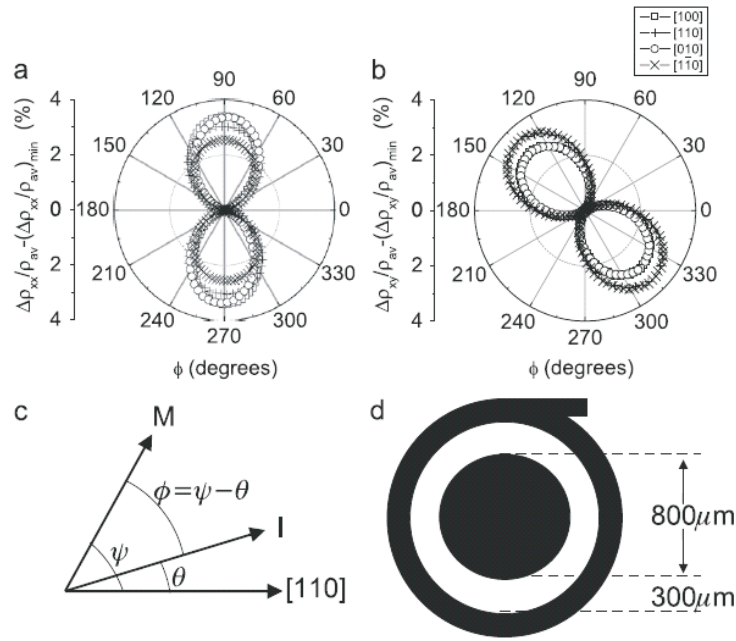


Figure 2.9: (a) Measured (at 4.2 K) longitudinal and (b) transverse AMR for as-grown 25 nm thick $\text{Ga}_{0.95}\text{Mn}_{0.05}\text{As}$ film as a function of the angle between magnetization in the plane of the film and the current. The direction of the current for each measurement is shown in the legend. The y-axis plots $\frac{\Delta\rho}{\rho_{av}}$ shifted with the minimum now at zero to illustrate the symmetries present in the data more clearly. (c) A pictorial illustration of the different angles as defined in the text. (d) Corbino geometry. (after Rushforth *et al.* [59])

excluded by symmetry consideration. It is also noted that the longitudinal AMR ($\frac{\Delta\rho_{xx}}{\rho_{av}}$) and the transverse AMR ($\frac{\Delta\rho_{xy}}{\rho_{av}}$) are not independent.

Figure 2.9(a) and (b) shows the fractional change in the longitudinal ($\frac{\Delta\rho_{xx}}{\rho_{av}}$) and transverse ($\frac{\Delta\rho_{xy}}{\rho_{av}}$) resistivities for a 25 nm thick $\text{Ga}_{0.95}\text{Mn}_{0.05}\text{As}$ Hall bars respectively for different current directions. These data can be used to extract the coefficients for the different contributions in the AMR as illustrated later in Figure 2.10. Figure 2.9(c) demonstrates the definition for the different angles with respect to the crystalline axis [110] as defined previously in Equations 2.20 and 2.21, while Figure 2.9(d) is a picture of the Corbino geometry used in Reference [59].

It is not possible to deduce the individual terms in Equations 2.20 and 2.21 with only one Hall bar. For example, a Hall bar orientated along $[\bar{1}\bar{1}0]$ gives $\phi =$

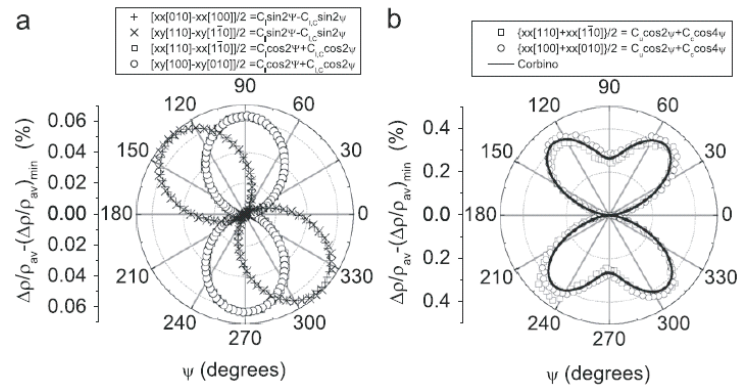


Figure 2.10: (a) An example showing how the individual components in the AMR can be extracted using different combinations of the data from Figure 2.9. (b) The purely crystalline terms of the AMR can be extracted from a combination of two orthogonal bars or by using a Corbino device. (after Rushforth *et. al.* [59])

$\psi + \pi/2$. Substituting this into Equations 2.20 and 2.21 generates $\frac{\Delta\rho_{xx}}{\rho_{av}} = (-C_I + C_U - C_{I,C}) \cos 2\psi + C_C \cos 4\psi$ and $\frac{\Delta\rho_{xy}}{\rho_{av}} = (-C_I + C_{I,C}) \sin 2\psi$ where the individual terms can be deduced only if $C_U = 0$. A combination of at least two Hall bar orientations are needed if the individual AMR components are to be extracted from the experimental data. This is illustrated in Figure 2.10.

Figure 2.10(a) demonstrates how the individual AMR components can be extracted from Hall bars with different orientations. For instance, the difference in the longitudinal resistivities in the [010] and [100] directions give a singular dependence on $\sin 2\psi$ with amplitude $2(C_I - C_{I,C})$ (cf. Equation 2.20), which is the same as the difference of transverse resistivities in the [110] and [1 $\bar{1}$ 0] samples. Using other combinations from the data, a $\cos 2\psi$ signal with amplitude $2(C_I + C_{I,C})$ can also be obtained. The close agreement in the same coefficients obtained by using different combinations points to a consistency between the data and the phenomenological analysis demonstrated by Rushforth and co-workers [59]. Figure 2.10(b) illustrates how the purely crystalline terms can be extracted. It can be done through a combination of the measurements from two orthogonal Hall bars, or obtained directly from the Corbino geometry since the non-crystalline terms are averaged to zero as the current flows in all radial directions in this geometry.

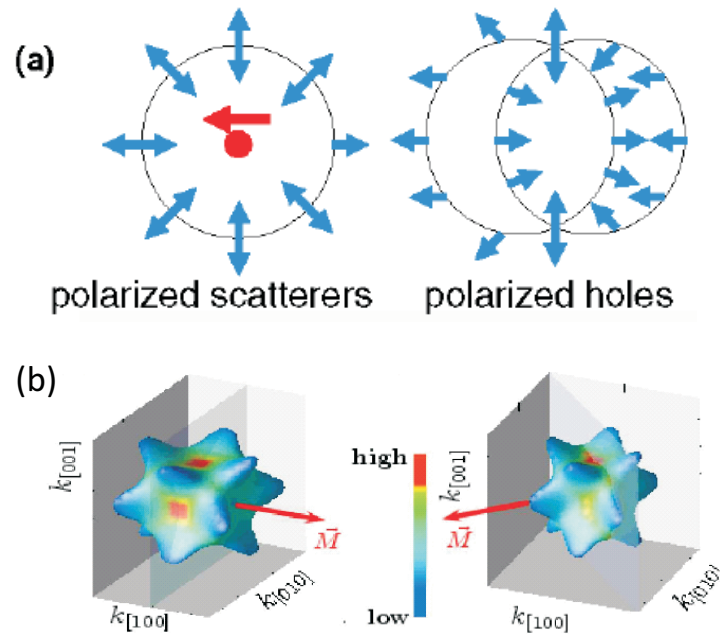


Figure 2.11: (a) Noncrystalline AMR in spherical bands: 2D cartoons of AMR mechanisms. (b) Noncrystalline and crystalline AMR on warped bands: calculated anisotropic scattering rates for $\hat{M} \parallel [100]$ and $[110]$ axes respectively. (after Rushforth *et. al.* [58])

Microscopic Origin of AMR

In dilute moment systems such as (Ga,Mn)As, there are two distinct microscopic mechanisms affecting the anisotropic carrier lifetimes [58]. One combines the spin-orbit coupling in the carrier band with polarization of randomly distributed magnetic scatterers and the other with polarization of the carrier band itself resulting in an asymmetric band-spin texture. These mechanisms act simultaneously in real systems, but theoretically they can be turned on and off independently.

Figure 2.11 portrays a 2D picture illustrating the AMR mechanisms for the non-crystalline contribution and the calculated anisotropic scattering rate for both the non-crystalline and the crystalline AMR on the 3D Fermi surface of the minority heavy-hole band in $\text{Ga}_{0.95}\text{Mn}_{0.05}\text{As}$ considering band-warping in the Kohn-Luttinger Hamiltonian.

By using the Boltzmann transport theoretical approach [61] with inputs from a six-band $\mathbf{k} \cdot \mathbf{p}$ description of the GaAs host valence band combined with the kinetic-

exchange model of the coupling to the local Mn_{Ga} d^5 - moments, the conductivities for $\hat{M}\parallel I$ and $\hat{M}\perp I$ can be evaluated [59]. Since AMR in (Ga,Mn)As is dominated by effect of the spin-orbit coupling of the carriers with polarization of randomly distributed magnetic scatterers, spin-splitting of the valence band is neglected in the following discussion. To simplify it further, only the noncrystalline AMR in the heavy-hole Fermi surfaces in the spherical, $\mathbf{s}\parallel\mathbf{k}$, spin-texture approximation is considered. This is possible since light hole bands give only a small contribution to the total conductivity [59]. In this model, the scatterers are approximated with a δ -function scattering potential $\propto (\alpha + \hat{M} \cdot s)$. Here \mathbf{s} and \mathbf{k} are the carrier spin operator and wave vector, and α represents the ratio of nonmagnetic (the δ Coulomb potential) and magnetic (the potential due to p-d exchange) parts of the impurity potential. Assuming a proportionality between conductivity and life-times of carriers with $\mathbf{k}\parallel\mathbf{I}$, the ratio of the conductivity for magnetization parallel to the current direction ($\sigma_{\hat{M}\parallel I}$) to the conductivity for magnetization perpendicular to the current direction ($\sigma_{\hat{M}\perp I}$) can be obtained (details of the derivation from Boltzmann theory can be found in reference [59]),

$$\sigma_{\hat{M}\parallel I}/\sigma_{\hat{M}\perp I} = (\alpha^2 + 1/4)(\alpha^2 + 1/12)/(\alpha^2 - 1/4)^2 \quad (2.22)$$

When the magnetic term in the impurity potential is much larger than the non-magnetic term ($\alpha \ll 1$), one expects $\sigma_{\hat{M}\parallel I} < \sigma_{\hat{M}\perp I}$ (this gives the positive AMR usually observed in metallic ferromagnets). As α increases, the sign of the non-crystalline AMR reverses at a relatively weak nonmagnetic potential ($\alpha = 1/\sqrt{20}$ in the model). The magnitude of $\sigma_{\hat{M}\parallel I}/\sigma_{\hat{M}\perp I}$ is maximized when the two terms are comparable ($\alpha = 1/2$), and it vanishes when the magnetic term is much weaker than the non-magnetic term ($\alpha \rightarrow \infty$). Physically, in the absence of a non-magnetic potential (when $\alpha = 0$), carriers experience the strongest scattering among all Fermi surface states when they move along \hat{M} (i.e. with \mathbf{s} parallel or antiparallel to \hat{M}), giving $\sigma_{\hat{M}\parallel I} < \sigma_{\hat{M}\perp I}$. When the non-magnetic potential is present, however, it can more efficiently negate the magnetic term for carriers moving along \hat{M} , This gives rise to a flip in the sign of AMR for relatively small α as shown in Figure 2.12. Since $\alpha < 1/\sqrt{20}$ is unrealistic for the magnetic acceptor Mn in GaAs [20, 61],

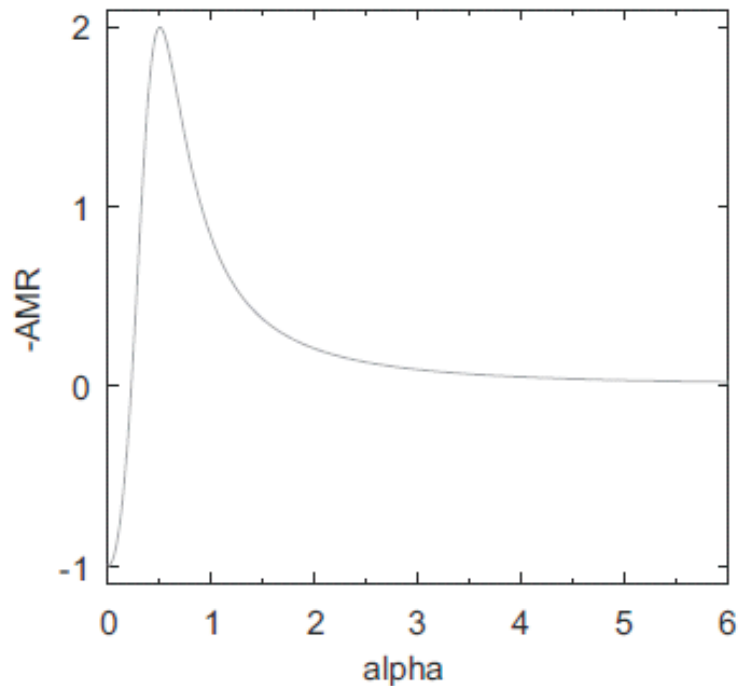


Figure 2.12: AMR as a function of the ratio between effective strengths of the non-magnetic and magnetic scattering. (after Rushforth *et. al.* [59])

$\sigma_{\hat{M}\parallel I} > \sigma_{\hat{M}\perp I}$ is obtained and is consistent with experiments [56, 57, 62].

Experimental studies on AMR in (Ga,Mn)As

Experimentally, AMR can be used as a sensor to infer information about the magnetic anisotropies in magnetic materials. This can usually be achieved in two ways [56–59, 62]. One is by sweeping an applied magnetic field in directions both in-plane and perpendicular-to-plane of the sample. This can be done with respect to different angles in relation to the magnetization, current and the crystallographic directions in the sample. Magnetic field sweeps can give an estimate of the switching field in the sample and the anisotropies of the material can then be inferred (refer to Chapter 5). The other method is by measuring the relative change in the magnetoresistance in a rotating saturation magnetic field. In a saturation magnetic field, the magnetization direction of the sample will be aligned with the direction of the applied field. In our experiments, for devices with in-plane magnetization and in the Corbino geometry (refer to Chapters 4, 5 and 6), the same underlying

symmetry breaking of the crystal fields for the magnetoresistance can be inferred for the magnetic anisotropy in such an rotating field experiment.

(Ga,Mn)As epilayers with broken cubic symmetry due to growth-direction lattice-matching strains are usually characterized by two AMR coefficients [20, 56]:

$$AMR_{op} = \frac{\rho_{xx}(M\|\hat{x}) - \rho_{xx}(M\|\hat{z})}{\rho_{xx}(M\|\hat{z})} \quad (2.23)$$

$$AMR_{ip} = \frac{\rho_{xx}(M\|\hat{x}) - \rho_{xx}(M\|\hat{y})}{\rho_{xx}(M\|\hat{y})} \quad (2.24)$$

where \hat{z} is the growth direction and the electrical current $\mathbf{I} \parallel \hat{x}$, and the longitudinal resistivity is denoted as ρ_{xx} . The non-zero coefficient AMR_{ip} is defined as the relative difference in resistivities in the in-plane $\mathbf{M} \perp \mathbf{I}$ and $\mathbf{M} \parallel \mathbf{I}$ configurations. In strained (Ga,Mn)As, AMR_{ip} is in general not equal to AMR_{op} , defined as the relative difference in resistivities in the $\mathbf{M} \perp$ plane and $\mathbf{M} \parallel \mathbf{I}$ configurations. An example of the experimental results obtained is shown in Figure 2.13 and 2.14.

Figure 2.13 shows the relative resistance of (Ga,Mn)As under both compressive strain (top two panels) and tensile strain (bottom panel) with respect to different orientations of the applied magnetic field. In particular, it is observed that $AMR_{op} > AMR_{ip}$ for compressive strained sample and $AMR_{op} < AMR_{ip}$ for tensile strained sample, consistent with the discussion in the previous section. The values of the magnetic field corresponding to the resistance maxima can also be associated with the anisotropy field (to the same order) in the system.

Sheet resistance as a function of magnetic field for a series of compressive strained as-grown and annealed (Ga,Mn)As with different doping concentrations is shown in Figure 2.14. The measured resistance is for different Hall bars along one of the $\langle 110 \rangle$ directions. The direction x is defined as the current direction, y as a direction in-plane but perpendicular to the current, and z is the perpendicular-to-plane direction. For low-doped samples (in the case of (a) $x = 0.011$), the resistance is higher for the in-plane magnetic field orientation than the perpendicular-to-plane orientation. In addition, the AMR occurs when the magnetic field is in-plane than when it is out-of-plane. This indicates that this sample possesses perpendicular-to-plane magnetic anisotropy, consistent with the discussion in Section 2.3.1 for

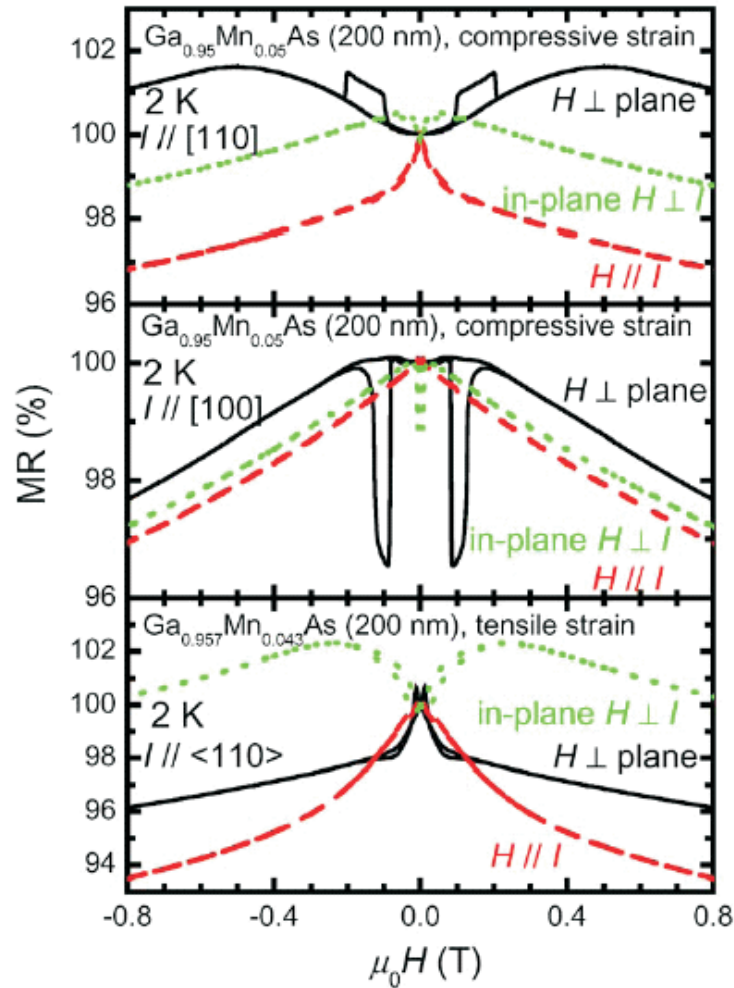


Figure 2.13: Upper and middle panel: experimental field-induced changes in the resistance of Ga_{0.95}Mn_{0.05}As grown on GaAs substrate under compressive strain for current along the [110] crystal direction (upper panel) and [100] crystal direction (middle panel) for three different orientations of the magnetic field. Lower panel: experimental magnetoresistance curves in Ga_{0.957}Mn_{0.043}As grown on (In,Ga)As substrate under tensile strain (current along the [110] crystal direction). (after Matsukura *et. al.* [56])

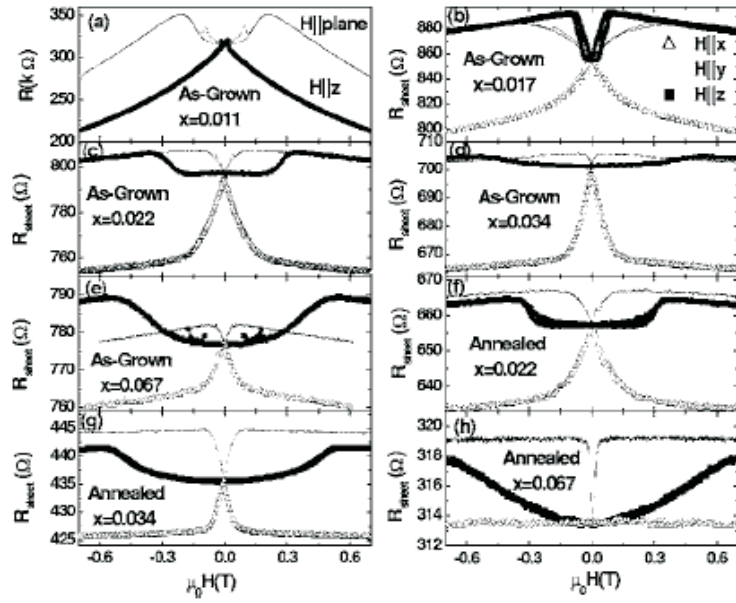


Figure 2.14: Sheet resistance as a function of magnetic field at $T = 4.2$ K for the as-grown $\text{Ga}_{1-x}\text{Mn}_x\text{As}$ thin films with different value of x : (a) $x = 0.011$, (b) $x = 0.017$, (c) $x = 0.022$, (d) $x = 0.034$, and (e) $x = 0.067$, for the annealed samples with (f) $x = 0.022$, (g) $x = 0.034$, and (h) $x = 0.067$, in three mutually orthogonal orientations of the magnetic field ($[110]$, $[1\bar{1}0]$ and $[001]$ directions). (after Wang *et al.* [62])

low-doped material.

2.5 Electrical control through gating

One has always desired the ability to control the properties of magnetic materials by external means from fundamental and technological viewpoints. As discussed in the above sections, diluted magnetic semiconductors (DMS) exhibit carrier-mediated ferromagnetism which provides a means for electrical control of their magnetic properties. Recent experiments have demonstrated electrical manipulation of ferromagnetic properties in both (In,Mn)As and (Ga,Mn)As, such as Curie temperature and coercive field, via gating [1,3]. The hole concentration of these epilayers with perpendicular magnetic anisotropy was altered using a surface-gated field-effect transistor (FET) arrangement. Changes in the hole concentration by the application of electric fields is expected to result in alterations of the hole-mediated ferromagnetic exchange interaction among localized Mn spins, and hence in the modification of ferromagnetic properties.

2.5.1 Field-effect Transistor

The replacement of the bulky vacuum tubes with the semiconductor junction transistor, in around 1948, marked the beginning of a rapid growth in transistor technology for the next few decades. Transistor is without a doubt one of the most important inventions in the 20th century. It is at the heart of all electronics, appearing in every corner of our lives. Transistors act as switches and by far, field-effect transistors are one of the most important devices included in integrated circuits (ICs).

In a FET, current flows between two electrodes (source and drain) and is modulated by voltage applied through a third electrode, the gate. The bias on the gate electrode changes the free carrier density within the conducting channel, thereby regulating the current flowing through the source and drain. One way of producing a variable surface charge density in the semiconductor substrate is by using the Metal-Insulator-Semiconductor (MIS) capacitor structure. The structure of the MIS diode is shown in Figure 2.15. There are three components, a metal gate electrode, an

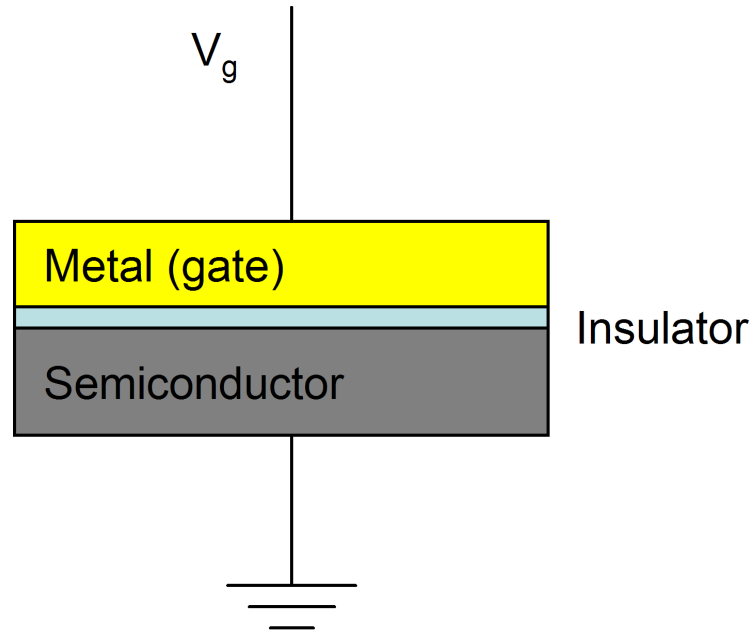


Figure 2.15: The structure of a Metal-Insulator-Semiconductor (MIS) capacitor. The metal is electrically isolated from the semiconductor by the insulating dielectric. V_g here is the gate voltage.

insulator and a semiconductor. The bottom Ohmic connection to the semiconductor is grounded while the gate has a bias V_g applied to it. Charges of opposite sign to the gate-bias are attracted to the semiconductor-insulator interface. The FET is then fabricated by adding two electrical contacts on the semiconductor side of the MIS structure. This provides a means for electrical control of the magnetization in DMS statically with gating.

2.5.2 P-N junction gating

P-N junctions are elementary building blocks in electronics and are used in diodes, varistors, varactors etc. For the application of electrical control of magnetic properties of (Ga,Mn)As, it is an attractive option as it allows control of the width of the depletion region with applied voltages. For ultra-thin samples similar to those used in the experiments (refer to Chapters 4, 5 and 6), the width of the depletion region is comparable to the thickness of the (Ga,Mn)As epilayer, enhancing the efficiency in the effective gating.

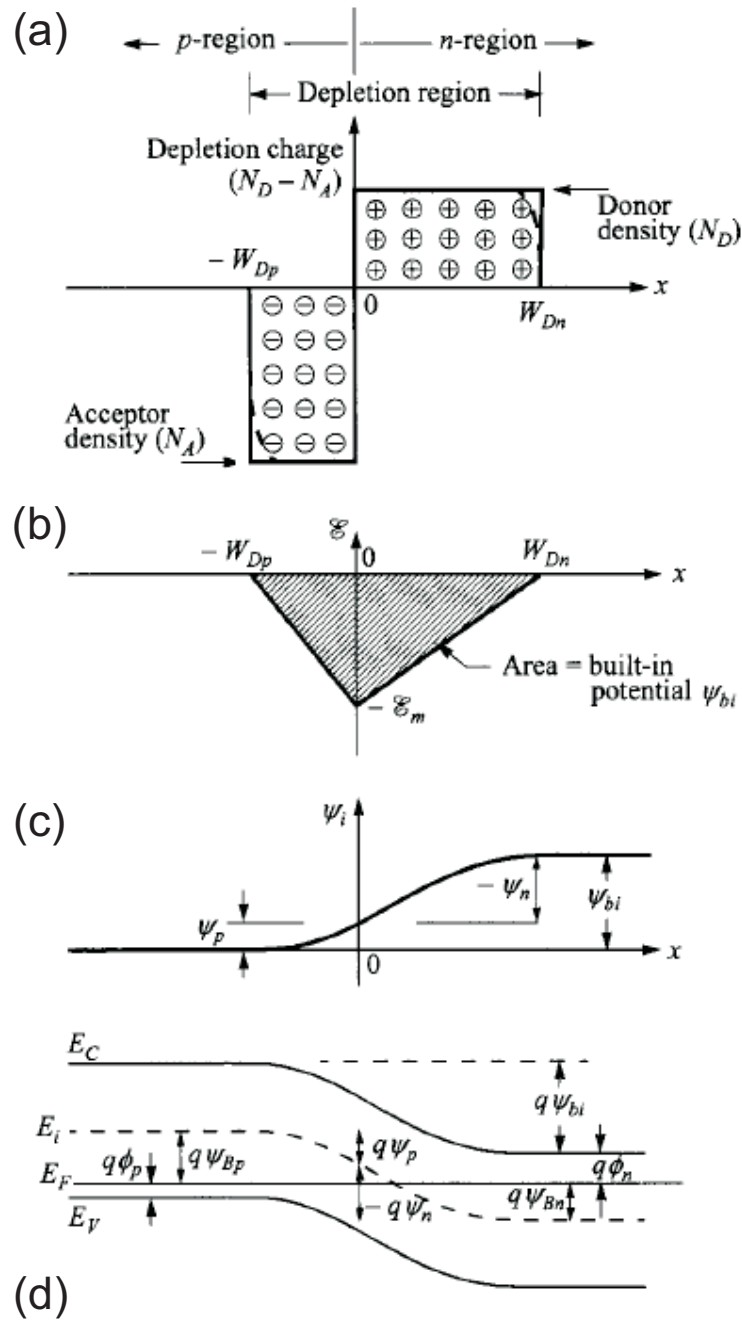


Figure 2.16: Abrupt p-n junction in thermal equilibrium. (a) Space-charge distribution. Dashed lines indicate corrections to depletion approximation. (b) Electric-field distribution. (c) Potential distribution where ψ_{bi} is the built-in potential. (d) Energy-band diagram (after Sze *et. al.* [63]).

To simplify the numerical analysis, an abrupt junction (or full-depletion approximation) is assumed here. An abrupt junction is shown in Figure 2.16. It consists of a depletion region around the metallurgical junction with well-defined edges and assumes that the transition between the depleted and the neutral region is abrupt.

At thermal equilibrium without current flow (can also be applied to reverse-bias), the current equation of drift and diffusion gives rise to [63]

$$J_n = 0 = q\mu_n(n\varepsilon + \frac{kT}{q} \frac{dn}{dx}) = \mu_n n \frac{dE_F}{dx} \quad (2.25)$$

or

$$\frac{dE_F}{dx} = 0 \quad (2.26)$$

where E_F is the fermi energy. This implies that the Fermi level must be constant throughout the sample. The built-in potential ψ_{bi} is then given by

$$q\psi_{bi} = E_g - (q\phi_n + q\phi_p) \quad (2.27)$$

where E_g is the band gap energy, ϕ_n and ϕ_p are the Fermi potentials from the conduction-band edge in the n-type semiconductor and from the valence-band edge in the p-type semiconductor respectively. This is illustrated in Figure 2.16(d). This quantity will be useful in the calculation of the depletion width later.

To calculate the field and potential distribution inside the depletion region, we start from the electrostatic Poisson equation which gives

$$-\frac{d^2\psi_i}{dx^2} = \frac{d\varepsilon}{dx} = \frac{q}{\epsilon_s} [N_D^+(x) - n(x) - N_A^-(x) + p(x)] \quad (2.28)$$

where $N_D^+(x)$, $N_A^-(x)$, $p(x)$ and $n(x)$ is the concentrations of ionized donors, ionized acceptors, free holes and free electrons respectively. By integrating the Poisson equation twice (details shown in [63]) and assuming complete ionization, the potential across the different regions in the depletion region can be found as

$$\psi_p = \frac{qN_A W_{Dp}^2}{2\epsilon_s} \quad (2.29)$$

$$|\psi_n| = \frac{qN_D W_{Dn}^2}{2\epsilon_s} \quad (2.30)$$

where ψ_p and ψ_n are the potentials across the p-region and n-region respectively, W_{Dp} and W_{Dn} are the depletion widths across the p-region and n-region respectively and ϵ_s is the dielectric constant of the semiconductor.

It is also noted that in thermal equilibrium, the electric field in the neutral regions of the semiconductor must be zero, so that the total negative charge per unit area in the p-side must be equal to the total positive charge per unit area in the n-side:

$$N_A W_{Dp} = N_D W_{Dn} \quad (2.31)$$

Another useful relationship is obtained by relating the potential across the depletion layer width to the applied voltage. The combination of both relations yields a solution for W_{Dp} and W_{Dn} , from which all other parameters can be obtained.

$$\psi_{bi} = \psi_p + |\psi_n| \quad (2.32)$$

P-I-N Junction

The above discussion for the p-n junction can be extended to that for a p-i-n junction. A p-i-n junction is similar to a p-n junction, but contains in addition an intrinsic or un-intentionally doped region with thickness W_u , between the n-type and p-type layer. It is especially helpful in the following experiments to insert this additional insulating layer so as to minimize the leakage current through the backgate in the FET device during gating.

The analysis for the p-i-n junction is similar to that of a p-n diode, although the potential across the undoped region must be included in the analysis [64]. Equation 2.32 then becomes:

$$\psi_{bi} + V_a = \psi_p + \psi_u + |\psi_n| \quad (2.33)$$

where V_a is the applied voltage from the p-region and ψ_u is the potential across the undoped region.

The above equation can be solved analytically by substituting equation 2.29 and 2.31 and an appropriate form for ψ_u to get an expression for the depletion width in the p-doped region.

$$W_{Dp} = -\frac{\epsilon_s}{\epsilon_u} \left(\frac{N_D}{N_A + N_D} \right) W_u + \left[\left(\frac{\epsilon_s}{\epsilon_u} \frac{N_D}{N_A + N_D} W_u \right)^2 + 2\epsilon_s \left(\frac{N_D}{qN_A(N_A + N_D)} \right) (\psi_{bi} - V_a) \right]^{\frac{1}{2}} \quad (2.34)$$

where ϵ_u is the dielectric constant of the undoped region and assuming that the dielectric constant of the p-doped and n-doped region (i.e. $\epsilon_p \sim \epsilon_n = \epsilon_s$) is similar.

The above equation can be extended to test the viability of the p-n junction FET approach to low-voltage gating of thin (Ga,Mn)As films.

For the wafer D036 used in Chapter 4, the expression can be rewritten as:

$$W_{Dp} = -\frac{\epsilon_{GaAs}}{\epsilon_{AlAs}} \left(\frac{n}{n+p} \right) W_{AlAs} + \left[\left(\frac{\epsilon_{GaAs}}{\epsilon_{AlAs}} \frac{n}{n+p} W_{AlAs} \right)^2 + 2\epsilon_{GaAs} \left(\frac{n}{p(p+n)} \right) (\Delta_{GaAs} + V_g) \right]^{\frac{1}{2}} \quad (2.35)$$

where ϵ_{GaAs} and ϵ_{AlAs} are the dielectric constants for GaAs and AlAs respectively, n is the doping concentration of the n-region, p is the hole concentration in the p-region, W_{AlAs} is the AlAs barrier width, Δ_{GaAs} is the GaAs band gap and V_g is the applied gate voltage [4].

The potential of the insulating layer, ψ_u , used in Equation 2.33 can be expressed as

$$\psi_u = \frac{qN_A W_{Dp} W_u}{\epsilon_u} \quad (2.36)$$

For the wafer E028 used in Chapters 5 and 6, the potential across the insulating layer can now be expressed as

$$\psi_u = \frac{qN_A W_{Dp} W_u}{2\epsilon_{AlAs}} + \frac{qN_A W_{Dp} W_u}{2\epsilon_{AlGaAs}} \quad (2.37)$$

$$= \frac{qN_A W_{Dp} W_u}{2} \left(\frac{\epsilon_{AlAs} + \epsilon_{AlGaAs}}{\epsilon_{AlAs} \epsilon_{AlGaAs}} \right) \quad (2.38)$$

$$= \frac{qN_A W_{Dp} W_u}{\epsilon_{eff}} \quad (2.39)$$

where the effective dielectric constant, ϵ_{eff} , can be expressed as

$$\epsilon_{eff} = \frac{2\epsilon_{AlAs}\epsilon_{AlGaAs}}{\epsilon_{AlAs} + \epsilon_{AlGaAs}} \quad (2.40)$$

2.5.3 Polyelectrolyte gating

To enhance the effects of gating on the magnetic properties of (Ga,Mn)As, one needs to be able to manipulate a larger change in the density of holes in the epilayer. For common gating, one usually turns to a dielectric with a larger dielectric constant and minimizing the thickness of the dielectric. One novel alternative is to use polymer electrolyte which acts as a high-capacitance insulator.

In a recent report [65], an electrolytic double layer was used for electric-field induced modification of magnetism in FePt and FePd. The electrolyte propylene

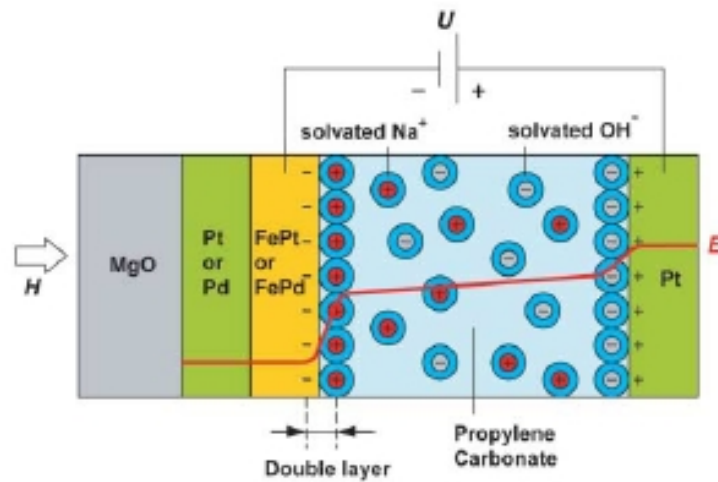


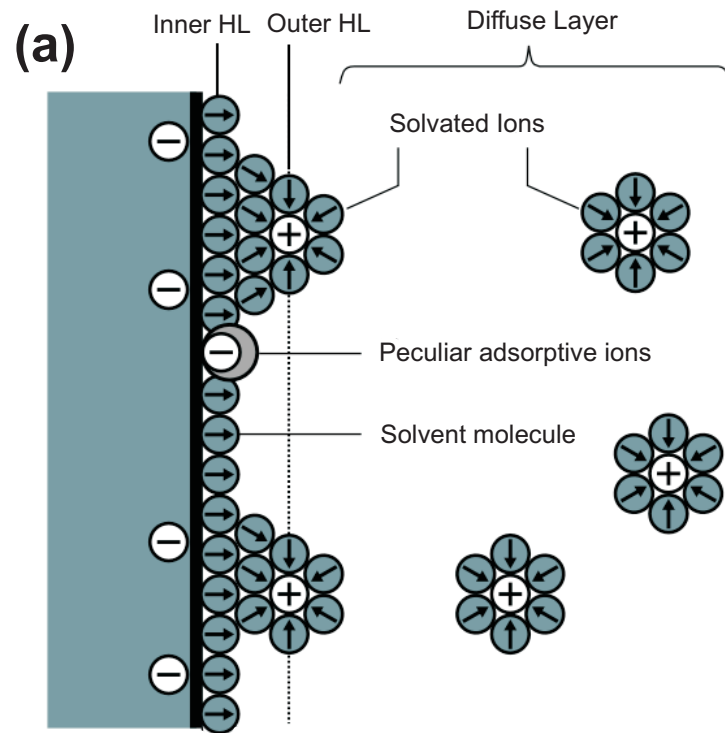
Figure 2.17: Schematic of the electrolytic cell containing the FePt or FePd film within an applied magnetic field H . The potential profile E due to the applied potential U is shown by the red line. The potential drop at the Pt electrode side is much lower (as compared to that of the sample surface) due to the large area of the Pt electrode. Solvated Na^+ present to create the electrolytic double layer (after Weisheit *et. al.* [65]).

carbonate (PC) with solvated Na^+ and OH^- ions was used to create a potential difference of up to 1 V on the FePt or FePd layer (refer to Figure 2.17). This is an elegant approach to overcome the difficulties faced in preparing a thin and homogeneous dielectric layer free of pinholes.

Solid polymer electrolytes consist of a salt dissolved in a polymer matrix. In polymer electrolytes, very high polarization is achieved by virtue of mobile ions that translate in response to electric fields. The specific capacitances are extremely large and can exceed $10 \mu\text{Fcm}^{-2}$ [66], which is significantly greater than values obtained with other materials (for example, a 50-nm-thick layer of a typical dielectric such as aluminium oxide has a specific capacitance of $0.85 \mu\text{Fcm}^{-2}$ [3]).

Electric double layer

The high-capacitance nature of polyelectrolyte gating arises from the electric double layers (EDL) formed on both sides of the electrodes when it is polarized. A schematic



Schematic diagram of the interface between electrode and electrolyte

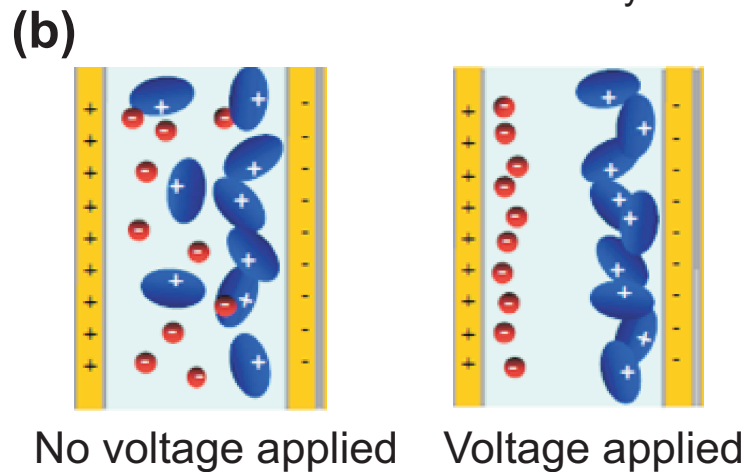


Figure 2.18: (a) A schematic diagram of the interface between electrode and electrolyte. (b) A ‘cartoon’ picture showing the formation of the EDL when a voltage is applied through the electrodes. When there is no applied voltage, the ions are randomly distributed (left panel). Upon the application of a voltage across the electrodes, the ions are redistributed to form the EDL.

diagram of the formation of EDL at the interface of the electrode and the electrolyte is shown in Figure 2.18. In the EDL model, which was first proposed by H. Helmholtz in the 1850s, no electron transfer reactions are assumed to occur at the electrode and the solution is composed only of electrolyte. The interactions between the ions in solution and the electrode surface were assumed to be electrostatic in nature and resulted from the electric surface charge on the electrode. This surface charge creates an electric field, causing a redistribution of ions close to the electrode surface in order for the interface to remain electrically neutral in equilibrium. The attracted ions are assumed to approach the electrode surface and form a layer, known as the Helmholtz layer (HL), to balance the surface charges. The net electric charge in this screening diffuse layer is equal in magnitude to the net surface charge, but has the opposite polarity. As a result the complete structure is electrically neutral. The overall result is two layers of charge (the double layer) and a potential drop which is confined to this diffuse layer in the solution. The result is analogous to an electrical capacitor which has two plates of charge separated by some distance, d , given by the thickness of the EDL.

An illustration of the potential across the counter-charge layer formed at the interface of the electrode and the electrolyte is shown in Figure 2.19. The characteristic thickness of each of the EDL is given by the Debye length which is:

$$\kappa^{-1} = \left(\frac{\epsilon_0 \epsilon_r k T}{2 N_A e^2 I} \right)^{\frac{1}{2}} \quad (2.41)$$

where ϵ_r is the dielectric constant of the electrolyte, k is the Boltzmann constant, T is temperature, N_A is the Avogadro's number and I is the ionic strength of the electrolyte.

Mechanisms of transistor action

In addition to the electrostatic gating common in field-effect transistors, electrochemical doping is also possible when an electric field is applied in a polyelectrolyte-gated (PEG) FET structure. Figure 2.20 illustrates the two different mechanisms at work during transistor actions in the PEG-FET [67]. The major factor in deciding which mechanism dominates is the permeability of the semiconductor layer to the

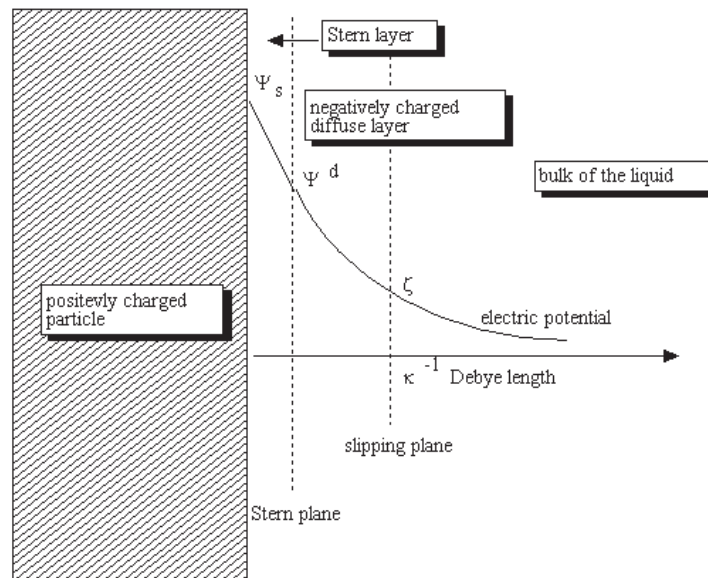


Figure 2.19: An illustration of potential across the electric layer formed at the interface of the electrode and the electrolyte. κ^{-1} shown in the diagram is the Debye length which is the characteristic thickness of the counter-charge layer (after Wikipedia).

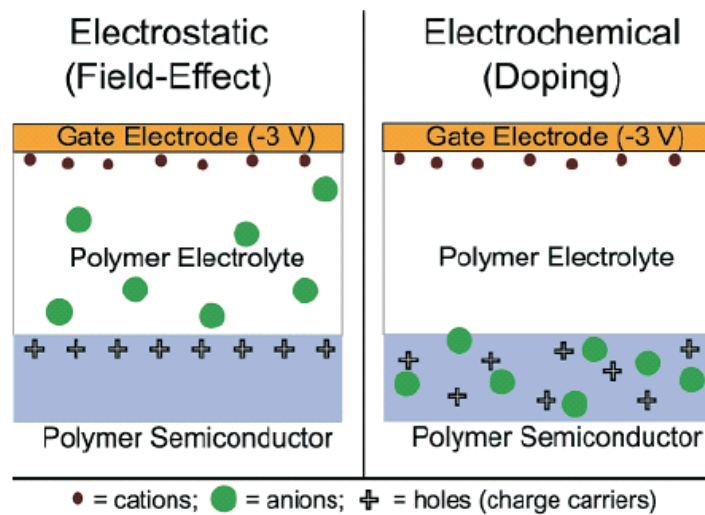


Figure 2.20: Schematic cross-sections of a polyelectrolyte gated-FET channel showing the key difference in the extent of ion penetration between electrostatic charging (left) and electrochemical doping (right) as possible operating mechanisms. (after Panzer *et. al.* [67]).

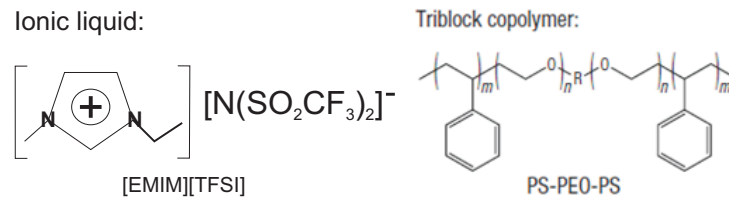


Figure 2.21: Chemical structure of the ionic liquid and triblock copolymer ion gel components: 1-ethyl-3-methylimidazolium bis(trifluoromethylsulfonylethyl)imide ([EMIM][TFSI]) and poly(styrene-block-ethylene oxide-block-styrene)(PS-PEO-PS). (after Cho *et. al.* [68]).

ions in the polymer electrolyte.

As shown in Figure 2.20, electrochemical doping consists of ions migration into the semiconductor and constitutes an electrochemical reaction, or doping process. In a electrochemical transistor, this migration of ions can increase the conductivity in the polymer semiconductor by stabilizing charges in its backbone. On the other hand, if ions do not penetrate into the semiconductor during FET operation, electrostatic gating is achieved. The current in the semiconductor channel can be modulated by the electrostatic induction of charge carriers in response to a high electric field at the semiconductor/polymer electrolyte interface. An electric double layer is formed in this case.

The ionic liquid 1-ethyl-3-methylimidazolium bis(trifluoromethylsulfonylethyl)imide ([EMIM][TFSI]), which has relatively large cations and anions compared to the atomic structure of (Ga,Mn)As, was chosen for experiments carried out in Chapter 6 to minimize this electrochemical doping effect.

Ionic gel

One special class of polymer electrolyte is the ionic gel. An ionic gel consists of an ionic conducting liquid immobilized inside a polymer matrix. To create an ionic gel, a block copolymer is polymerized along with an ionic liquid so that self-assembled nanostructures where the ions are selectively soluble. The ionic gel electrolyte used in the experiment (refer to Chapter 6) is formed by gelation of the 1-ethyl-

3-methylimidazolium bis(trifluoromethylsulfonyl)imide ([EMIM][TFSI]) mixed with poly(styrene-block-ethylene oxide-block-styrene) (PS-PEO-PS) tri-block copolymer, dissolved in acetonitrile.

Using equation 2.41, and substituting the appropriate value of $\epsilon_r = 23$ for [EMIM][TFSI] [69] and using a similar ionic concentration as used in Chapter 6, the value of $\sim 1.4\text{\AA}$ is obtained for each of the double layers, which is in the correct order of the estimated value of 7\AA from experiments [69].

2.6 Curie temperature

The Curie temperature (T_C) is an important parameter in a ferromagnetic material as it marks the onset of its ferromagnetism. In a simplified picture, for low temperatures well below T_C , magnetic moments are aligned parallel within magnetic domains in the ferromagnetic state. As the temperature increases toward T_C , spin alignment within each domain decreases due to thermal fluctuations. Above T_C , the material is paramagnetic so that magnetic moments are in a completely disordered state.

Measurement of the Curie temperature can be achieved in mainly two ways: One is from the temperature-dependence of the remnant magnetization measurement using superconducting quantum interference device (SQUID) magnetometry and the other is from Arrott plots obtained from anomalous Hall measurements [1, 7, 70–72]. Recently, Novak and co-workers have realized the Curie point singularity in the temperature derivative of resistivity ($d\rho/dT$) in (Ga,Mn)As [70] which allows measurement of T_C using direct transport measurement data.

2.6.1 Curie point singularity in $d\rho/dT$ of (Ga,Mn)As

In magnetic semiconductor with dense moment and low carrier density such as Eu-chalcogenide magnetic semiconductors, the peak in the resistivity $\rho(T)$ observed has been explained by the coherent scattering from long wavelength spin fluctuations [73]. The long wavelength limit of the spin-spin correlation function can be justified by the small carrier density and corresponding small Fermi wave vector k

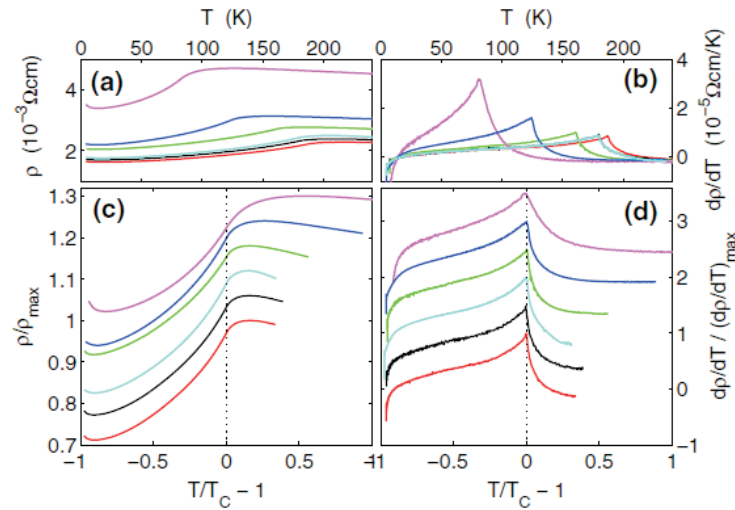


Figure 2.22: (a) Resistivities $\rho(T)$ and (b) temperature derivatives dR/dT for optimized (Ga,Mn)As films (of thicknesses between 13 and 33 nm) prepared in Prague and Nottingham MBE systems. Data normalized to maximum $\rho(T)$ and dR/dT are plotted in (c) and (d), respectively. Curves in (a), (c), and (d) are ordered from top to bottom according to increasing Mn doping and T_C : 4.5% Mn-doped sample with $T_C=81$ K, 6% with 124 K, 10% with 161 K, 12% with 179 K (Prague and Nottingham samples), and 12.5% doped sample with 185 K Curie temperature. In (c) and (d), curves are offset for clarity. (after Novak *et. al.* [70])

in the systems.

For high carrier density transition metal ferromagnets such as Ni, the long wavelength limit of the spin-spin correlation function no longer applies. In a seminal work by Fisher and Langer [74], the singularity at T_C for these transition metal ferromagnets was found instead to occur in $d\rho/dT$ and is associated with the critical behaviour of correlations between nearby moments.

Novak and co-workers [70] extended this argument to (Ga,Mn)As, which has dilute magnetic moment and generally high carrier density. They found that T_C in (Ga,Mn)As can also be estimated from the singularity in $d\rho/dT$. Figure 2.22 shows experimental results they have gathered from a wide range of (Ga,Mn)As wafers with different Mn-doping levels ranging from 4.5% to 12.5%. The plots in Figure 2.22 demonstrates that the maxima in the resistivities ($\rho(T)$) of the the

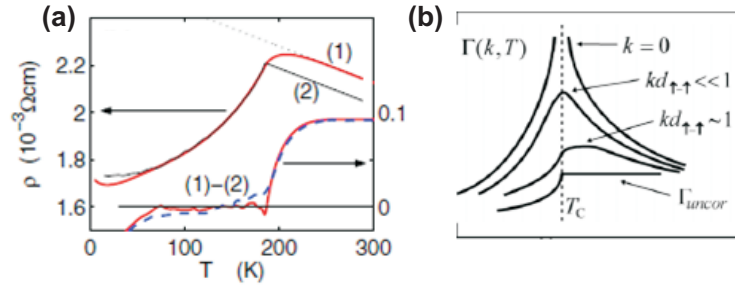


Figure 2.23: (a) Measured resistivity $\rho(T)$ at zero field (1), the fit of $\rho(T)$ by $\rho_{fit}(T) = c_0 + c_{nm}T + c_{m2}M^2(T) + c_{m4}M^4(T)$ (2), and the difference $\rho(T) - \rho_{fit}(T)$ for the 0 (red) and 1000 (blue-dotted) Oe-field measurements. (b) Schematics of the uncorrelated part and Fourier components of the spin-spin correlation function for different ratios between the wave vector and inverse of the spin separation. (after Novak *et. al.* [70])

$d\rho/dT$ singularities for different wafers with a range of T_C from 81 to 185 K.

In reference [70], Novak and co-workers have also explored the phenomenology of the $d\rho/dT$ singularity in T_C . Figure 2.23 demonstrates the two dominant contributions to the resistivity approaching T_C from two directions: from below T_C ($T \rightarrow T_C^-$) and above T_C ($T \rightarrow T_C^+$). The diagram on the left in Figure 2.23 shows results of resistivities for the corresponding measurements in 0 Oe (red) and 1000 Oe (black) fields. A useful insight can be gained by fitting $\rho_{fit}(T) = c_0 + c_{nm}T + c_{m2}M^2(T) + c_{m4}M^4(T)$, which contains both contributions from the non-magnetic part in the temperature dependence $c_{nm}T$, and the uncorrelated scattering part ($c_{m2}M^2(T) + c_{m4}M^4(T)$) assuming a M^2 expansion dependence. The remaining magnetic contribution, $\rho_m(T)$, to $\rho(T)$ can be found by subtracting the fit from the actual measured data as shown in the left panel of Figure 2.23. The nose dive of $\rho_m(T)$ on the paramagnetic side suggests that the measured peak in the resistivity originates from a singular behaviour at $T \rightarrow T_C^+$.

To explore the mechanism for the resistivity contribution approaching from $T \rightarrow T_C^+$, the theory of the spin-spin coupling between local Mn moments and valence band holes, which is central to the ferromagnetism in (Ga,Mn)As, is invoked. When treated in the Born approximation, the interaction yields a carrier scattering rate

from magnetic fluctuations which is proportional to the static spin-spin correlation function $\Gamma(R_i, T) \sim J^2[\langle S_i \cdot S_0 \rangle - \langle S_i \rangle \cdot \langle S_0 \rangle]$. The diagram on the right in Figure 2.23 is a schematic of the uncorrelated part (Γ_{uncor}) and Fourier components ($\Gamma(k, T)$) of the spin-spin correlation function for different ratios of the wave vector to the inverse of the spin separation. At small wave vectors (i.e. long wavelength), $\Gamma(k, T)$ has a peak near T_C . For k similar to the inverse separation of the local moments (in the case of (Ga,Mn)As), $kd_{\uparrow-\uparrow} \sim 1$, the peak broadens into a shoulder, with the singular behaviour at T_C in the $d\rho/dT$.

This method is especially useful in determining the T_C for patterned samples or devices since their small dimensions are often restrictions preventing the use of other techniques such as SQUID magnetometry. It has been used extensively in the later experimental chapters (refer to Chapters 5 and 6).

Chapter 3

Materials and experimental methods

To study the effect of gating on compressively strained (Ga,Mn)As epilayers with more complex in-plane competing cubic and uniaxial magnetic anisotropies, different gating field effect transistor (FET) structures were made on a number of different (Ga,Mn)As wafers. Various standard experimental procedures such as photolithography, wet-etching and metal evaporation were used. There are three main stages to the fabrication of a FET device. They are mesa definition, bond pads deposition and bonding. For the case of top-gating, ionic gel is applied after the thermal evaporation of the contact pads. Much difficulty was faced during the fabrication process, especially with bond pads deposition and the subsequent bonding procedure.

The first section of this chapter is dedicated to the materials and the experimental methods used in the fabrication of the FETs. The second section of this chapter is focused on the experimental techniques employed in the various low-temperature measurements made as reported in Chapters 4, 5 and 6. The equipment used for magnetotransport measurements is also described.

3.1 Materials used

As detailed in Chapter 4, preliminary studies on ultra-thin (Ga,Mn)As were carried out to understand what effects gating has on its magnetic and electric transport properties. These materials exhibit an in-plane magnetic anisotropy. Ultra-thin (Ga,Mn)As of about 5 nm was used for the experiments detailed in Chapters 4, 5 and 6 to maximize the capacitance that can be achieved in the transistor devices. Moreover, electrical gating is largely a surface effect and hence larger gating-induced effects are expected for thin films.

Ultra-thin (Ga,Mn)As layers with various Mn concentrations were grown by LT-MBE by Vit Novák at the Institute of Physics in Prague. Two wafers labeled D036 and E028 were processed. Devices made from D036 were used in Chapter 4 whereas the improved E028 wafer was used for both Chapter 5 and 6. The parameters of the wafers are summarized in Table 3.1.

	D036	E028
x [%]	8.0	2.5
T_C [K]	~ 40	~ 28
t [nm]	4	5

Table 3.1: Wafer parameters for the two ultra-thin (Ga,Mn)As samples: Mn concentration x , Curie temperature T_C (as measured by SQUID magnetometry in Prague on the unpatterned wafers) and thickness t are reported.

The wafer D036 is grown on top of a 20 nm undoped AlAs barrier followed by a heavily n-doped epitaxial GaAs layer ($n = 2 \times 10^{18} \text{ cm}^{-3}$) which acts as the gate electrode. An improved version, E028, is grown on top of a 10 nm AlAs spacer layer with another 10 nm $\text{Al}_{0.3}\text{Ga}_{0.7}\text{As}$ spacer layer next to the n-GaAs. The differential spacer layer is engineered to further minimize leakage current. 2 nm of undoped GaAs is also grown on top of the (Ga,Mn)As epilayer for E028. This acts as a protective layer to prevent unintended chemical etching of the (Ga,Mn)As during the fabrication processes.

Figure 3.1 shows the SQUID measurement of the in-plane remanent magnetiza-

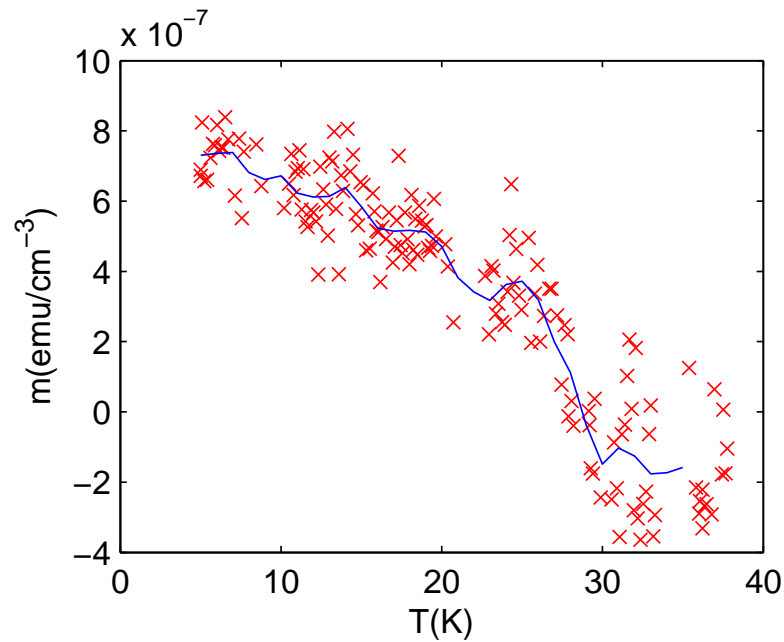


Figure 3.1: SQUID measurement of the temperature dependence of the remanent magnetization for the wafer E028. In-plane remanent magnetisation persists up to about 28 K. The measurement was performed by Kamil Olejník.

tion of wafer E028 with temperature. It gives a measured T_C of ~ 28 K, as shown in Figure 3.1. The Curie temperature of the layer E028 was again estimated after device processing from the singularity in the temperature derivative of the resistance as discussed in Chapter 5, and the results are found to be consistent.

3.2 Device fabrication

Conventional techniques for the processing of III-V semiconductors were employed for the fabrication of the devices used in the following studies. The device layout is first transferred on a chip by means of lithography, usually photolithography in our case. The pattern is then reproduced either by etching or by evaporating thin metal layers. Finally, the processed chip is scribed to divide up the devices which are then packaged and wire-bonded. The process reported in this section describes the typical fabrication of the (Ga,Mn)As devices used in the study reported in Chapters 4, 5 and 6. A summary of the fabrication steps for the devices made are reported in Appendix A.1.

3.2.1 Designing the devices

Before the actual chemical processing of the devices, accurate layouts were first designed using AutoCAD. In AutoCAD, the topography of the device is specified by polygonal shapes that belong to different layers. Each layer corresponds to a particular stage of the process. In the case of electron beam lithography, all the patterns belonging to the same layer will be written on the sample in the same lithographical process, with the same exposure dose.

In our study, the AutoCAD design was used in the fabrication of the optical mask employed in the photo-lithographical patterning of the device. The main restriction of photo-lithography is the limitation on the smallest feature size one can achieve, which is theoretically limited by optical diffraction. The maximum resolution is usually of the order of the wavelength of the UV light used. However, in most cases, the minimum size is usually hard to achieve due to many other environmental factors such as the photo-resist used and the contact between the sample (with the photo-resist) and the mask. As such, the minimum feature size of the mask is limited to $2\ \mu\text{m}$. An example of the layout file of the mask used in this study is shown in Figure 3.2.

As shown in Figure 3.2, the majority of the devices used are of the Corbino geometry. The advantages of using the Corbino design is that it keeps the resistance of the device low enough even at cryogenic temperatures so that measurements with a low noise ratio can still be made. This is possible with the short effective channel length, which is dependent on the ratio of the inner diameter and the outer diameter of the Corbino disc.

3.2.2 Making the device

After designing the layout for the various processes of the device and making our optical mask, we can proceed to the fabrication of the devices. The fabrication involves mainly three steps: optical lithography, etching and metallic bond pads deposition.

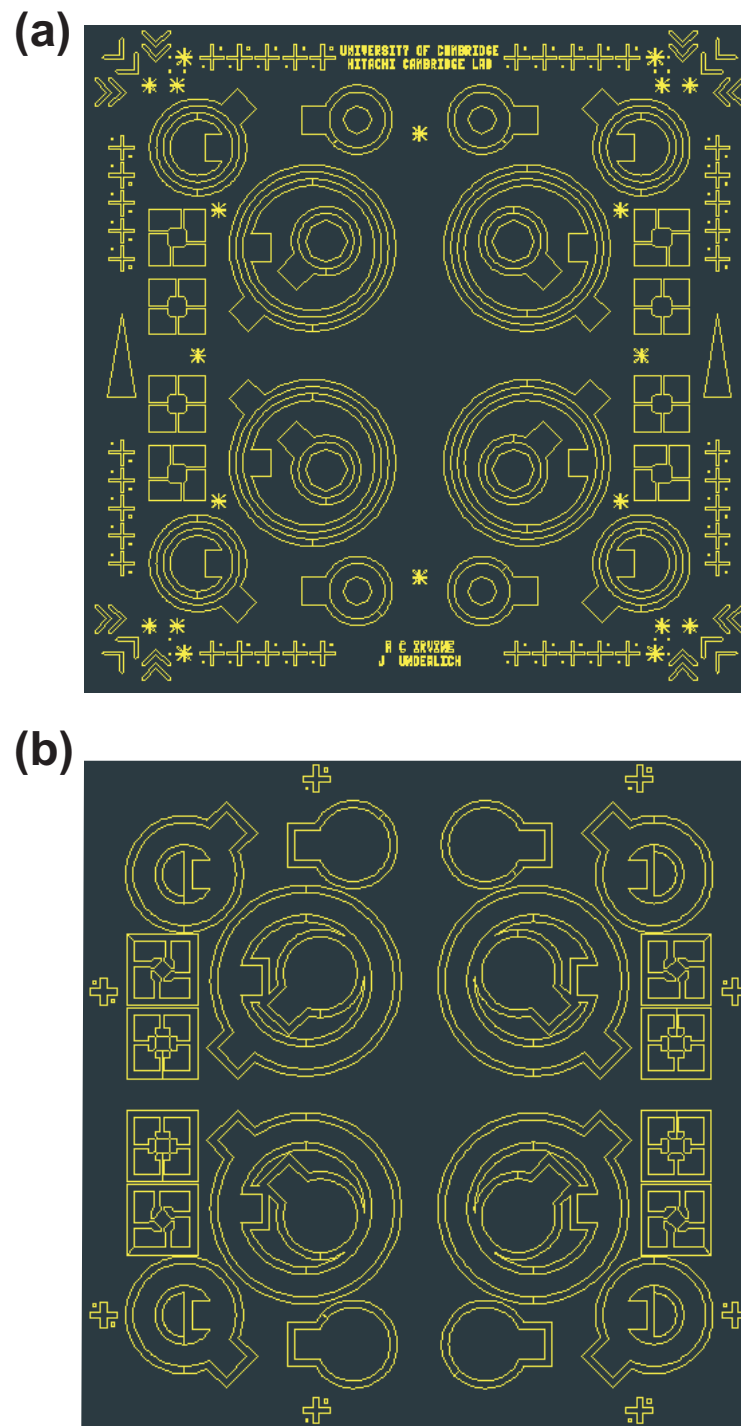


Figure 3.2: An example of the photolithography mask used for (a) bond pads deposition and (b) device patterning in the fabrication of devices made in this study.(drawn by Dr. A. Irvine)

Optical lithography

Before proceeding with any lithography step, the chip is cleaned by immersing it in an ultrasonic bath: first in acetone, then in iso-propanol (IPA) for 5 minutes each. The chip is then dried by baking in an oven at 80°C for 15 minutes before spinning the UV-III resist on the sample surface. It is important to mention that any thermal processes are kept to as low a temperature and as short a time as possible during the multi-staged fabrication process since samples were grown at low temperature (200°C to 300°C). Any unnecessary thermal annealing may change the magnetic or transport properties of the sample as outlined in Chapter 2. However for thin-films below the thickness of 15 nm (used mainly in the experiments), this is not so critical as no Mn_I can be detected [23].

In all the following processes, the positive photo-resist UV-III is spun at 5000 rpm for 40 seconds to ensure a uniform layer of resist. The thicknesses of the resist were measured with a Dektak profilometer. The commonly employed optical resist S1813 cannot be used in the fabrication of (Ga,Mn)As, as it was found that its developer solution, M319 etches (Ga,Mn)As. Therefore, for optical lithography, the resist UV-III has been used because it can be developed in another developer solution, CD-26.

After spinning the UV-III photo-resist, the sample is baked at 150°C on a thermal hot plate for 1 minute. This is necessary to dry the resist as well as to prepare it for UV exposure. The sample is then exposed to UV radiation for 2 minutes. After the UV exposure, the sample is again baked at 150°C on a thermal hot plate for 1 minute. After the photo-lithography, the resulting pattern is developed in a solution of MICROPOSITTM MFTM CD-26 developer at 20°C for 30 s, before being rinsed in de-ionized water. This development time has been optimized since over-development of the pattern will give rise to rounded corners and loss in resolution, and under-development will not give the desired pattern with underlying resist on the supposedly exposed areas.

Etching

Reactive Ion Etching (RIE) is a process to create trenches in the desired areas so as to isolate the channel and the necessary probes and pads. For the etching of the (Ga,Mn)As epilayer, a mixture of gases, SiCl_4 and Ar (1:1), which combines the effects of physical and chemical etching, is used. The RIE process needs to be optimized depending on the thickness of the (Ga,Mn)As epilayer. (Ga,Mn)As and GaAs etch at different rate, with (Ga,Mn)As susceptible mainly to physical etching only and hence etches away much more slowly than that of GaAs. This process has to be fine-tuned so that the trenches are not etched too deeply. Otherwise, it would be difficult to spin the next resist layer (if it is required to be a thin layer) on top of the chip due to its highly uneven surface created after etching. It must also be taken into account that the narrower trenches will be less etched than the wider ones due to the differences in the sizes of exposed areas.

Wet-etching involves immersing the sample in a bath of liquid-phase ('wet') etchant. The etchant used is a mixture of concentrated (72%) H_3PO_4 : H_2O : H_2O_2 in the proportion 1:40:10. The sample is etched for 10 s at 25°C to give an etched depth of 120-150 nm. The etch depth is specific in this case so that metallization of the back-gate can be made to the n-doped GaAs layer in the wafer. For best performance with the etchant, it is important to prepare a fresh mixture of it each time to ensure a consistent etching rate as H_2O_2 is highly reactive and the etchant mixture tends to degrade with time even if it is stored in a fridge. Wet-etching is usually employed in our case since the dimensions of the devices made are generally large, in the tens and hundreds of μm , which can be wet-etched relatively uniformly and quickly.

Metal deposition

Another way to transfer the pattern on the photo-resist to the sample is by metal deposition. This is usually done by thermal evaporation and is often the most challenging stage of the fabrication process since Au does not stick very well on (Ga,Mn)As. It is thus necessary to use a layer of thin Cr (typically 30 nm thick), which acts as an adhesive, to attach Au to the surface of the (Ga,Mn)As epilayer.

This is a critical step before bonding of the devices and much care has to be taken to ensure that the bond pads stick well in contact with the (Ga,Mn)As epilayer's surface. Firstly, both the Cr rod, and the Au wires in tungsten boats used in the evaporation process are degassed to remove any impurities in these two sources. Then, the evaporator used is pumped down to very low pressures before the start of evaporation (usually $5 - 6 \times 10^{-7}$ mbar) so as to minimize impurities in the evaporation chamber before evaporating. Thirdly, the Cr is deposited slowly at about 1 \AA/s to ensure that a uniform layer of Cr is formed. The time delay between evaporating Cr and Au is also made as short as possible (typically less than 2 minutes) so that the Cr layer deposited earlier is still hot and reactive, improving its adhesiveness to the Au layer deposited subsequently. For bond pads, a thick layer of Au is also deposited to ensure that the thin Au wires used in bonding stick better to the pads since less damage is done to the adhesive Cr layer by the ultrasound used during the wedge bonding. To improve the adhesiveness further, two chemical steps are carried out right before evaporation to ensure that the surface of the chip is clean before this fabrication step. The chip is first exposed to oxygen plasma for 30 s to remove any photo-resist or organic residuals. Then, it is dipped in a solution of HCl (37%) : deionized water (1:10) for 30 s to remove the top layer of native oxides, followed by a 30 s rinse in deionized water and blow-drying with nitrogen. These steps are important to ensure a clean surface for better adhesion but are difficult to apply for a thin GaMnAs epilayer since HCl also etches away the epilayer by removing the Mn oxides formed. Thus, the process of fabricating the device is designed such that only one evaporation step is required to form both the bond pads as well as the bottom-gate contact.

As soon as the evaporation step is done, the chip is fully immersed in acetone for the lift-off process: the unwanted metal layer on top of the remaining patterned UV-III resist will be removed as the UV-III dissolves. Once the procedure is successful, the sample is rinsed in IPA and blow-dried with nitrogen.

3.2.3 Packaging the device

After completing the fabrication steps, the chip is scribed in order to separate adjacent devices. This can be done using a scribe machine with a diamond tip. Typical device sizes are of the order of $2\text{ mm} \times 2\text{ mm}$, with the wafer thickness of about $400\ \mu\text{m}$. Individual devices are then mounted and wire bonded to a 20-pin chip carrier. Usually the devices are glued to the carrier with silver dag (a solution of fine silver powder in a MIBK solvent), cured at 80°C for 30 minutes. Because the gluing may affect the magnetic properties of the device under study by introducing unwanted strain, it is also possible to temporarily attach the chip with a UV-III resist, perform the bonding and then remove the resist with IPA. This results in a free-standing chip, held in place only by the bonding wires. The wire bonding was done with a wedge-wedge ultrasonic bonding machine, KS-4523, with either gold or aluminium wires of $25\ \mu\text{m}$ diameter.

3.2.4 Making the top-gate

In Chapter 6, the use of the top-gate with the ionic gel is introduced. Ionic gel is used because of its high capacity (refer to Chapter 2). In this section, the preparation of the ionic gel and the fabrication of the top-gate electrode is discussed.

Preparation of ionic gel

The ionic gel consists of an ionic liquid and a polymer matrix. The ionic liquid, 1-ethyl-3-methylimidazolium bis(trifluoromethylsulfonyl)imide ([EMIM][TFSI]) used was purchased from Sigma-Aldrich. It is a Fluka product with a purum grade and a purity of $\geq 97.0\%$ (NMR). The symmetric poly(styrene-block-ethylene oxide-block-styrene) (PS-PEO-PS) triblock copolymer used was purchased from Polymer Source, Inc. The molecular masses (M_n) of the PS and PEO blocks were 9.5 kg mol^{-1} and 48 kg mol^{-1} , respectively.

The ionic liquid [EMIM][TFSI] and the PS-PEO-PS triblock copolymer were dissolved in acetonitrile (or ethyl acetate) with the following proportions: 9.3 wt% ionic liquid, 0.7 wt% polymer, 90 wt% solvent. To ensure the mixture dissolved

fully, it is sealed in a vial and put on a hot-plate at 60°C for 2-3 hours in a glove box (under low pressure and low oxygen content). The mixture is then filtered using a 0.45 μm PTFE filter to get a clear solution. All materials used in this study were stored in a glove box before use.

Top-gate electrode

Due to the sensitive chemical nature of the ionic gel, it is difficult technically to perform additional chemical processes after introducing the ionic gel on the device. Patterning of the top-gate electrode via optical lithography is thus not a viable option. The sizes of the devices made also make thermal evaporation of the metallic top-gate with shadow mask difficult. Added to this issue is the underlying n-doped GaAs layer which acts as the back-gate of the device. Any attempt having the top-gate electrode on top of this layer will create a potential difference between the top-gate and the bottom-gate which will complicate the measurements as well as run the risk of shorting the two gates (since the top layers are quite thin) during the bonding process. These make the conventional process of spinning on the ionic gel and making a top-gate electrode impractical.

One way around this problem is to introduce a needle contact into a droplet of the ionic gel. The ‘needle’, which can be an end of a bonding wire, protrudes into the centre of the droplet and when charged, can polarize the charges in the ionic gel. However, this method proves to be difficult too due to the nature of the (Ga,Mn)As surface and the hydrophobic nature of [EMIM][TFSI]. The droplet of ionic gel wets the surface almost completely each time, making this method unfeasible.

To overcome the above issues, the top-gate electrode is made by two or three wires bonded across the centre of the chip. The wires are positioned as near to the top surface of the chip as possible without touching any of the devices. This is illustrated in Figure 3.3. Ionic liquid is then dropped into the chip carrier carefully to fill the whole carrier. The carrier is then sealed with a glass substrate to prevent the evaporation of the ionic gel.

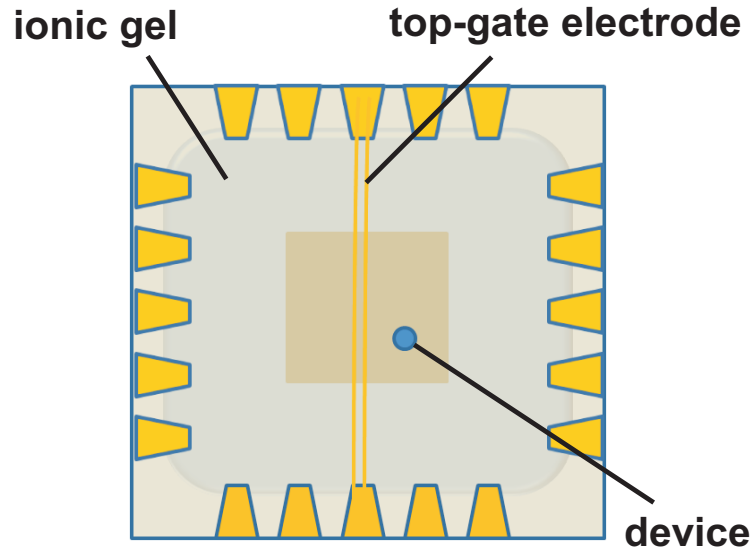


Figure 3.3: A schematic diagram of the chip-carrier illustrating the formation of the top-gate electrode. The two wires shown across the centre of the chip is the top-gate contact.

3.3 Measurement methods

In this section, the equipment and various electrical methods used for magnetotransport measurements at low temperatures are described.

3.3.1 Cryogenic systems

Low temperature magnetotransport measurements were performed in a Oxford Instruments Heliox cryostat. The system is a pumped He cryostat, equipped with a NbTi superconductive coil capable of magnetic fields of up to 12 T at 4.2 K. The base temperature of the system reaches 250 mK. This low temperature is achieved by first cooling the system to 2.2 K by pumping of He^4 , followed by the pumping of liquid He^3 below 2.2 K. The temperature of the system can be stabilized by the adjustment of a needle valve between the sample space and the liquid He reservoir, and a heating element controlled by a temperature controller Oxford Instruments ITC503. The system uses a vertical loading mechanism. Two variable temperature inserts were used, capable of rotating the sample with respect to the magnetic field. One uses an Attocube Systems ANC150 Piezo Step Controller which could rotate the

sample about two independent axes. It is coupled with two Hall sensors positioned in-plane and out-of-plane with respect to the sample allowing precise alignment of the sample to the external magnetic field. The other insert had a mechanical rotator and could only rotate the sample about one axis, either in plane or out-of-plane of the sample. It is also equipped with a temperature sensor which is positioned near the sample, giving a more accurate temperature reading at the device compared to measurements read directly off the temperature controller.

Another cryogenic system used is the custom-made 3-axial system by Cryogenics. It is equipped with a NbTi superconductive coil along the three principle axes of the sample space, capable of generating magnetic fields in all three directions (and since magnetic field is a vector, direction of the magnetic field experienced by the sample is generated by controlling the relative currents running through the three superconductive coils). The maximum magnetic field generated in each direction is usually limited to only ~ 1 T. As opposed to the Heliox system whereby a stable temperature of 4.2 K can be achieved by filling up the sample space with liquid He, the temperature in this 3-axial system is controlled by a constant flow of liquid He being pumped through the sample space together with a heating element controlled by a Lake Shore 340 temperature controller.

3.3.2 Electrical measurements

Electrical measurements made with the Heliox are usually done with an Agilent 4156C Precision Semiconductor Parameter Analyzer. It contain both SMUs (source measurement units) and VMUs (voltage monitor units). An additional pulse generator can also be attached to the parameter analyzer to generate short voltage pulses to the samples when needed. SMUs are capable of outputting a source voltage or current and measuring the current through it at the same time. VMUs are capable of making voltage measurements at specific contacts. The measurements made are then recorded either on disks or on a computer through a LabVIEW interface.

For measurements done using the 3-axial system, the samples were biased with an Agilent HP3245A Universal Source and gated with a Keithley 236 SMU, and measured with the lock-in technique, using either SR830, EG&G5210 or EG&G5302

lock-in amplifiers. When necessary, SR570 current preamplifiers were employed. The outputs of the lock-ins were read directly on a computer through a LabVIEW interface.

Resistance vs. temperature

Channel resistance is measured against temperature as a way to measure the Curie temperature, T_C , of the sample. The T_C of the device can be estimated from the singularity in the temperature derivative of the resistance [70]. For experiments done in both Chapters 5 and 6, the measurements were taken with the mechanical rotator in the Heliox. The mechanical rotator is chosen because the temperature sensor is positioned near the sample which will give a more accurate reading of the actual device temperature. Heliox is also an ideal system for this measurement as the sample space can be isolated during the measurement. The sample space can then be heated at a slow constant rate to get a higher resolution for measurement of T_C .

Measurements of the channel resistance of the device were taken from ~ 5 K to above the Curie temperature T_C at 60 K. A data point was taken each second while the sample space was being warmed up slowly with the internal heater at a fixed setting of 2.0, and with the needle valve connecting the sample space and the liquid helium bath fully closed. Different fixed gate voltages can be applied as the channel resistance is measured by measuring the change in the current flowing in the channel with a fixed applied voltage across the source-drain at 50 mV.

Magnetic field sweeps

Magnetic field sweeps were done for different sample orientations, both in-plane or out-of-plane of the sample. The in-plane and out-of-plane field sweeps confirm if the magnetization of the sample is out-of-plane or in-plane, and also determine the strength of the switching field. The difference of the magnetic field sweeps gives the anisotropic magnetoresistance (AMR) effect at saturation field (an example is in Chapter 5). In-plane magnetic field sweeps were also performed at different angles to the crystalline axis. This reveals the easy axes in the sample and when done with

different gate voltages, can demonstrate the effects of gating on its anisotropy (an example of this is in Chapter 5).

Field sweeps were done initially from different ranges to make sure that we did not miss any magnetization rotations and to determine the strength of the switchings. We could then zoom in to the relevant magnetic field ranges to study the details of the switchings with higher resolution.

Rotation experiments

The qualitative nature of the in-plane magnetic anisotropy landscape can be scanned in the Corbino device by recording the AMR at a rotating in-plane saturation field.

Details of the saturation field used and the frequency of the measurements are found in the individual experimental chapters. For experiments in Chapter 4, the Attocube rotator is used and the in-plane angles can be measured using the Hall sensors. For experiments in Chapters 5 and 6, the mechanical rotator is used. The rotation of the sample is measured by the number of rotations made with respect to the initial alignment with every 5 degrees corresponding to 2 and a half rotations. For all the experiments done, channel resistance was measured 101 times for each fixed back-gate voltage at each position. The average is then taken to obtain a mean value of the channel resistance for the different back-gate voltages at each point.

Voltage-pulse measurements

The experiments in Chapter 5 were carried out in the heliox. Using the pulse generator of the precision parameter analyzer, the experiments were performed at a constant field-sweep rate of 0.1 mT per second starting from a negative saturation field of 1 T. The gate voltage was set to a base value of -1 V and then after each measurement step spanning 1 s, a 10 ms voltage pulse of a fixed magnitude was applied and then returned to the base voltage.

The experiments in Chapter 6 were carried out using a Tektronix AFG 3102 dual channel arbitrary/function generator with the 3-axial system. A pulse with a pulse width of 5 ms is generated by the function generator with a leading and trailing time of 10 ns each. The measurement is taken for every 1 mT step, after a 500 ms wait

from the initiation of the pulse. Details of the magnetic field sweeps are recorded in Chapter 6. It is worth mentioning that there is no fundamental difference between the two methods except that there is less noise in the measurement of the controlled pulsing using the Tektronix function generator.

Chapter 4

Low-voltage back-gating and oxide removal

Only a few works so far have reported electrical gating, via charge depletion, of magnetic properties of (III,Mn)V ferromagnetic semiconductor field-effect transistors (FETs). Curie temperature and coercive field variations have been demonstrated by applying tens of volts on a top-gate FET with an oxide dielectric separating a metal gate from an (In,Mn)As or (Ga,Mn)As channel [1,3]. In this chapter, we introduce an all-semiconductor, epitaxial p-n junction field-effect transistor. As illustrated in Section 2.5.2, this allows for the possibility for a large depletion of (Ga,Mn)As thin films at a few volts with the presence of the depletion layer. Subsequently, we also apply the surface oxide etching procedure to controllably thin the (Ga,Mn)As layer in a fabricated transistor and observe a further strong enhancement of the field effect on the channel resistance. Mn_I was removed by post-growth annealing surface oxide strip. The systematic oxide stripping effectively thins the device and enhances the gating effects on the epilayer. Gatable spintronic characteristic of our p-n junction ferromagnetic FET is demonstrated in anisotropic magnetoresistance (AMR) measurements.

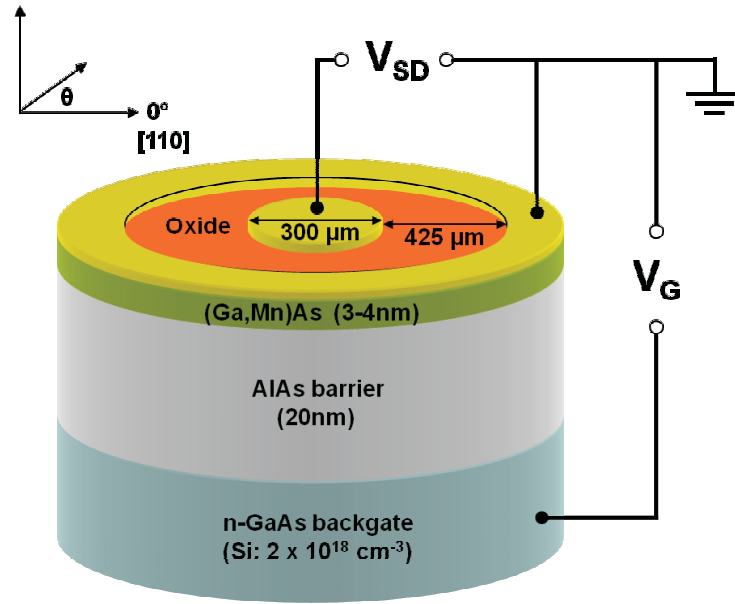


Figure 4.1: Schematic cross-section of the (Ga,Mn)As FET structure.

4.1 Sample structure

The devices made were fabricated using samples made by LT-MBE with a 4 nm thick epilayer of $\text{Ga}_{0.92}\text{Mn}_{0.08}\text{As}$ (wafer D036) grown on top of a 20 nm undoped AlAs barrier followed by a heavily n-doped epitaxial GaAs layer ($n = 2 \times 10^{18} \text{ cm}^{-3}$) which acts as the gate electrode. The undoped AlAs barrier was added as an insulating layer to minimize the out-diffusion of Mn ions during the wafer-growing process so as to limit the leakage current through the back-gate. Details of the fabrication method are outlined in Chapter 3.

The resistivity of the wafer used in this case is relatively high (device's resistance is $\sim 1.4 \text{ M}\Omega$ at 4.2 K giving a resistivity in the order of $\sim 1 \Omega\text{cm}$) as a result of the very thin layer of (Ga,Mn)As used. The majority of the data was recorded using the Corbino device, which minimizes the channel length to channel width ratio, lowering the device resistance and making electrical measurements feasible. The inner contact of the Corbino disc, of $300 \mu\text{m}$ in diameter, is the source and the outer ring, of $1150 \mu\text{m}$ in diameter, is the drain of the transistor structure. During the measurements, a source voltage, V_{SD} of 50 mV is applied through the source contact with the drain connected to a common ground. The gate voltage is applied through

a bond-pad in direct contact to the bottom heavily n-doped GaAs layer.

Using the equation 2.34 in Chapter 2 and by assuming abrupt depletion in the p-type region (with depletion length W_{Dp}) and in the n-type region on either side of the AlAs barrier, the respective dielectric constants $\epsilon_{GaAs} = 12.85$ and $\epsilon_{AlAs} = 10.06$ of GaAs and AlAs, and the GaAs band gap $\Delta_{GaAs} = 1.5$ eV [4]:

$$W_{Dp} = -\frac{\epsilon_{GaAs}}{\epsilon_{AlAs}} \left(\frac{n}{n+p} \right) W_{AlAs} + \left[\left(\frac{\epsilon_{GaAs}}{\epsilon_{AlAs}} \frac{n}{n+p} W_{AlAs} \right)^2 + 2\epsilon_{GaAs} \left(\frac{n}{p(p+n)} \right) (\Delta_{GaAs} + V_g) \right]^{\frac{1}{2}} \quad (4.1)$$

where n is the doping concentration of the n-region, p is the hole concentration in the p-region, W_{AlAs} is the AlAs barrier width, Δ_{GaAs} is the GaAs band gap and V_g is the applied gate voltage. Using the equation for the 4-nm-thick (Ga,Mn)As, one obtains 18% depletion at 3 V and 34% depletion at 10 V.

4.2 Characterization of the FET

4.2.1 Leakage current

The Corbino device is first verified to have inconsequential leakage current as shown in Figure 4.2 for both 4 K and 40 K. With $V_{SD} = 0$ V, it is shown that the leakage current (I_g) passes directly to the drain so that it does not significantly affect the measurements from the source current for both temperatures. The schematic diagram (inset of Figure 4.2) gives a simplistic outlook of the currents flowing through the device. It can be verified from the graphs (together with Figure 4.3) that the magnitude of the current measured through the source contact (I_s) is equal to the addition of the current through the drain contact (I_d) and the gate contact (I_g) (which is treated as the leakage current here since ideally $I_g = 0$ A).

Simulating the actual measurement setting with a $V_{SD} = 50$ mV, the different currents through the device (similar to Figure 4.2) are plotted in Figure 4.3 for 25 K. The leakage current is negligible within the range of $V_g = -2$ V to $+2$ V. At higher positive gate voltage ($+3$ V), the leakage current becomes significant. However, it can be seen in the plot that the gradient of the slope on the channel current (I_s) remains approximately constant, and the leakage current is mainly through the

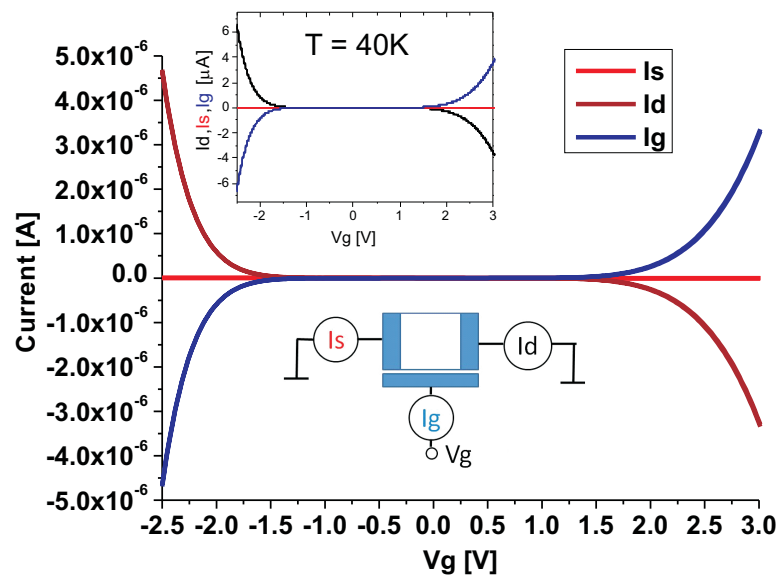


Figure 4.2: IV characteristics of Corbino device for different gate voltages for $V_{SD} = 0$ V at two different temperatures (4 K and 40 K(inset)). The schematic diagram (inset) gives a simplistic outlook of the currents flowing through the device.

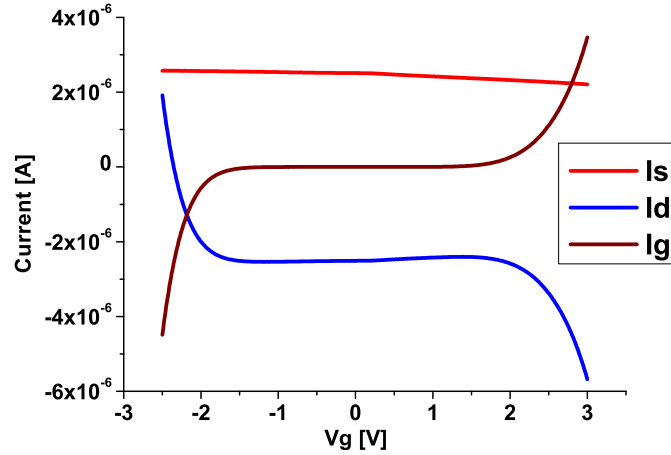


Figure 4.3: IV characteristics of Corbino device for different gate voltages (at 25 K) for $V_{SD} = 50 \text{ mV}$. It can be seen in the plot that the gradient of the slope on the channel current (I_s) remains approximately constant, and the leakage current is mainly through the drain contact.

drain contact. This further confirms that the leakage current flows mainly through the drain contact (V_d is fixed at 0 V) and has little to play in the measurements of the device itself.

4.2.2 Magnetic characteristics

For compressively strained (Ga,Mn)As epilayer, the magnetization of the device is expected to lie in plane. This is demonstrated in Figure 4.4 which plots the relative resistance normalized to the zero-field value of the resistance. For the perpendicular magnetic field sweep, two humps are observed as the magnetic field is swept from -1 T to +1 T. Each hump identifies a magnetization switching process. The magnetization of the (Ga,Mn)As film was first aligned to the negative perpendicular field direction by a saturation magnetic field of -1 T. The large negative isotropic magnetoresistance (IMR) is associated with a field-induced reduction in the spin disorder responsible for much of the resistance near the Curie temperature (T_C) [45] (cf. Section 2.4.1 in Chapter 2). This negative IMR is reduced as the strength of the aligning magnetic field is decreased.

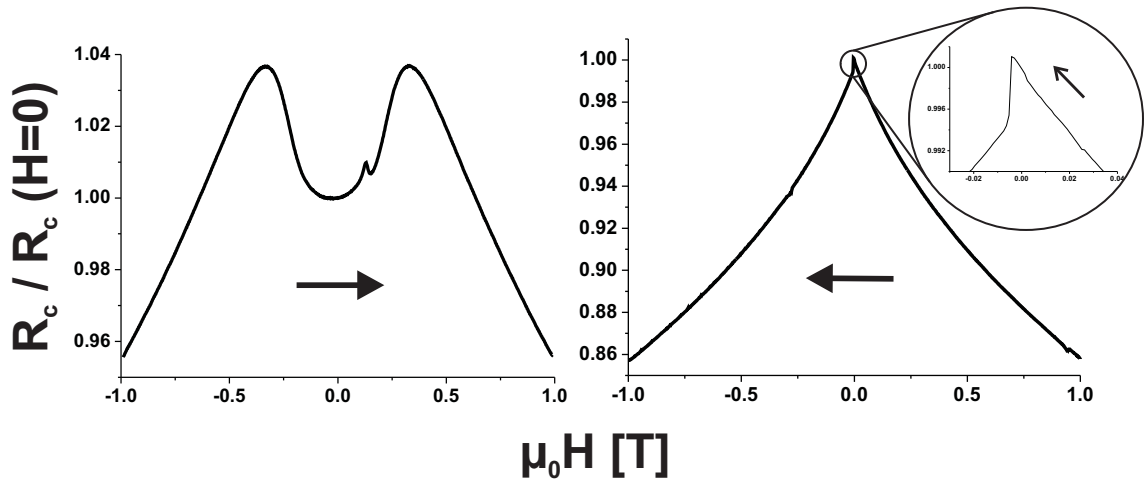


Figure 4.4: Magnetic field sweeps perpendicular (left) and parallel (right) to the plane of the device at 15 K at $V_g = 0$ V. The arrows give the direction of the magnetic field sweeps.

As the magnitude of the negative magnetic field decreases (i.e. becomes more positive), the relative magnetoresistance increases to a maximum at around -330 mT. At this critical switching field, the magnetization of the epilayer relaxes back to the plane of the epilayer (the lowest energy configuration for this material). The resistance then decreases as the magnitude of the magnetic field is lowered as the magnetic moments are relaxed back to their in-plane configuration [57]. The same happens as the magnetic field is increased to +1 T. The in-plane magnetization configuration is being ‘tilted’ out and aligned to the positive perpendicular direction at the critical field of +330 mT. The negative magnetoresistance again took over and lowered the relative resistance further as the magnetic moments further aligned and resistance associated with spin-disorder is minimized. Notice that there is a small peak at about 130 mT. This is associated with a slight mis-alignment of the device with the sample rod so that it is tilted slightly out of plane, and corresponds to a shift to a partly aligned in-plane magnetization at this field strength.

An in-plane magnetic field sweep from a saturation field of +1 T to -1 T is also performed at 15 K along the [110] crystalline axis (easy axis) of the sample as shown in Figure 4.4. This confirms that the magnetization of the sample lies in-plane. Zooming into the centre of the plot, a peak is observed at around 4 mT

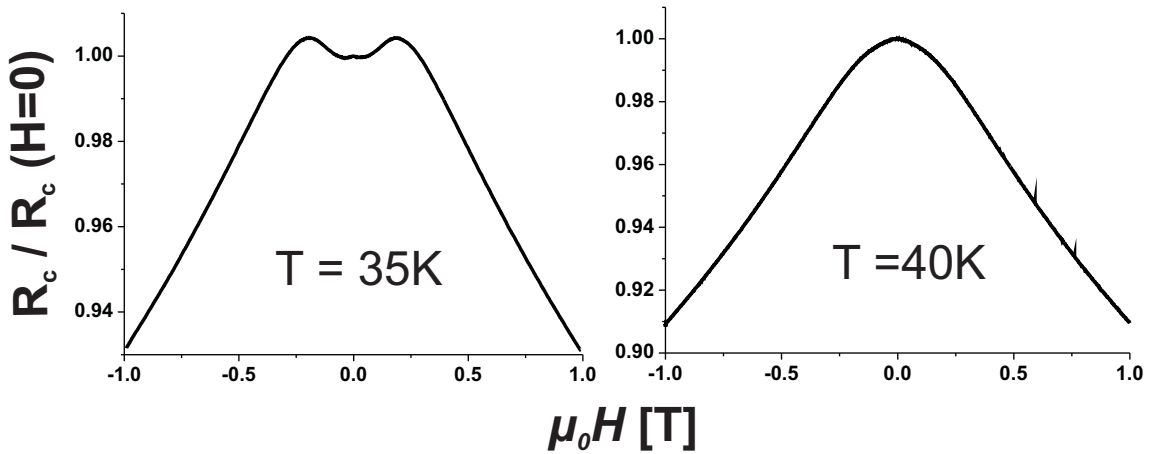


Figure 4.5: Perpendicular field sweeps for two other temperatures - 35 K (left panel) and 40 K (right panel). Together with the perpendicular field sweeps for 15 K, an approximate range for T_C can be deduced.

which is within the precision of the magnetic field measurement. The slow increase of relative resistance to the peak from the positive magnetic field is likely due to a very small rotation of the magnetization to the ‘natural’ magnetic orientation. The sharp decrease which follows after the peak arises from a 180° reversal as the magnetization is being flipped from the positive magnetic field direction to the negative one. The magnetoresistance then follows the decreasing trend again, which arises from the reduction in the spin disorder with stronger alignment to the direction of the negative magnetic field as its magnitude increases.

In-plane magnetic field sweeps at different angles with respect to the crystalline axes are important for samples with in-plane magnetization as they elucidate the magnetization properties of these materials. This will be further discussed in Chapter 5 as these measurements reveal the easy magnetic axes as well as the crystalline magnetic anisotropy in (Ga,Mn)As.

The perpendicular-to-plane magnetic field sweeps at different temperatures are shown in Figure 4.5. The relative resistance (normalized to the resistance at zero magnetic field) shows two distinct AMR peaks with a magnitude of $\sim 3.5\%$ at about ± 330 mT for 15 K. As the temperature increases, the twin peaks decrease in both the magnitude of the AMR and the switching field. At 35 K, the AMR peaks

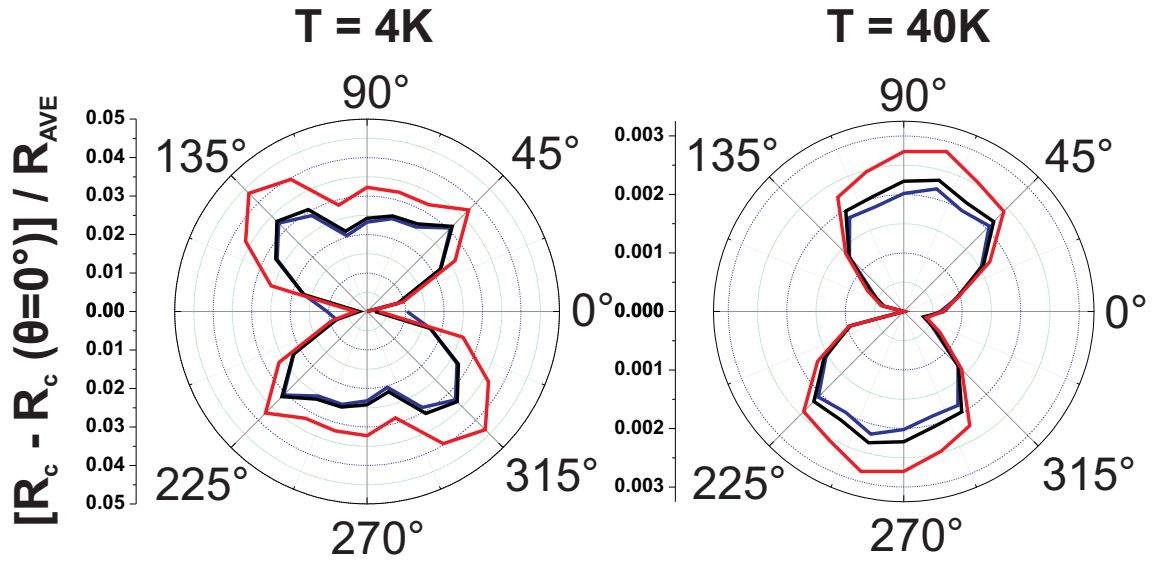


Figure 4.6: Relative anisotropic magnetoresistance (AMR) for in-plane magnetic field (5 T) at different angles with respect to the crystalline axis [110] ($\theta = 0^\circ$) at 4 K and 40 K for gate voltages at -2.5 (blue), 0 (black) and +3.0 V (red). R_{AVE} is the average channel resistance measured across the entire angular range for the respective gate voltages.

decrease to a magnitude of $\sim 0.04\%$ with a switching field at about ± 190 mT. As the temperature at which the measurement sweeps are made increases from 35 K to 40 K, the plot changes from a twin-peaks to a single peak at 0 T. The reduction in the switching field strength and the eventual disappearance of the twin peaks can be explained by the decrease of magnetic anisotropy due to the weakening of the ferromagnetic ordering when the temperature approaches T_C . From the plot, it is expected that the Curie temperature lies close to 40 K.

4.3 Temperature and voltage dependence of AMR

4.3.1 In-plane magnetic field rotation

The qualitative nature of the in-plane magnetic anisotropy landscape, which determines the switching processes, can be scanned in our Corbino device by recording the AMR in a rotating in-plane saturation field. Unlike the out-of-plane rotation

AMR, contributions depending on the relative angle between the in-plane magnetization and current average out over the radial current lines. The in-plane AMR then depends purely on the angle between magnetization and crystallographic axes. The rough in-plane magnetic field rotation measurements, shown in Figure 4.6, are taken every 15 degrees in a saturation field of magnitude 5 T, where the relative AMR is calculated from the difference between magnetoresistance at different in-plane angles and that of zero degree (along the $[110]$ crystalline axis), divided by the average magnetoresistance for the entire rotation AMR. These plots are recorded at two different temperature to explore the temperature dependent gating effects on the AMR.

Temperature and voltage dependence

The manifestation of the uniaxial anisotropy and the cubic anisotropy of the AMR in the in-plane saturation magnetic field rotation measurements can be observed as maximum relative change in AMR in the $[1\bar{1}0]$ crystalline axis (i.e. $\theta = 90^\circ$) and the symmetry breaking directions between the $[110]$ and $[1\bar{1}0]$ crystalline axes respectively. At 4 K, the AMR plot unveils an uniaxial symmetry and traces of an additional cubic term breaking the symmetry between the $[110]$ and $[1\bar{1}0]$ crystalline directions. The magnitude of this in-plane rotation AMR is $\sim 3\%$ along the axis between the $[110]$ and $[1\bar{1}0]$ crystalline directions for zero gate voltage. As the temperature increases to 40 K, the uniaxial component of the in-plane AMR dominates as expected [48] with a magnitude of about 0.23% at $\sim 75^\circ$ from the $[110]$ crystal axis. The decrease in the magnitude of the in-plane rotation AMR can be associated with the de-stabilization of the magnetic state of the sample at higher temperatures.

Besides temperature dependence effects, the in-plane rotation AMR is also affected by the change in the hole density in the epilayer by the application of different gate voltages in the field effect transistor structure. As shown in Figure 4.6, the magnitude of the AMR increases with increasing positive gate voltages (depletion of holes). There is also an asymmetry observed in the magnitude of the gating effects on the AMR for the different polarity of applied gate voltages, which is also

observed in other experiments in the Hall resistance [3] and Curie temperature [75]. The effects on the magnitudes of the in-plane rotation AMR is not isotropic; instead it is concentrated on the uniaxial component close to or along the $[1\bar{1}0]$ crystalline direction.

4.3.2 Perpendicular-to-plane magnetic field rotation

Besides in-plane rotation AMR measurements done at saturation field of 5 T, perpendicular to plane rotation AMR measurements are also done with a saturation field of 10 T. The sample is first placed in plane with the magnetic field along the $[110]$ crystalline axis (i.e. 0°). It is then rotated in the saturation magnetic field out-of-plane and the channel resistance is recorded for every 15 degrees. The results for the out-of-plane rotation AMR for different temperatures and different gate voltages are plotted in Figure 4.7. It is noted that anomalous Hall effect is embedded in these magnetoresistance measurements and is also dependent on the rotation angle out-of-plane. Unfortunately, this effect cannot be easily extracted for the Corbino device measured.

As shown in Figure 4.7, the relative perpendicular-to-plane rotation AMR, which is calculated by dividing the channel resistance measured at different angles by the in-plane (zero degree) resistance, increases with increasing angle from the sample plane. This is consistent with what is expected of $(\text{Ga,Mn})\text{As}$ as the sample resistance is higher when its magnetization is perpendicular to the measuring current than when the two are parallel [57] (also explained in Section 2.4.2 in Chapter 2), especially when zero degree in plane is along $[110]$ crystalline axis which is an easy axis of the sample.

From the magnitude of the relative AMR of the 4 K plot, a cosine squared dependence is observed from 0° (in-plane) to 90° (out-of-plane). The anomaly observed for high positive gate voltages at 4 K, which is not seen at higher temperatures, could be due to larger leakage currents at these gate voltages for a more resistive system at low temperature. As the temperature increases, the magnitude of the AMR, together with the overall gating effect, is suppressed. The out-of-plane AMR decreases from $\sim 6\%$ at 4 K to $\sim 3\%$ at 37 K for zero gate voltages, again consistent

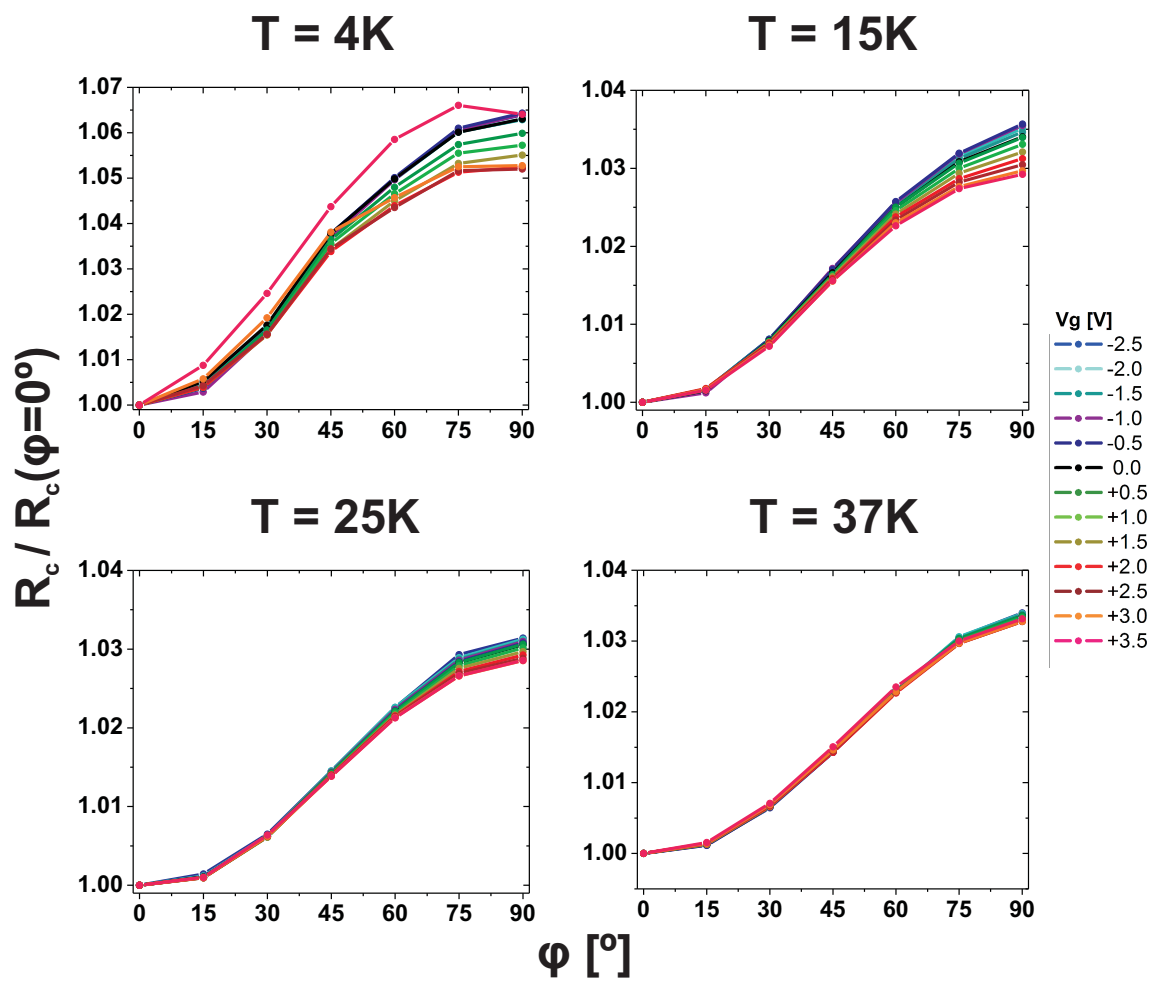


Figure 4.7: Relative anisotropic magnetoresistance (AMR) measured at saturation (10 T) in a rotating out-of-plane field for different gate voltages at 4 K, 15 K, 25 K and 37 K.

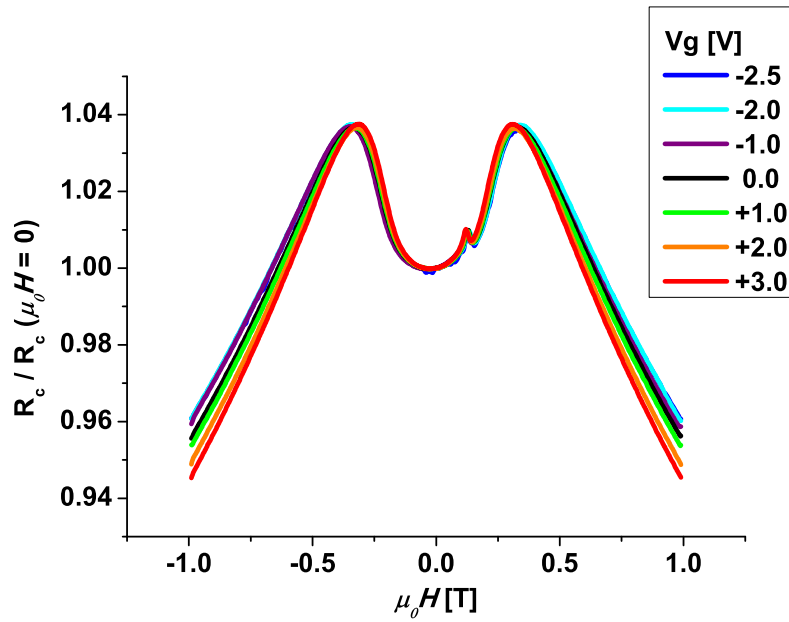


Figure 4.8: Perpendicular magnetic field sweeps at 15 K for different gate voltages.

with added spin fluctuations due to temperature's contribution to its entropy. At 4 K, application of a gate voltage of -2.5 V yields an increase of about 0.1% whereas an application of +2.5 V yields a decrease of about 1%. The asymmetric behaviour is consistent with what is seen in other effects. For the positive gate voltages, the effect of gating also seems linear with increasing positive gate voltages from 0 V to +2.5 V. At higher temperatures, the effects of gating is diminished. For 37 K, application of a gate voltage of -2.5 V yields an increase of only about 0.05% whereas an application of +2.5 V yields a decrease of about 0.08%.

4.3.3 In-plane and out-of-plane magnetic field sweeps

Figure 4.8 shows the out-of-plane magnetic field sweeps at 15 K from -1 T to +1 T for various V_g values. As described in previous section, the negative isotropic magnetoresistance (IMR) is associated with the stronger alignment of spins which suppresses spin disorder. The small notch in between the twin peaks is due to a slight misalignment of the sample which was later checked to be less than 10° . Application of positive gate voltages shift the switching field to a lower magnitude and the

converse is true for negative gate voltages. With an application of a gate voltage of +3.0 V, the magnitude of the switching field decreases from 326 mT at zero V_g to 306 mT. For a V_g of -2.5 V, the magnitude of the switching field increases to 340 mT. Besides changing the switching fields, the slopes of the negative IMR also decreases in magnitude with positive gate voltages. A possible explanation could be as follow. Depletion of holes with positive gate voltages would de-stabilize the coupling between Mn magnetic moments in the hole-mediated ferromagnetic system. Thus, the Mn moments would be less aligned for the case of positive gate voltages than that of the negative gate voltages (which increases the hole concentration in the system). In the case of the negative magnetoresistance, which is related to the magnetization in (Ga,Mn)As, increasing the applied field say from 0.5 T to +1.0 T would align the Mn moments more for the case of positive gate voltages than that of the negative voltages. This could result in a larger percentage change in the negative IMR for the positive gate voltages than the negative gate voltages for a given change in the applied magnetic field strength. Another point that can be made about Figure 4.8 is that the magnitude of peak in the relative change in the magnetoresistance does not seem to alter with the application of gate voltages. This could be related to the negative IMR since the relative magneoresistance measured include both the positive AMR as well as the negative IMR terms. A possible larger change in the AMR component for positive gate voltages (similar to Figure 4.9) could be masked by the stronger negative change in the IMR components for these positive gate voltages.

In-plane magnetic field sweeps at 4 K along the [110] from -1 T to +1 T are shown in Figure 4.9 for different gate voltages. Similar to the out-of-plane magnetic field sweeps, a depletion of the epilayer with positive gate voltage of +3.0 V decreases the magnitude of the switching field from ~ 380 mT at 0 V to ~ 370 mT. On the other hand, the magnitude of the AMR increases with the application of +3.0 V from 3.8% at 0 V to 5.5%. Again, the slopes of the negative magnetoresistance also decrease in magnitude with positive gate voltages.

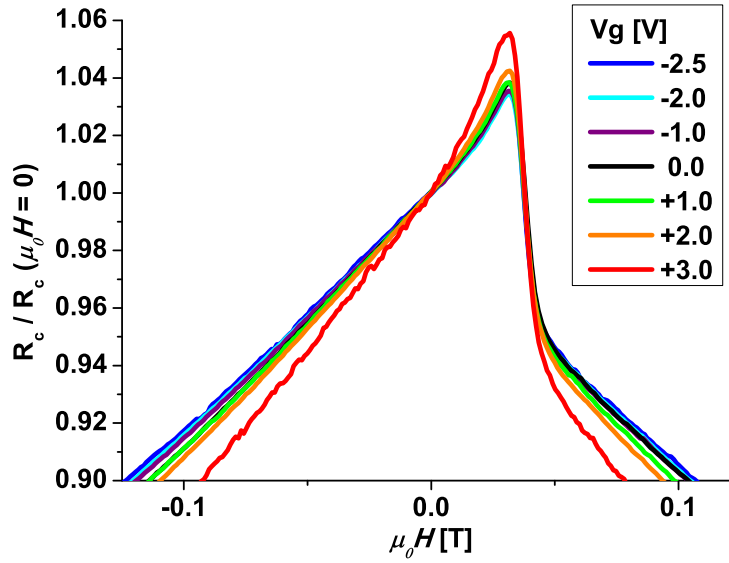


Figure 4.9: In-plane field sweeps at 4 K for different gate voltages along the [110].

4.4 Surface oxide etching

Aside from the standard continuous annealing, a sequence of discrete etch-anneal steps has been applied, each consisting of 30 s etching in 30% HCl, rinsing in water, and subsequent annealing for 5 min. (The HCl etched surface is hydrophobic and dries off instantly after the rinsing.)

This is of special interest since manganese impurities residing in the interstitial sites (Mn_I) of Mn-doped (Ga,Mn)As act as double donors and couple anti-ferromagnetically with the local substitutional Mn moments, decreasing the strength of ferromagnetism in (Ga,Mn)As. Discrete annealing and oxide removal steps aid in removing these Mn_I systematically.

4.4.1 Channel Resistances

Figures 4.10 and 4.11 show two gating characteristics of the resistance of one physical device which was fabricated as illustrated earlier in the chapter. After measuring this device, the (Ga,Mn)As layer was further etched to approximately 3 nm without removing the contacts and again measured. In both cases we find a marked decrease

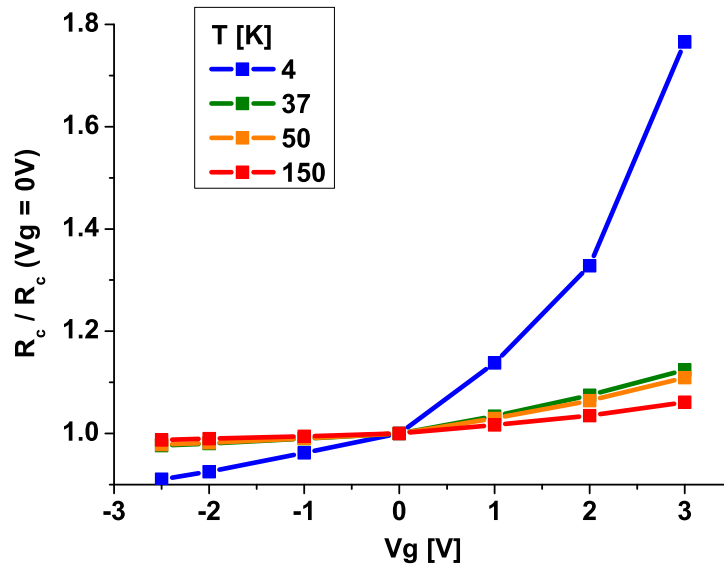


Figure 4.10: Channel resistance at different temperatures with different applied gate voltages

in the (Ga,Mn)As channel conductance upon depletion induced by gating. The gating efficiency is enhanced in the thinned sample, consistent with the increased relative depletion at a given voltage. Note that the large amplification of the field-effect with decreasing temperature we observed is attributed to the vicinity of the metal-insulator transition in the studied (Ga,Mn)As.

4.5 Summary and Conclusions

These sets of experiments provided insights into the general device characteristics and magnetic properties of ultra-thin (Ga,Mn)As with an in-built n-type back-gate. The magnetization vector of the device is observed to lie in-plane and the effects of gating on AMR are observed. The Curie temperature of the device has been estimated through its AMR measured by out-of-plane magnetic field sweeps. A more systematic way of measuring the Curie temperature (cf. Section 2.6 in Chapter 2) is demonstrated in the next chapter (since the measurements done on this device happened before the publication [70]). Systematic etching by oxide removal allows

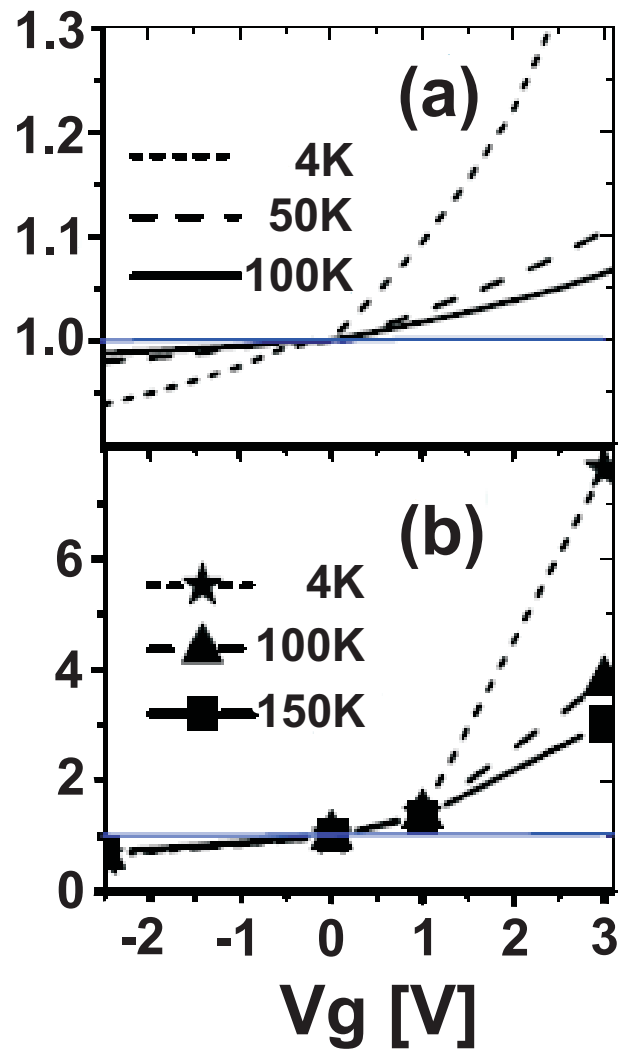


Figure 4.11: Gate voltage dependence of the source-drain resistivity relative to the resistivity at zero gate voltage for the FET device with 4-nm-thick (Ga,Mn)As (plus a 1 nm oxidized surface layer) measured at different temperatures. (b) Same as (a) after thinning the (Ga,Mn)As layer to 3 nm by etching. Done in collaboration with Dr. Olejník.

for effective thinning of the sample and thus allows more effective gating. In the next chapter, a more detailed study on an improved wafer is made. Especially of interest is the effect of gating on the magnetic anisotropy of the (Ga,Mn)As epilayer.

Chapter 5

Persistent switching by voltage pulses

Having developed an all-semiconductor, epitaxial p-n junction field-effect transistor in the previous chapter, the system was exploited for more detailed investigation of electrical manipulation on the magnetic properties of the (Ga,Mn)As epilayer through gating. The wafer was altered slightly to contain a lower concentration of Mn dopants, resulting in a lower concentration of holes and allowing for a larger effect with the electrical gating. Short voltage pulses were also used in place of fixed constant gate voltages to demonstrate magnetic response and the persistence of induced reorientations of the magnetization vector to short electric pulses. It also removes potentially obscuring variations among the resistance traces in regions away from magnetization switchings which are caused by different slopes of the negative IMR and AMR at different gate voltages.

5.1 Device Structure and Simulations

The schematic cross-section of the III-V heterostructure used in this sets of experiment is shown in Figure 5.1. It is a semiconductor p-n junction FET specially designed to accommodate ferromagnetism in the p-type region and its efficient depletion by low voltages. From the top, the structure comprises a 5 nm thick approximately 2.5% Mn-doped GaAs (wafer E028) capped by 2 nm of undoped GaAs to pre-

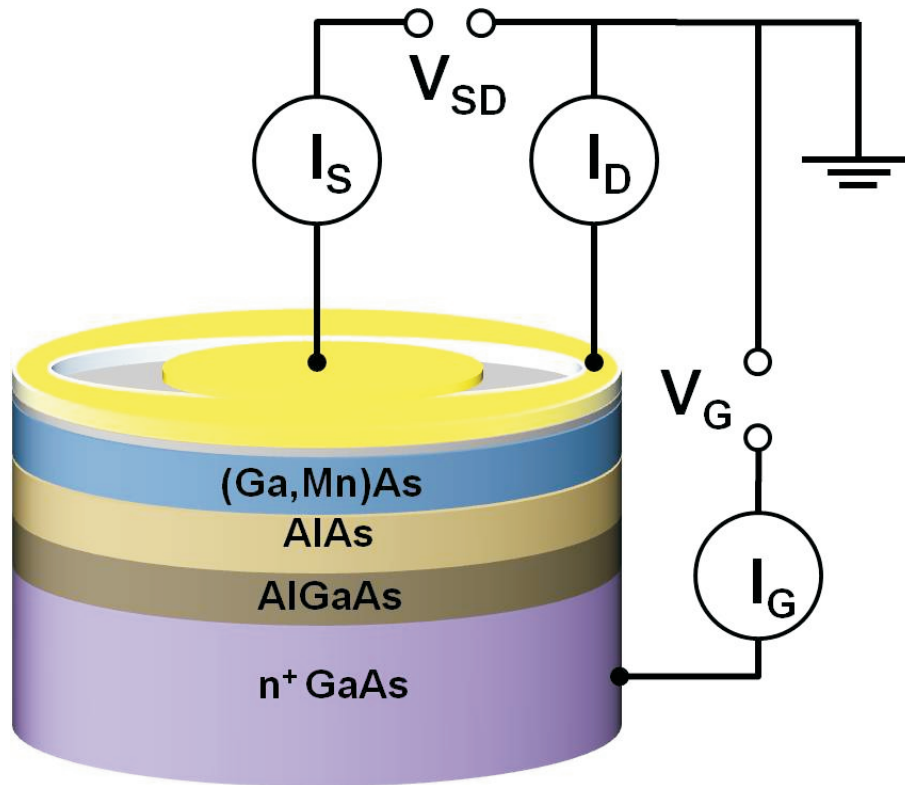


Figure 5.1: Schematic of the ferromagnetic p-n junction FET structure and the Corbino disk geometry of the source and drain contacts.

vent oxidation of the underlying transition metal doped semiconductor film. These two top layers were grown by low-temperature molecular-beam-epitaxy (MBE) to avoid Mn precipitation. The 2.5% doping was chosen to pass the insulator-to-metal transition threshold which for the moderately deep Mn_{Ga} acceptor is between 1-2% and to achieve robust ferromagnetic state with Curie temperature $T_C \approx 30$ K, while still minimizing the number of unintentional interstitial-Mn impurities [20, 76, 77]. (The interstitial Mn is highly mobile at the growth temperature and its diffusion into the p-n junction would result in detrimental leakage currents.) The Curie temperature measured by SQUID in an unpatterned piece of the wafer is comparable to maximum T_C 's achieved at the same Mn-doping in thicker films, indicating a very good quality of the ultra-thin ferromagnetic semiconductor epilayer.

The n-type gate electrode is formed by a highly Si-doped ($2 \times 10^{18} \text{ cm}^{-3}$) GaAs grown by high-temperature MBE. The large electron doping is required in order to achieve appreciable and voltage dependent depletion of the ferromagnetic p-region

with hole doping $\sim 10^{20} \text{ cm}^{-3}$. The built-in electrostatic barrier due to the depletion effect at the p-n junction is further supported by inserting a 10 nm $\text{Al}_{0.3}\text{Ga}_{0.7}\text{As}$ spacer layer with a large conduction band off-set to the neighboring n-GaAs and a 10 nm AlAs spacer with a large valence band off-set to the neighboring p-(Ga,Mn)As.

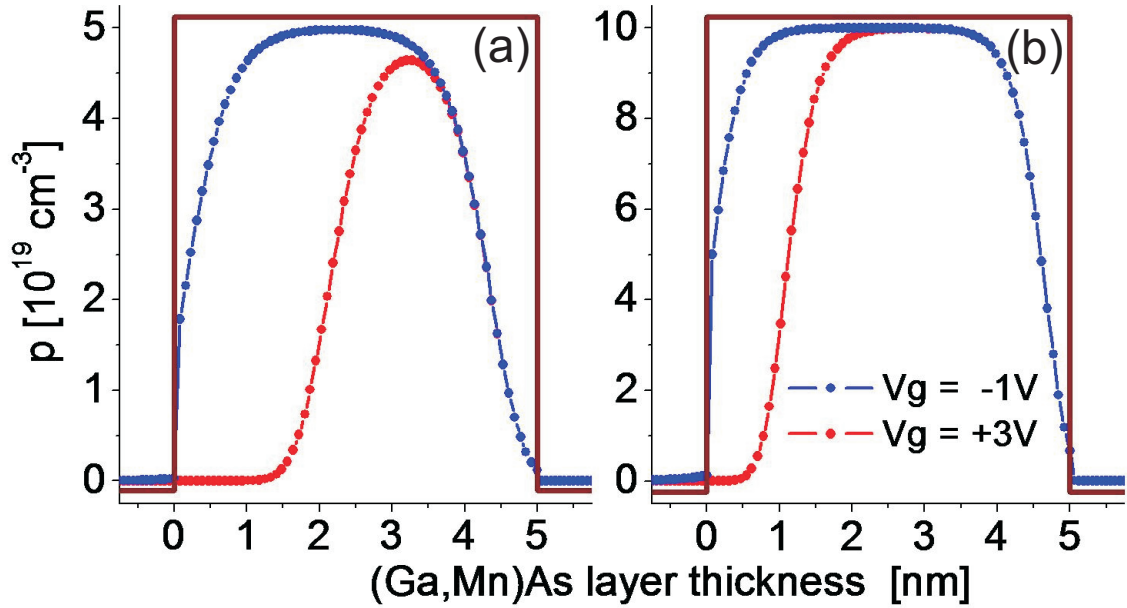


Figure 5.2: (a) and (b) Numerical simulations of the hole density profile at -1 V (accumulation) and +3 V (depletion), considering a $2 \times 10^{18} \text{ cm}^{-3}$ electron doping in the n-GaAs and $5 \times 10^{19} \text{ cm}^{-3}$ and 10^{20} cm^{-3} hole doping in the p-(Ga,Mn)As. The simulations were done by Dr. Ogawa.

Self-consistent numerical simulations using the Silvaco-Atlas device modeling package done by Dr. Ogawa from the Hitachi Cambridge Laboratory are shown in Figure 5.2. Two simulations (Figure 5.2(a) and (b)) with slightly different carrier concentrations were done for $5 \times 10^{19} \text{ cm}^{-3}$ and 10^{20} cm^{-3} hole doping as would be expected for (Ga,Mn)As with a nominal Mn doping of 2.5% and a T_C of $\sim 30 \text{ K}$ [8]. They confirm that sizable variation of carrier distribution can be achieved by gating the heterostructure with less than 4 V. The ‘0 nm’ on the x-axis of these diagrams is defined as the distance from the interface between the (Ga,Mn)As epilayer and the neighbouring AlAs barrier with ‘5 nm’ being the edge of the ‘free’ surface (or

neighbouring the insulating GaAs protective layer with a 5 nm gold contact set to ground). The built-in potential due to the band bending at the p-n junction results in a depletion layer even at negative gate bias. The calculations also illustrate that total hole depletion/accumulation in the (Ga,Mn)As contains both the change in the average 3D hole density in the epilayer and the change in the effective thickness of the conductive ferromagnetic semiconductor film. As expected of the p-n junction gating, the change of the holes density is mainly within the vicinity of the (Ga,Mn)As/AlAs barrier interface. The hole density within 2 nm from the ‘free’ surface is unchanged regardless of the back-gate voltage applied. The Drude channel conductance is linearly proportional to both of these components and is therefore expected to be linearly proportional to the total depletion/accumulation.

Gate voltage sweep measurements done at 4.2 K are shown in Figure 5.3. The plot shows negligible leakage current through the back-gate (I_g) from a gate voltage of -1 V to +2.5 V. At higher positive gate voltage (+3 V), the leakage current becomes significant. However, it can be seen that the gradient of the slope on the channel current (I_s) remains approximately constant, and the leakage current is mainly through the drain contact. Measurements discussed below were done at voltages between -1 V (forward bias) to +3 V (reverse bias) for which the leakage currents between the n-GaAs gate and p-(Ga,Mn)As channel can be neglected as shown. The (Ga,Mn)As channel was lithographically patterned in a low-resistance Corbino disk geometry with the inner contact diameter of 500 μm and the outer diameter of 600 μm .

5.2 Voltage Control of Curie temperature and magnetoresistance

In Figure 5.4, the measured channel resistances versus gate-voltage were plotted for temperature 4-40 K. At 40 K, an increase of the channel resistance by approximately 25% is observed at positive voltages. It is consistent with the depletion of the (Ga,Mn)As channel as predicted by the simulations in Figure 5.2 using the Drude conductance model. At low temperatures, the gating effect is strongly enhanced.

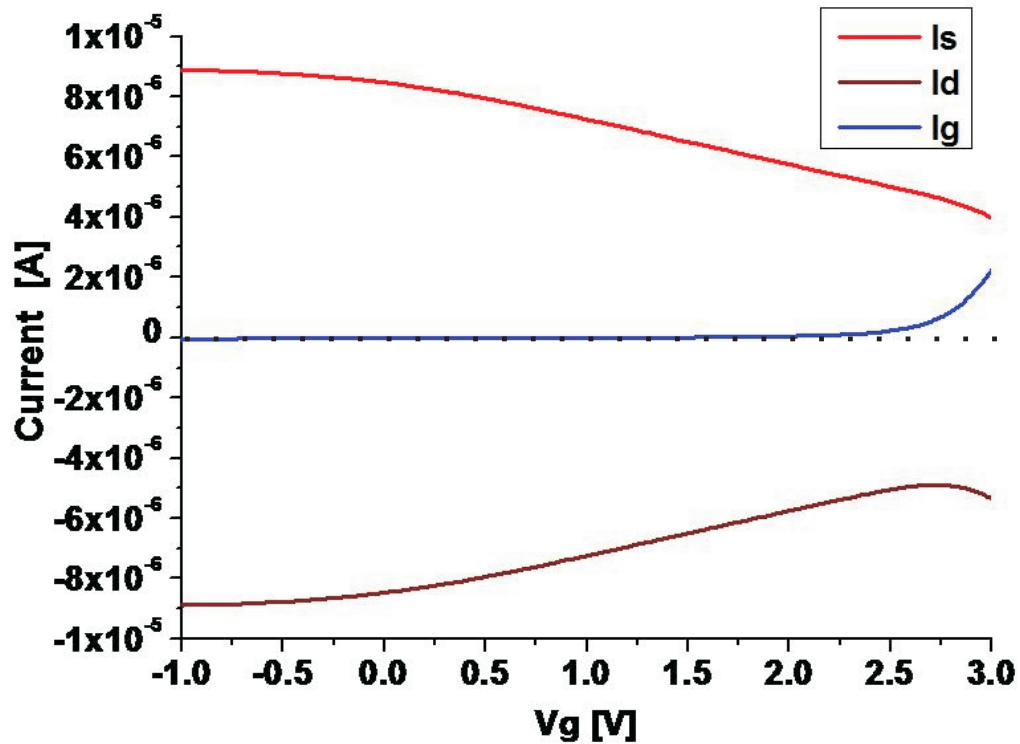


Figure 5.3: Gate voltage sweep measurements done at 4.2 K. The plot shows negligible leakage current through the back-gate (I_g) from a gate voltage of -1 V to +2.5 V. At higher positive gate voltage (+3 V), the leakage current became significant. However, it can be seen that the gradient of the slope on the channel current (I_s) remains approximately constant, and the leakage current is mainly through the drain contact.

At 4 K the increase of R_c between -1 and +3 V is by more than 100%. This enhancement is attributed to the vicinity of the metal-insulator transition in our ultra-thin (Ga,Mn)As epilayer.

The voltage-dependence of the Curie temperature in the ferromagnetic p-n junction is shown in Figure 5.5. Our measurement technique is distinct from previous studies which relied on approximate extrapolation schemes based on Arrott plot measurements at finite magnetic fields [1, 3, 78]. Recent observation and interpretation of the peak [70] in the zero-field temperature derivative of the resistance at the Curie point in good quality (Ga,Mn)As materials has provided the tool for direct

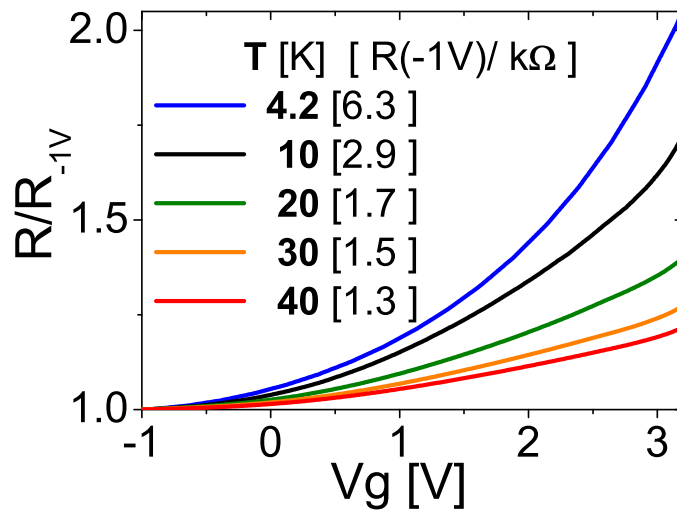


Figure 5.4: Gate voltage dependence of the p-(Ga,Mn)As channel resistance at temperatures 4-40 K.

transport measurements of T_C in microdevices without relying on any extrapolation schemes (cf. Section 2.6 in Chapter 2). This has also overcome the difficulty of measuring the T_C in SQUID for low-doped (Ga,Mn)As microdevices directly since they are often too small to generate enough magnetization required for the SQUID's sensitivity.

Differentiated resistivity curves obtained in the device at 0 and +3 V are plotted in Figure 5.5. The data show a clear shift of the Curie temperature. For V_g at 0 V, a peak (ie. the Curie point) is observed at ~ 27.9 K, which is consistent with what is measured for the wafer using SQUID. For V_g at +3 V, the Curie point is shifted to ~ 26.9 K; i.e., the magnetization can be turned on and off in parallel with accumulating and depleting holes in the ferromagnetic semiconductor channel by biasing the p-n junctions with a few volts.

Curie temperature variations provide the key physical demonstration of the low-voltage control of magnetization. Nevertheless, for most spintronic functionalities it is not required to destroy the ordered state of spins but only to change their collective orientation. Focus is therefore placed on effects related to reorientations of the unit vector of the macroscopic moment in the rest of the chapter. To avoid thermal fluctuations of the magnetization, all measurements are done far from the

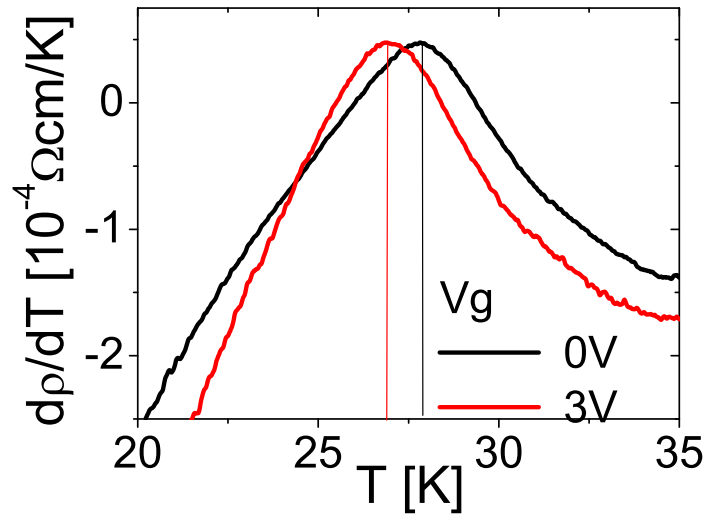


Figure 5.5: Temperature derivative of the measured channel resistivity at 0 and +3 V. The maximum corresponds to T_c .

Curie point at 4.2 K.

In Figure 5.6, magnetoresistance traces recorded during in-plane and perpendicular-to-plane sweeps of an external magnetic field are shown, at gate voltages -1 and +3 V. Apart from the negative isotropic magnetoresistance (IMR), the data indicate a remarkably large anisotropic magnetoresistance (AMR) effect which at saturation reaches $\sim 30\%$. The characteristics of IMR and AMR have been discussed in much detail in chapter 4. As in the previous chapter, even with a much lower Mn-doped (Ga,Mn)As epilayer, the resistance is larger for the perpendicular-to-plane magnetization orientation and the size of the effect is enhanced by depletion. The magnetoresistance traces in Figure 5.6 indicate that the film has a magnetic anisotropy favoring in-plane magnetization, which is overcome by an external field of approximately 150 mT. At weaker magnetic fields, magnetization switching effects are confined to the plane of the ferromagnetic film. The electrical response of our system to magnetization rotations is both large and tunable by low gate voltages.

The measurements, shown in Figure 5.7, unveil a cubic anisotropy along the $[110]/[1\bar{1}0]$ crystal axes and an additional uniaxial term breaking the symmetry between the $[110]$ and $[1\bar{1}0]$ directions. Similar to Figure 4.6 in Chapter 4, it reflects only the crystalline contribution to the AMR since the non-crystalline contribution is

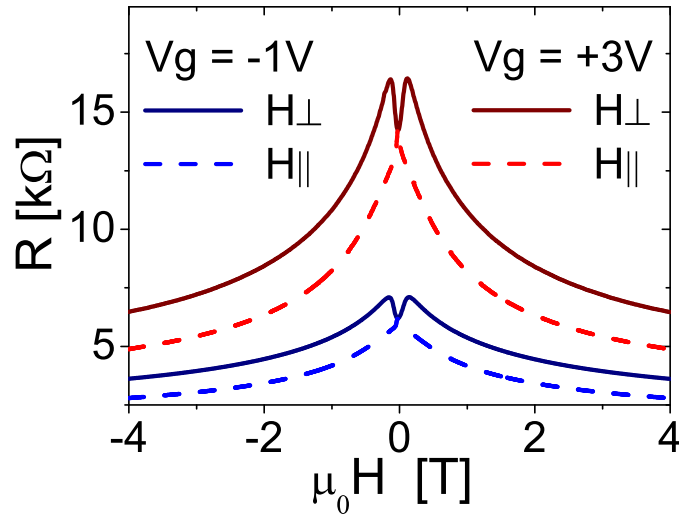


Figure 5.6: In-plane (H_{\parallel}) and perpendicular-to-plane (H_{\perp}) magnetic field sweep measurements of the channel resistance at -1 and +3 V at 4.2 K.

averaged to zero as the current flows in all radial directions in the Corbino geometry. It therefore reflects the same underlying symmetry breaking crystal fields as the magnetic anisotropy.

5.3 Persistent Magnetization Switching with Short Voltage Pulse

A variable width of hysteretic magnetization loops measured at different constant gate voltages, shown in Figure 5.8, is the prerequisite for observing electrically assisted magnetization switchings. Note that electrical measurements of magnetization reorientations utilized in Figures 5.9 and 5.10 are facilitated in our system by the IMR which responds to abrupt changes of the total magnetic induction upon a 180° reversal, and by a combined effect of the IMR and of the AMR for intermediate switchings by less than 180° . The amplitude of the AMR and the IMR contributions are similar in our experiments.

The switchings by short low-voltage pulses are demonstrated in Figure 5.9 and analyzed in detail in the following section. The experiments were performed at constant field-sweep rate of 0.1 mT per second starting from negative saturation field

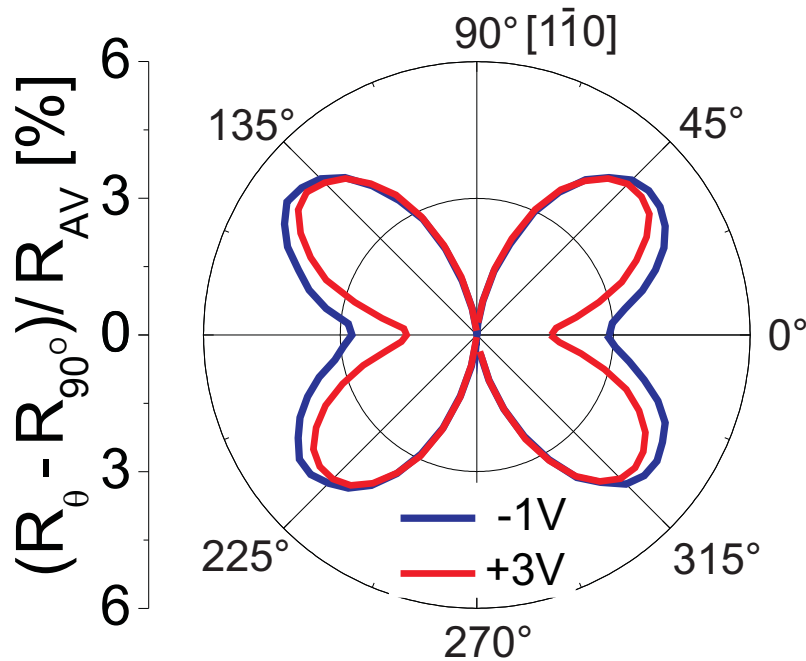


Figure 5.7: In-plane AMR measured at saturation (4T) in a rotating in-plane field at -1 and +3 V. R_{AV} is the average channel resistance measured across the entire angular range for the respective gate voltages.

of 1 T. The gate voltage was set to a base value of -1 V and then after each measurement step spanning 1 s, a 10 ms voltage pulse of a fixed magnitude was applied to the gate before returning to the base gate voltage. This technique was applied during the AMR detection and allows us to demonstrate the magnetic response to short electric pulses and the persistence of induced reorientations of the magnetization vector. It also removes potentially obscuring variations among the resistance traces in regions away from magnetization switchings which are caused by different slopes of the negative IMR at different gate voltages.

In Figure 5.9, measurement with no pulses (constant -1 V gate voltage) and data acquired at 0 to +4 V peak voltages are compared. The field was swept along the $[1\bar{1}0]$ crystal direction ($\theta = 90^\circ$, where θ is the in-plane field angle measured from the $[110]$ direction). As shown in detail in Section 5.4 and confirmed by SQUID magnetization measurements done by Dr. Olejník on an unpatterned part of the wafer, $[1\bar{1}0]$ is the main magnetic easy axis. The strong negative IMR facilitates the observation of the drop in R_c corresponding to a 180° reversal from an antiparallel

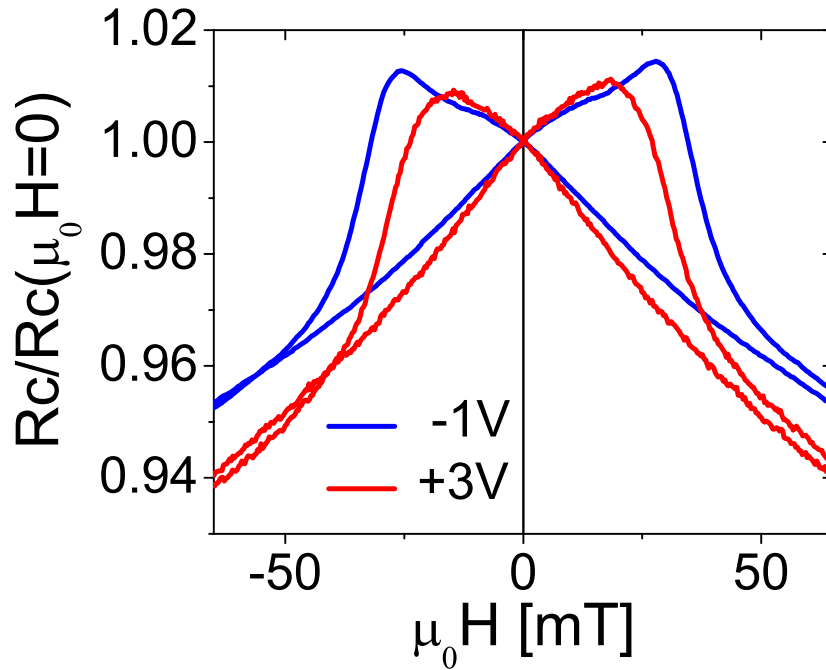


Figure 5.8: Hysteretic field sweep measurements at field angle $\theta = 90^\circ$ for constant gate voltages of -1 and +3 V.

to a parallel configuration of field and magnetization, and a corresponding increase of the magnetic induction. As the applied peak voltage increases, the magnetization reversals consistently shift to lower magnetic fields and the magnetization remains switched when the peak voltage pulse is turned off. As shown in Figure 5.9, the switching field, which is taken as the magnetic field at which there is a maximum change in the resistance, decreases from ~ 34.2 mT at -1 V to 26.4 mT at +4 V.

5.4 Theoretical Discussion

To discuss the detailed phenomenology of these persistent low-voltage induced magnetization switchings, field-sweep measurements at fixed field angles spanning the whole interval in 5° steps are presented in Figure 5.10. In panels (a) and (b), colour-maps of the resistance as a function of the field magnitude and angle for -1 V constant voltage and for the +3 V peak-voltage measurements, are shown respectively. The main effect observed in these plots is the overall suppression of the magnitude of the

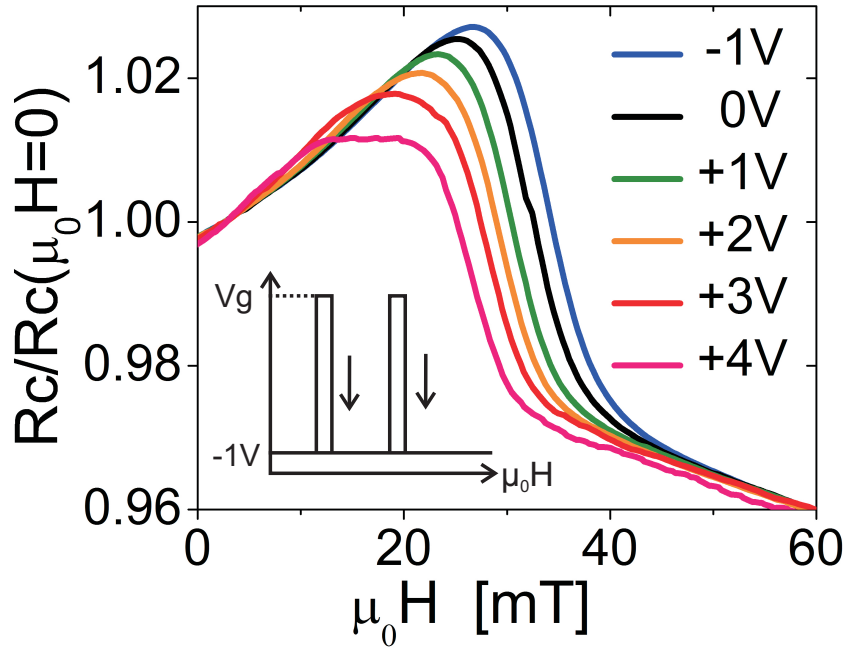


Figure 5.9: Up-sweeps of the $\theta = 90^\circ$ in-plane field at constant -1V gate voltage, and for measurements with the gate voltage set to a base value of -1V and with short additional voltage pulses corresponding to a total peak voltage of 0 , $+1$, $+2$, $+3$, and $+4\text{V}$, respectively.

switching fields by depletion. Additionally, the relative suppression is stronger at $\theta = 0^\circ$ (along the $[110]$ axis) than at 90° (along the $[1\bar{1}0]$ direction), as highlighted in Figure 5.11. This indicates that both the magnitude and ratio between the uniaxial and cubic anisotropy fields is modified by the gate voltage.

To quantify the depletion induced modification of the magnetic anisotropy, the anisotropy constants were extracted from fitting the measured $\theta = 0^\circ$ and 90° switching fields to a single domain anisotropy energy model,

$$E(\theta, \phi) = K_u \sin^2 \phi - \frac{1}{4} K_c \sin^2 2\phi - MH \cos(\theta - \phi) \quad (5.1)$$

where H and M are the magnitudes of the external field and magnetization, respectively, and ϕ is the magnetization angle. This simple model gives the lower bound for the anisotropy constants since other contributions to the magnetic anisotropy, such as shape and strain, are neglected in this model. Details for the calculation of the anisotropy constants are shown in Section 2.3.4 in Chapter 2. The uniaxial constant

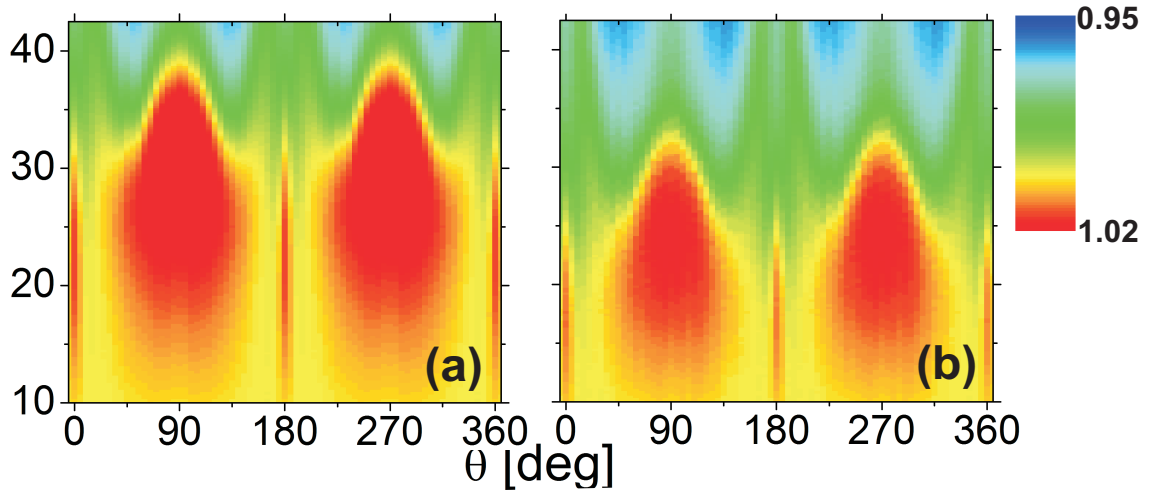


Figure 5.10: (a) and (b) Colour maps of channel resistance as a function of the in-plane field angle and magnitude (normalized to $H = 0$ resistance) for -1 V constant voltage and +3 V peak voltage measurements, respectively.

K_u is relatively weak compared to the cubic constant K_c , as shown in Figure 5.12. They both have a negative sign corresponding to the magnetic easy directions along the $[1\bar{1}0]$ and $[110]$ axes and the most easy direction along $[1\bar{1}0]$. As shown also from Figure 5.12, the dominant effect of depletion is in reducing the magnitude of K_c . Figure 5.12 shows how the corresponding anisotropy energy profiles at $H = 0$ evolve with depletion. The minima as shown in Figure 5.12 lie at both $[1\bar{1}0]$ and $[110]$ directions with a greater dip along the $[1\bar{1}0]$ direction, consistent with what was observed. As the (Ga,Mn)As epilayer is depleted, the anisotropy energy decreases in magnitude, especially along the cubic directions. The anisotropy energy is suppressed by more than half from -1 V to +4 V along the diagonals between crystalline easy axes (i.e. it is possible to induce magnetically-assisted switchings by gating pulses).

The key experimental observations are now discussed, employing the $\mathbf{k} \cdot \mathbf{p}$ semiconductor theory approach combined with the mean-field kinetic-exchange model of hole mediated ferromagnetism in (Ga,Mn)As [20, 76].

Calculations, done by Dr. Zemen and Prof. Jungwirth, for 2.5% local moment doping and hole density $p \sim 1 \times 10^{20} \text{ cm}^{-3}$, for which the simulations in Figure 5.2 predict hole depletions consistent with the measured variations of the channel re-

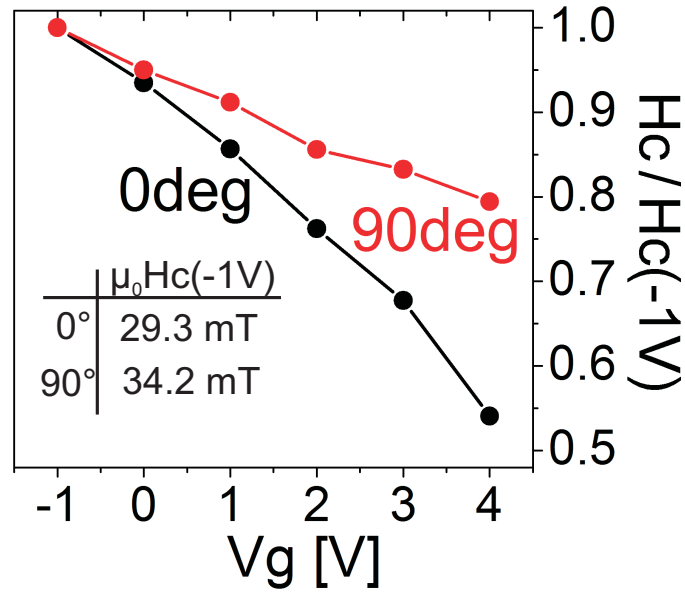


Figure 5.11: Switching fields at field angles $\theta = 0$ has a stronger suppression than at 90° as a function of the gate voltage.

sistance at temperatures near T_C , yield $T_C \sim 20$ K and $dT_C/dp \approx 1 \times 10^{-19}$ Kcm³. Both the absolute value of the Curie temperature and the few Kelvin suppression of T_C at a $\sim 20\%$ hole depletion predicted by the theory are consistent with the p-n junction simulations and the measured gate-dependent T_C values.

The semiconductor theory modelling which includes strong spin-orbit coupling effects in the host semiconductor valence band captures also the sensitivity of magnetocrystalline anisotropies in (Ga,Mn)As to hole density variations. The cubic anisotropy is included by accounting for the zincblende crystal structure of GaAs in the $\mathbf{k} \cdot \mathbf{p}$ model. The additional weak uniaxial anisotropy is often present in (Ga,Mn)As epilayers but its microscopic origin is not known and therefore, only the stronger cubic anisotropy term is calculated and discussed here. As shown in Figure 5.13, the microscopically calculated K_c constant changes sign at hole density of approximately 1.5×10^{20} cm⁻³. Below this density it favours the $[110]/[1\bar{1}0]$ magnetization directions, consistent with the experimental data. The typical magnitudes of K_c of ~ 10 mT are also consistent with experiment. Considering the large gate action seen at low temperatures we can also associate, semi-quantitatively, the

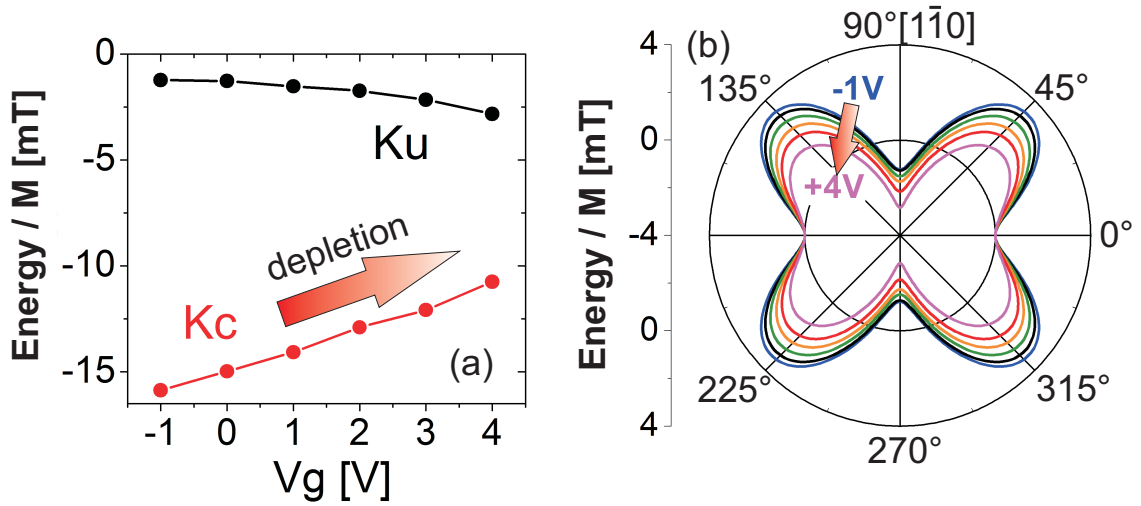


Figure 5.12: (a) Uniaxial and cubic anisotropy constants and (b) corresponding anisotropy energy profiles derived from the measured $\theta = 0$ and 90° switching fields. The calculations were done by Dr. Jöerg Wunderlich.

decreasing magnitude of the experimental K_c at depletion with the behavior of the theoretical K_c at low hole densities. The arrows highlighted in Figure 5.12 and Figure 5.13 show a common decreasing trend in the magnitude of K_c with depletion of the (Ga,Mn)As epilayer.

5.5 Summary and Conclusions

This chapter demonstrates low-voltage control of magnetic properties of a p-n junction (Ga,Mn)As FET via depletion effect in the ferromagnetic semiconductor channel. A shift in T_C of ~ 2 K and enhanced AMR (which at saturation reaches $\sim 30\%$) is achieved with a depletion of a few volts. Persistent magnetization switchings with short electric field pulses are also shown. By employing the $\mathbf{k} \cdot \mathbf{p}$ semiconductor theory approach, including strong spin-orbit coupling effects in the host semiconductor valence band, and accounting for the zinc-blende crystal structure of GaAs and focusing on the stronger K_c term, a change in sign of K_c at hole density of approximately $1.5 \times 10^{20} \text{ cm}^{-3}$ is observed. Below this density, the $[110]/[1\bar{1}0]$ magnetization directions are favoured, consistent with experimental data.

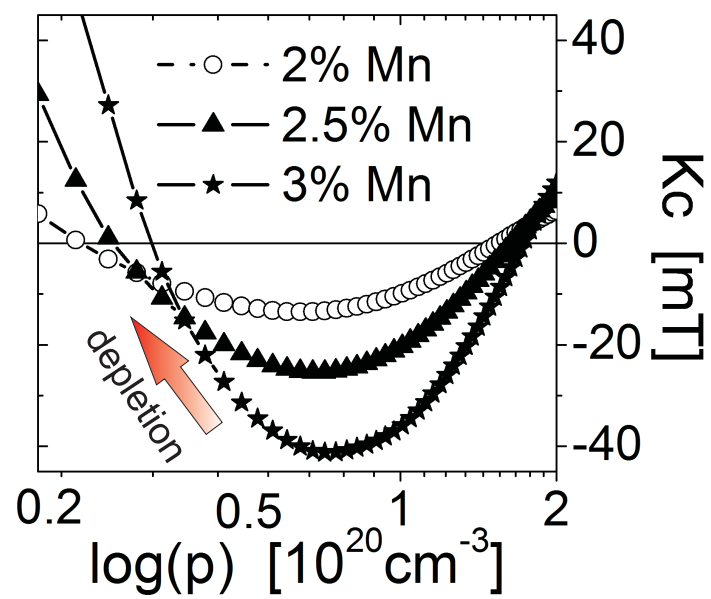


Figure 5.13: Microscopic calculations of the cubic anisotropy constant. Arrows in Figure 5.12 and here highlight the common trend with depletion. The calculations were carried out by Dr. Jan Zemen and Prof. Jungwirth.

Chapter 6

Double-gating: Ionic gel top-gate in addition to n-type built-in back-gate

As shown in the previous chapter, we have observed persistent magnetic switching with the application of short voltage pulses through the back-gate. Large change in the channel resistance of up to $\sim 200\%$ has been observed at 4.2 K with the application of just a few volts, which may be due to the proximity of the metal-insulator regime in the ultra-thin (Ga,Mn)As layer. In this chapter, an ionic gel is added to the top surface of the device in addition to the presence of the n-type built-in back-gate. The electric double layer (EDL) gating provided by the use of the ionic gel top-gate gives additional gating effects on the side opposite to the p-n junction. One of the drawbacks of the top-gate is that ions are frozen out below the glass transition temperature (T_G) of the ionic gel, which is around 220 K. As such, no variation of the electric field by EDL gating is possible at low temperatures (eg. 4 K) below T_G . However, the top-gate can be used to pre-bias the (Ga,Mn)As layer at temperatures above T_G , while electrical gating can be done at lower temperatures (below T_G) with the back-gate. This potentially allows greater electrical control, especially on devices made from very thin epilayer, since one gate can act as a pre-bias while the other is free for manipulation.

In this chapter, measurements obtained using the double-gated (Ga,Mn)As FET

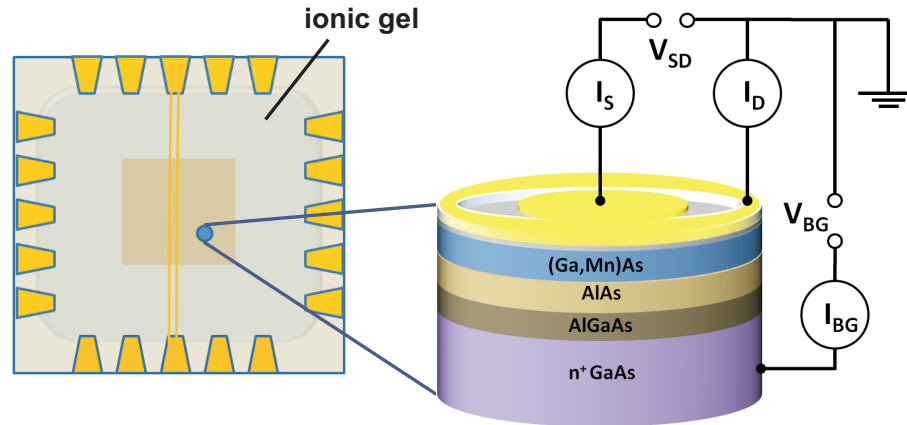


Figure 6.1: Schematic diagram of the FET structure used. (Left) Top-view of the device, the 2 Al wires linking across the channel are used as the metallic contact (top gate) to the ionic gel

are presented.

6.1 Device structure

The same (Ga,Mn)As wafer (E028) as described in Chapter 5 is used. The 5 nm, nominally 2.5% Mn-doped (Ga,Mn)As channel is grown on an insulating layer comprising 10 nm AlAs and 10 nm of AlGaAs which acts as a barrier to support the p-n junction structure. This is followed by a heavily Si-doped ($2 \times 10^{18} \text{ cm}^{-3}$) n-type GaAs substrate which forms the back-gate. The (Ga,Mn)As epilayer is also capped by a 2 nm thick insulating GaAs to protect it from oxidation and surface reactions with the ionic gel. The Corbino disc device structure is fabricated as described in Chapter 3. It consists of an inner circular contact and an outer ring contact of diameters $200 \mu\text{m}$ and $400 \mu\text{m}$ respectively. An ionic gel is then used to form the EDL for the top gate. It consists of the ionic liquid, formed from 1-ethyl-3-methylimidazolium bis(trifluoromethylsulfonyl)imide ([EMIM][TFSI]) (0.9 wt%), mixed with PS-PEO-PS tri-block copolymer (1.7 wt%), dissolved in acetonitrile. Details of the mechanism of the ionic gel gating is discussed in the theoretical chapter. The ionic gel is then dropped to cover the whole device with two aluminium wires used to form the top-gate contacts, as shown in Figure 6.1. The structure is

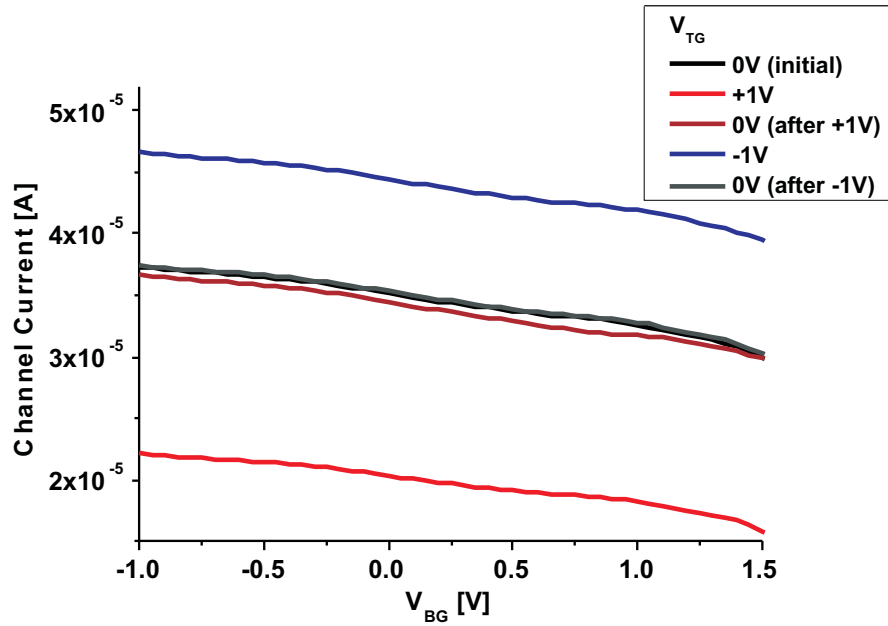


Figure 6.2: Channel current versus back-gating voltage curves for different top-gating steps. For this set of measurements, the top-gate voltage is limited to ± 1 V. The leakage current is found to be negligible within this range for the back-gate.

completed by sealing the bonding package with a glass substrate cover.

6.2 Ionic gel gating

Besides the draw-back of the immobile ions at low temperatures which means that top electrical gating cannot be done in-situ during the experiments below T_G , a number of other difficulties were met in using ionic gel gating due to possible electro-chemical reactions on the surface of the device upon the application of the top-gate voltage as soon as it gets above ± 1 V.

Figure 6.2 shows the channel current versus back-gating curves for different top-gating steps. To gauge a suitable top-gate voltage range for the actual device without compromising its integrity due to possible electro-chemical reactions, a test device is used in a trial for different top-gating steps. The test device used is selected from a wafer similar to the measured sample except for the Mn concentration in

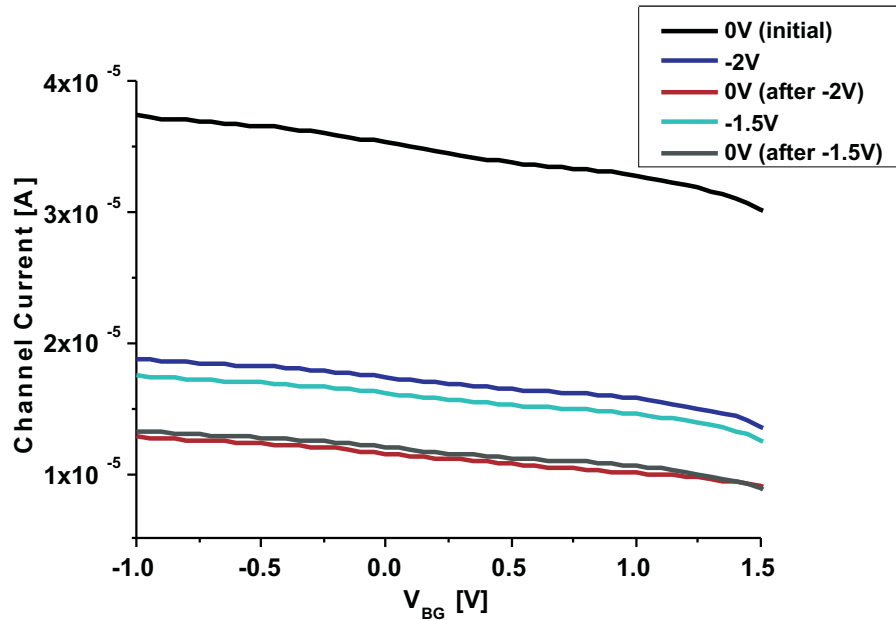


Figure 6.3: Channel current versus back-gating voltage curves for different top-gating steps. Top-gate of -2 V is applied and permanent degradation of the channel layer is observed.

the (Ga,Mn)As epilayer which is 3.5% instead of the lower 2.5% in the measured sample. Since both wafers have the same capping layer of 2 nm thick GaAs, the results obtained are also valid for the actual device. The measurement steps taken are as follows. First, the bottom-gate voltage dependence of the channel current is measured at 4.2 K after the application of the ionic gel without any applied top-gate voltage (V_{TG}) bias. The device is then biased with V_{TG} at +1 V at room temperature before it is cooled quickly in a helium dewar at 4.2 K for the second measurements. The above step is repeated with V_{TG} being re-set back to 0 V to check for any sign of chemical degradation. The same steps are again repeated for different V_{TG} , in particular for -1 V and 0 V as shown in Figure 6.2. The plots of the channel currents for V_{TG} at 0 V at different top-gating steps are almost identical. This gives us the confidence that gating within the range of ± 1 V is possible.

Figure 6.3 shows as an example, the onset of electro-chemical degradation within the epilayer. Using the same test device as above, a V_{TG} of larger magnitude at -2 V

was applied. As observed in the above plot, the channel current is lowered even with the accumulation in the epilayer with the negative gate bias, contrary to what was expected. With the negative V_{TG} lifted off as the V_{TG} is re-set to 0 V, the channel current is lowered further. After the two steps, V_{TG} of -1.5 V is again applied. This time, the expected behaviour returned with the magnitude of the channel current increased by $0.5 \mu\text{A}$ as compared to V_{TG} at 0 V. When the V_{TG} is again re-set back to 0 V, the channel current falls back to what was before V_{TG} of -1.5 V was applied. This is a result of a chemical degradation or ion penetration of the (Ga,Mn)As layer (refer to Section 2.5.3 in Chapter 2) when too large a top-gate voltage is applied.

After determining a feasible regime for V_{TG} , additional precautions are also taken to prevent any electro-chemical reactions. The device is measured right after the application of the ionic gel. Moreover, application of the top-gate voltage is only done when the device is placed in a He_2 -rich environment at a temperature of ~ 260 K, just above the glass transition temperature. The He_2 -rich environment achieved after purging the sample space with He gas a few times reduces the water content in which the device is charged. This minimizes possible chemical reactions as water content or OH^- ions dissolved in the ionic gel is thought to be the main ingredient responsible for the surface electro-chemical reactions. Charging at a lower temperature would also help to reduce the rate at which any electro-chemical reactions can take place.

6.3 Channel Resistances and Curie Temperatures

First, we investigate the effects of gating on channel resistances. Figure 6.4 shows the channel resistance versus temperature graph. Both the EDL top-gate and the back-gate are used. The device was first measured with gate voltages set to 0 V (black line)(i.e. Both the top and bottom-gate are set to the common ground). A top-gate voltage (V_{TG}) of -1 V and a back-gate voltage (V_{BG}) of -1 V is then applied (blue line). The channel resistance is then measured again while the sample's temperature increases. This process is repeated for V_{TG} of +1 V and a back-gate voltage (V_{BG}) of +2 V (red line), and then again with V_{TG} of -1 V and V_{BG} of -1 V (cyan line). Upon

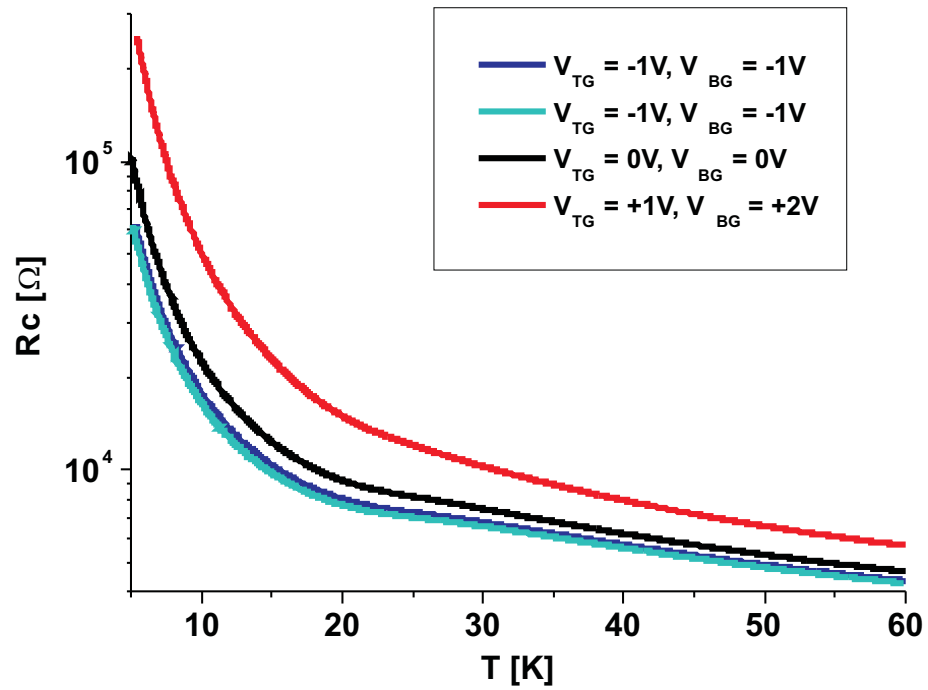


Figure 6.4: Channel Resistance versus temperature for different gate voltages.

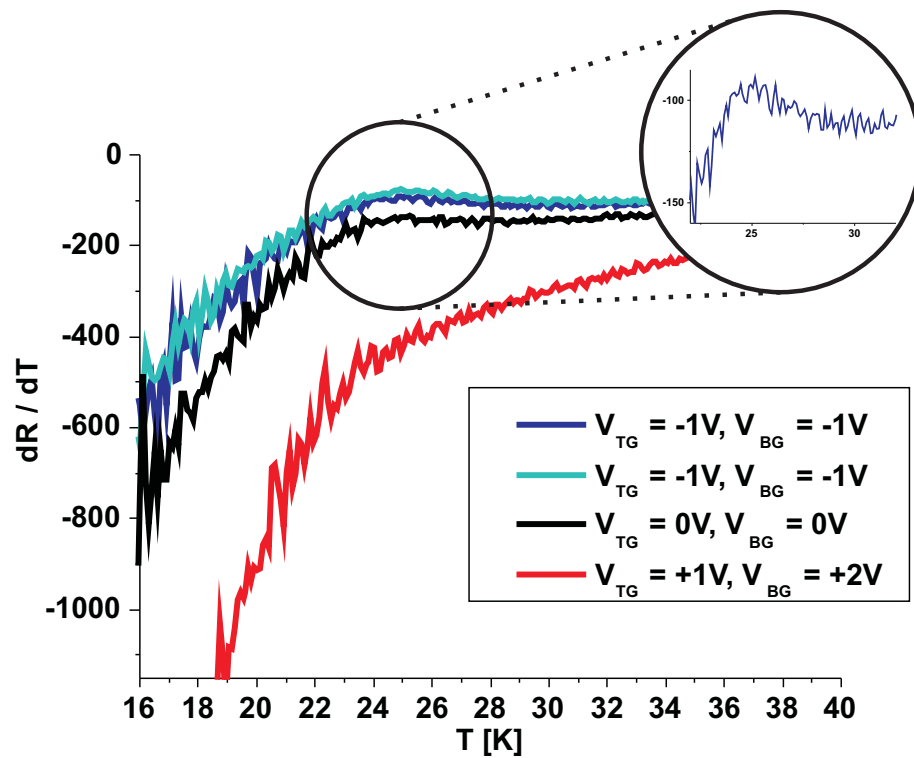


Figure 6.5: Derivative of the channel resistance for different gate voltages is plotted. The inset shows a broad peak observed for $V_{TG} = -1$ V with $V_{BG} = -1$ V.

application of V_{TG} of -1 V and V_{BG} of -1 V again on the last step, the resistance traced back to the original resistance with the same setting. The reproducibility shows that the device is not degraded during the measurement cycle. At 40 K, the channel resistance increased by approximately 40% with the application of positive voltages. At low temperatures, the gating effect is strongly enhanced; at 5.5 K the increase of R_c between -1 and +3 V is by more than 450%. This is far larger than what was measured by just bottom-gating alone as shown in the previous chapter.

In Figure 6.5, differentiated resistivity curves obtained in our device for the various V_{TG} and V_{BG} from the data in Figure 6.4 are shown. From the plots, there is no observable peak in dR/dT for the case of depletion of holes and a broad peak (inset) for the case of accumulation of holes with $V_{TG} = -1$ V and $V_{BG} = -1$ V. One reason for this is the inhomogeneity of the (Ga,Mn)As layer. The very broad or even no singularities seen could be a result of the superposition of many of these singularities measured for different parts of the (Ga,Mn)As with different Mn concentrations, which masks the singularity signal we would otherwise observe in thicker, homogeneous (Ga,Mn)As films [70]. Another reason could be the proximity of the metal-insulator regime in this ultra-thin (Ga,Mn)As layer. This gives a very strong dependence of the channel resistance with temperature, especially for the strongly depleted (Ga,Mn)As layer (ie. $V_{TG} = +1$ V and $V_{BG} = +2$ V). The effective peak in the dR/dT could have been masked by this stronger effect.

6.4 Anisotropic Magnetoresistance

The in-plane magnetic crystalline anisotropy field can be examined qualitatively by the AMR measured in a saturated rotating in-plane magnetic field in the Corbino transistor. The measurements, shown in Figure 6.6, unveil a cubic anisotropy along the $[110]/[1\bar{1}0]$ crystal axes and an additional uniaxial term breaking the symmetry between the $[110]$ (0°) and $[1\bar{1}0]$ (90°) directions. For the individual sets of V_{TG} at -1 V (Figure 6.6(a)) and +1 V (Figure 6.6(b)) with V_{BG} at both -1 V and +2 V for each set, the bottom-gate dependence of the rotation AMR is similar to what was observed previously. For V_{TG} at -1 V, with a change in V_{BG} from +2 V to -1 V,

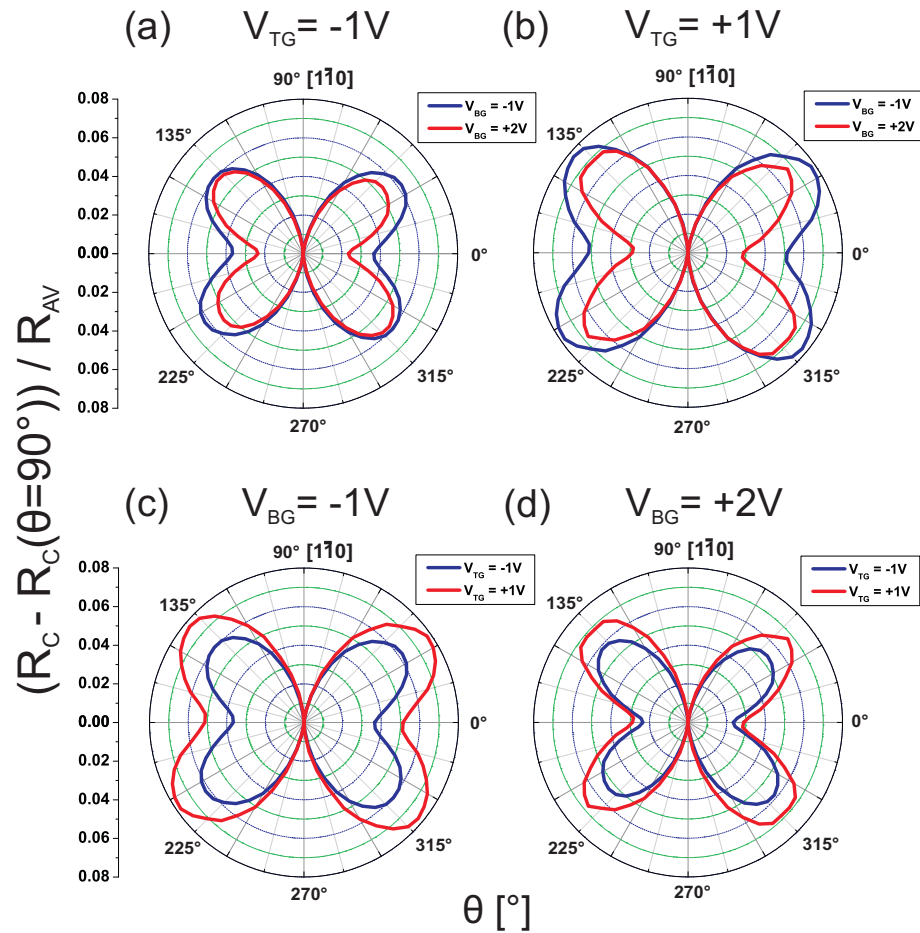


Figure 6.6: In-plane AMR measured at saturation (4T) in a rotating in-plane field for various gate voltages - at fixed (a) $V_{TG} = -1$ V, (b) $V_{TG} = +1$ V, (c) $V_{BG} = -1$ V and (d) $V_{BG} = +2$ V. R_{AV} is the average channel resistance measured across the entire angular range for the respective gate voltages.

there is an increase in the AMR of $\sim 1.5\%$ along crystalline direction of $[110]$. With V_{TG} at $+1$ V, a greater increase in the AMR of $\sim 2\%$ is again observed along the direction of $[110]$ when V_{BG} is changed from $+2$ V to -1 V. If the data for V_{BG} at -1 V and $+2$ V with the different V_{TG} s are compared, things look a little different. For V_{BG} at -1 V (Figure 6.6(c)), with a change in V_{TG} from $+1$ V to -1 V, instead of an increase, there is a decrease in the AMR of $\sim 1.5\%$ along the crystalline direction of $[110]$. Similarly, for V_{BG} at $+2$ V (Figure 6.6(d)), a change in V_{TG} from $+1$ V to -1 V decreases the AMR along $[110]$ by $\sim 0.5\%$. From this, it can be concluded that a larger change in the AMR can be induced by the double-gating.

The differences observed between the use of top-gate and bottom-gate could be a reflection of the inhomogeneity of the ultra-thin layer depending on which surface is being gated (cf. Section 6.3). For the top-gating, an electric double layer is formed on the top surface whereas for the bottom-gate, a depletion layer is formed at the intersection of the p-n junction. Since AMR is an effect depending on the scattering between carriers and both the Coulomb and magnetic potentials (refer to Section 2.4.2 in Chapter 2), it could be a ‘localized’ effect in regimes with higher carrier density. The inhomogeneity in the (Ga,Mn)As layer could thus give rise to AMR with opposite polarity for the two gating effects. In a sense, the inhomogeneity is expected in thin (Ga,Mn)As epilayers since for its low-temperature MBE growth, there would be a Mn concentration profile in (Ga,Mn)As with lower Mn doping in the region near the interface between (Ga,Mn)As and AlAs barrier, and a region of higher Mn doping near the top of the (Ga,Mn)As epilayer. Hence depletion of carriers near the top-interface and bottom-interface of the (Ga,Mn)As layer could result in a change in AMR in the opposite polarity. The different strain profile within the thin (Ga,Mn)As epilayer could also contribute to this anomaly.

6.5 Persistent Switching with voltage pulses

Similar to the previous experiments in Chapter 5, in-plane magnetic field sweeps for different angles (θ) with respect to the $[1\bar{1}0]$ crystalline direction were made with different voltage pulses. The results of the measurements are plotted in Figure 6.7.

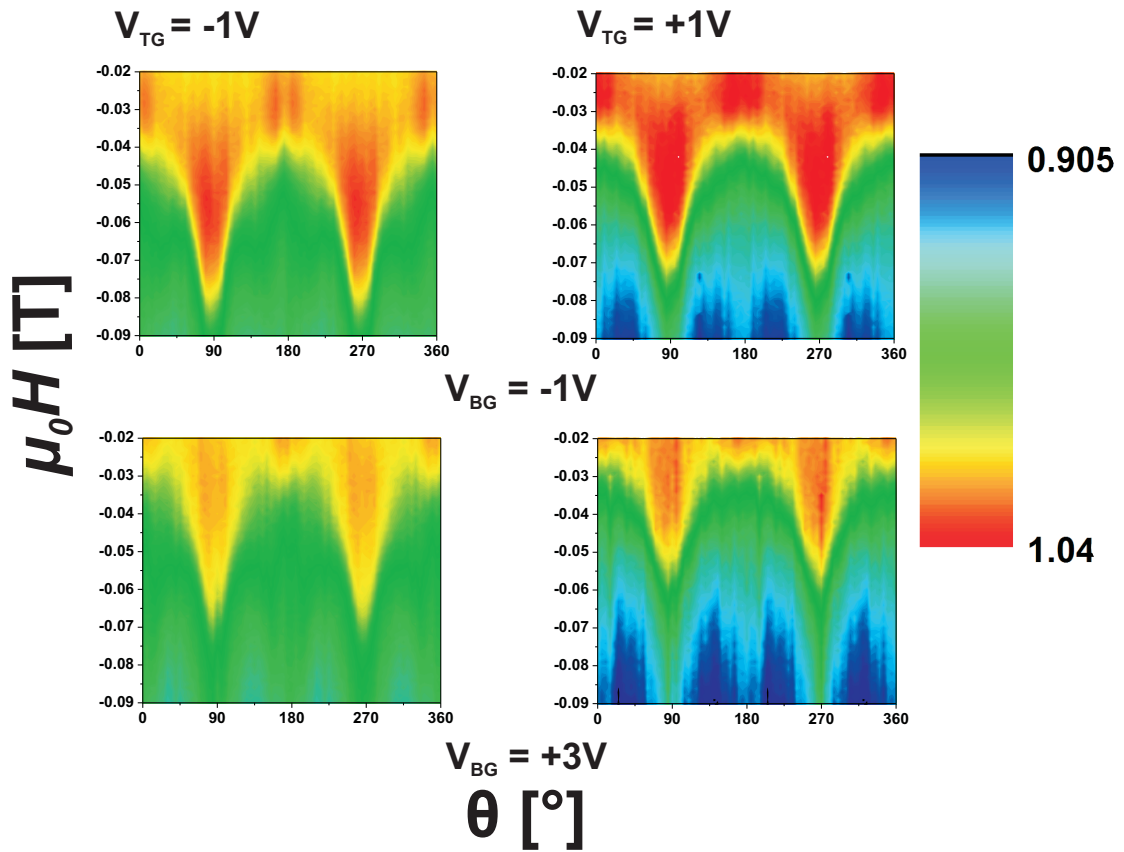


Figure 6.7: Colour maps of channel resistance as a function of the in-plane field angle and magnitude (normalized to the channel resistance at $H = 0$) for -1 V constant voltage and +3 V peak voltage measurements (V_{BG}) for two different top-gate voltages, V_{TG} , of -1 V (left panels) and +1 V (right panels).

The experiments were done with the magnetic field being swept from the positive saturation field of +0.1 T for V_{TG} at +1 V, while from +0.12 T for V_{TG} at -1 V. In contrast to a constant magnetic field sweep rate of 1 mT per second, measurements were taken in this set of data for every 1 mT. For further details of the set-up of the experiment, please refer to Chapter 3.

The colour plots shown in Figure 6.7 have been adjusted specifically to be on the same scale so that the magnitude of the AMR can be compared across different gate voltages. It is observed that the magnitude of the AMR generally increases when V_{TG} is increased from -1 V to +1 V. The ‘W’ shape of the colour plot reveals the underlying symmetry of the crystalline anisotropy field in the (Ga,Mn)As epilayer. Looking at individual set of data with the same V_{TG} and at $\theta = 90^\circ$ (along $[1\bar{1}0]$ crystalline axis), it is observed that upon a depletion of the channel layer from V_{BG} at -1 V to +3 V, the switching field is suppressed from a magnitude of ~ 80 mT to ~ 70 mT for V_{TG} at -1 V and from ~ 75 mT to ~ 60 mT for V_{TG} at +1 V.

This is illustrated more clearly in Figure 6.8 where the colour map of the first derivative of the channel resistance with respect to the in-plane magnetic field is plotted. The switching field is taken where the magnitude of the derivatives are at the maximum. More qualities of the double gating can be illustrated through this colour plot. Again, the larger magnitude for the first derivative is observed when V_{TG} is increased from -1 V to +1 V. The increase in the magnitude of the first derivative implies steeper slopes on the magnetic field sweeps. In contrast, when the channel layer is depleted with V_{BG} from -1 V to +3 V, the magnitude of the first derivatives is suppressed. The decrease in the magnitude of the first derivative is related to the decrease in the magnitude of MR peak (say for the case of fixed V_{TG} and a change in V_{BG} from -1 V to +3 V) since a “flattened” magnetic field sweep curve (from the AMR maxima to the switching by 180° reversal say along the major easy axis) could result in a gentler switching slope than if one has a larger maxima (cf. Figure 5.9 in Chapter 5).

Besides the change in magnitudes, it is observed that the ‘W’ shape of the plot is flattened with depletion. This is true for both top and back-gating. The shifting of the switching fields and the flattening of the ‘W’ shape (i.e. the difference

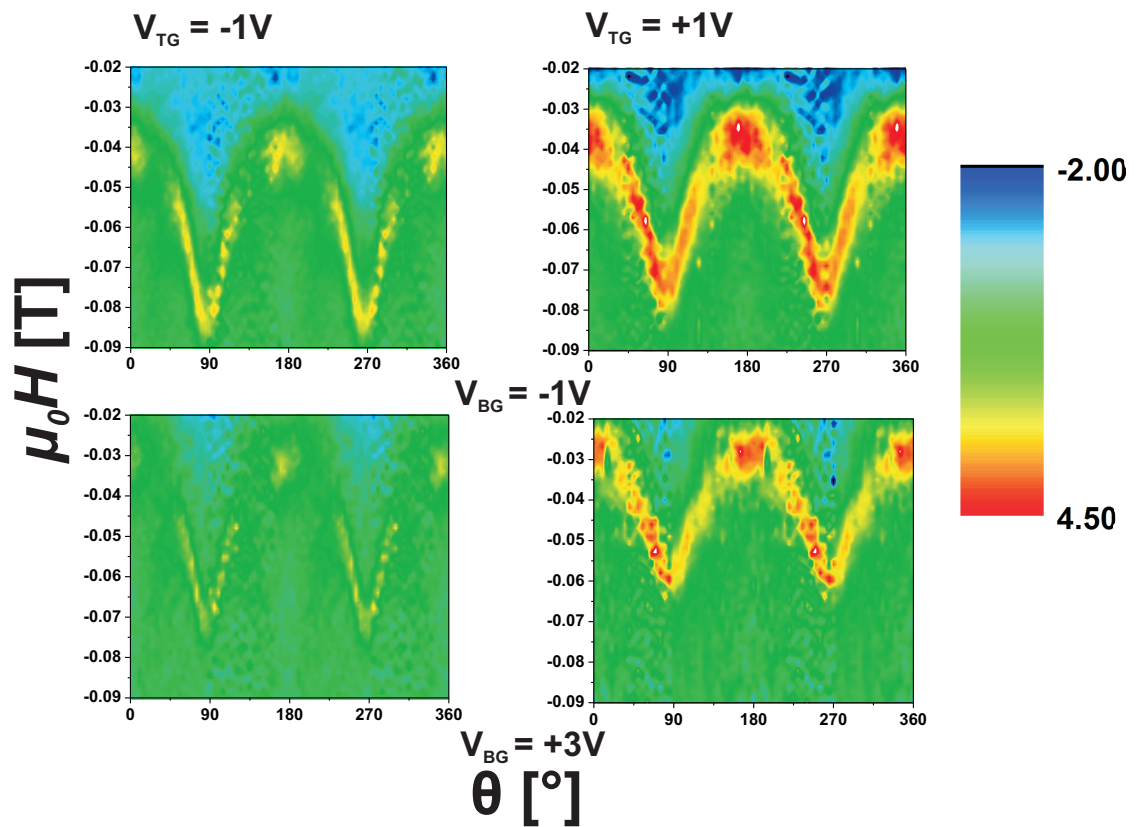


Figure 6.8: Colour maps of the first derivative of channel resistance for the data shown in Figure 6.7. The magnitude of the first derivative in the colour plot is of arbitrary unit.

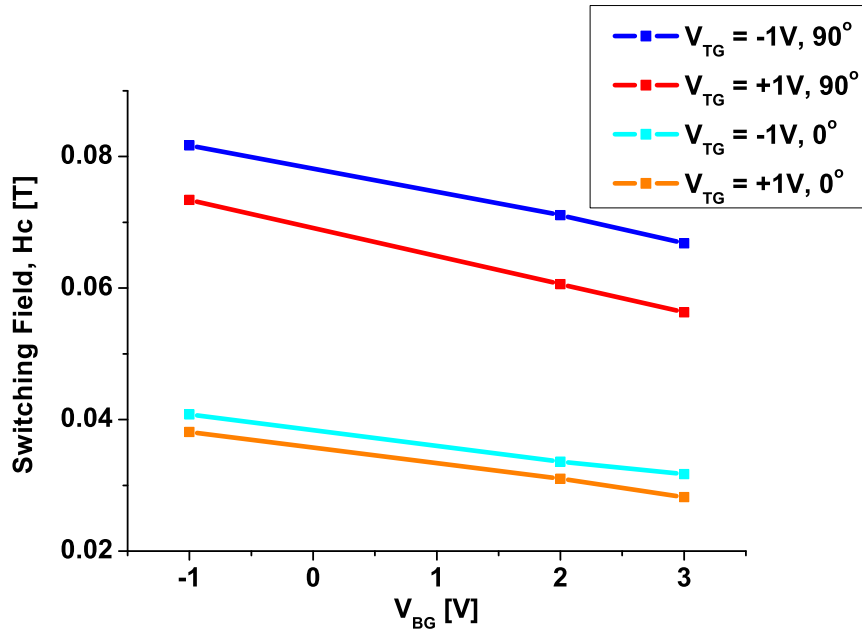


Figure 6.9: The values of the switching field for different top and bottom gate voltages along the 0° $[110]$ and 90° $[1\bar{1}0]$ directions.

between the switching fields for θ at 0° and 90°) is important in determining the effects of the electrostatic gating on the anisotropy fields of (Ga,Mn)As (refer to Section 2.3.4 in Chapter 2 which gives the relationship between the switching fields at $\theta = 0^\circ$ and 90° to the anisotropy constants, K_u and K_c). Using an identical method to the previous chapter via the simple single domain anisotropy energy model, the anisotropy constants can be found. The uniaxial anisotropy constant (K_u) is proportional to the difference of the switching fields at both 0° and 90° whereas the cubic anisotropy constant (K_c) is proportional to their sum. From the plot, it can be observed that the shift in the switching fields is larger than the flattening of the ‘W’ shape. This reflects qualitatively the dominant effect of gating on K_c .

The values for K_u and K_c are calculated from the experimental values of the switching fields at both 0° and 90° . The values of the switching fields for different top and bottom gate voltages are shown in Figure 6.9. The switching fields at 90° generally have higher magnitude compared to those at 0° , which correspond to the major and minor easy axes respectively. The switching fields are also generally

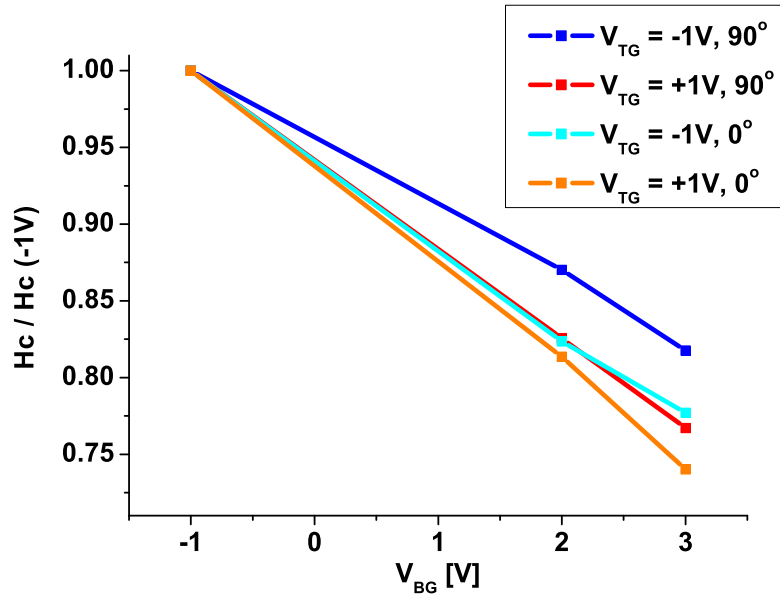


Figure 6.10: Normalized switching field with respect to $V_{BG} = -1$ V for each V_{TG} and along both 0° $[110]$ and 90° $[\bar{1}\bar{1}0]$ directions for different V_{BG} .

suppressed with depletion of the channel layer. At 90° , the switching field decreases from 82 mT to 67 mT for V_{TG} at -1 V from a change of V_{BG} of -1 V to +3 V. For V_{TG} at +1 V, the switching field decreases from 73 mT to 56 mT for a similar change in V_{BG} . A similar trend is also observed for 0° . The switching field at 0° decreases from 41 mT to 32 mT for V_{TG} at -1 V from V_{BG} of -1 V to +3 V. For V_{TG} at +1 V, the switching field decreases from 38 mT to 28 mT for V_{BG} from -1 V to +3 V. A closer look at the plot reveals that the effect of depletion of the layer with the top-gate is the same as that of the bottom-gate – to suppress the switching field (i.e. making it easier to switch magnetization and hence decreasing or negating the crystalline anisotropy field in the epilayer). The top-gate serves as a pre-bias to enhance or lower the magnetic coercivity as necessary. From the graph for 90° , it suggests that the top-gate bias has just offset the plot up or down with the same gradient on the line, so that an increase of V_{TG} from -1 V to +1 V is similar to that of V_{BG} from -1 V to +1.5 V. The effect for 0° is however much smaller.

Additionally, the relative suppression is stronger at $\theta = 0^\circ$ (along the crystalline $[110]$ axis) than at 90° for V_{BG} , as highlighted in Figure 6.10. The depletion of

the epilayer with the top-gate also creates a stronger relative suppression for both crystalline easy axes.

Figure 6.11 shows the calculated K_u and K_c values for the different gate voltages. These values are calculated from the assumption of a single domain anisotropy energy model, similar to the previous experiment in Chapter 5. From the graph with fixed V_{TG} and varying V_{BG} as shown in Figure 6.11, it is observed that the dominant effect of gating on the (Ga,Mn)As epilayer is in suppressing the value of K_c with the depletion of the hole density in the epilayer. From Figure 6.11(b), the magnitude of K_c decreases from 31 mT to 25 mT with V_{BG} from -1 V to +3 V for $V_{TG} = -1$ V, and from 28 mT to 21 mT for V_{TG} at +1 V. The same trend is observed on K_u is observed in Figure 6.11(a), with the values of K_u decreasing from a magnitude of 10 mT to 9 mT with V_{BG} from -1 V to +3 V for V_{TG} at -1 V, and 9 mT to 7 mT for V_{TG} at +1 V. Looking at the plot of K_u and K_c values with fixed V_{BG} and varying V_{TG} (Figure 6.12) and comparing with the previous Figure 6.11, depletion of the layer from the top-gate seems to have a similar effect. With a difference of 2 V in V_{TG} (i.e. from -1 V to +1 V), the magnitude of K_c decreases from 31 mT to 28 mT for V_{BG} at -1 V, and K_c from 25 mT to 21 mT for V_{BG} at +3 V. Similar effect by the top-gating is also observed for K_u .

Surprisingly, this does not follow the same trend in the AMR for the two different gating mechanisms as shown in Figure 6.6: depletion of carriers in the (Ga,Mn)As layer by the top-gate increases the magnitude of AMR while that by the back-gate decreases the AMR. As discussed briefly in Section 6.4, a reason could be that AMR is a more ‘localized’ effect which originates mainly from the region in the (Ga,Mn)As layer with the highest carrier density. The shift of the carrier cloud in the magnetic layer by gating from the surface (top-gate) and from the p-n junction back-gate can be very different and so it is possible for AMR to show different trends with the top- and back-gating. However for the magnetic anisotropy as seen in Figure 6.12 and 6.11, it is a measure of a more global property in the (Ga,Mn)As layer. Hence, this ‘average’ effect within the ferromagnetic epilayer has the same trend with depletion of holes whether it is by the top- or the back-gate.

In addition, it can be observed that biasing with V_{BG} does not affect the action

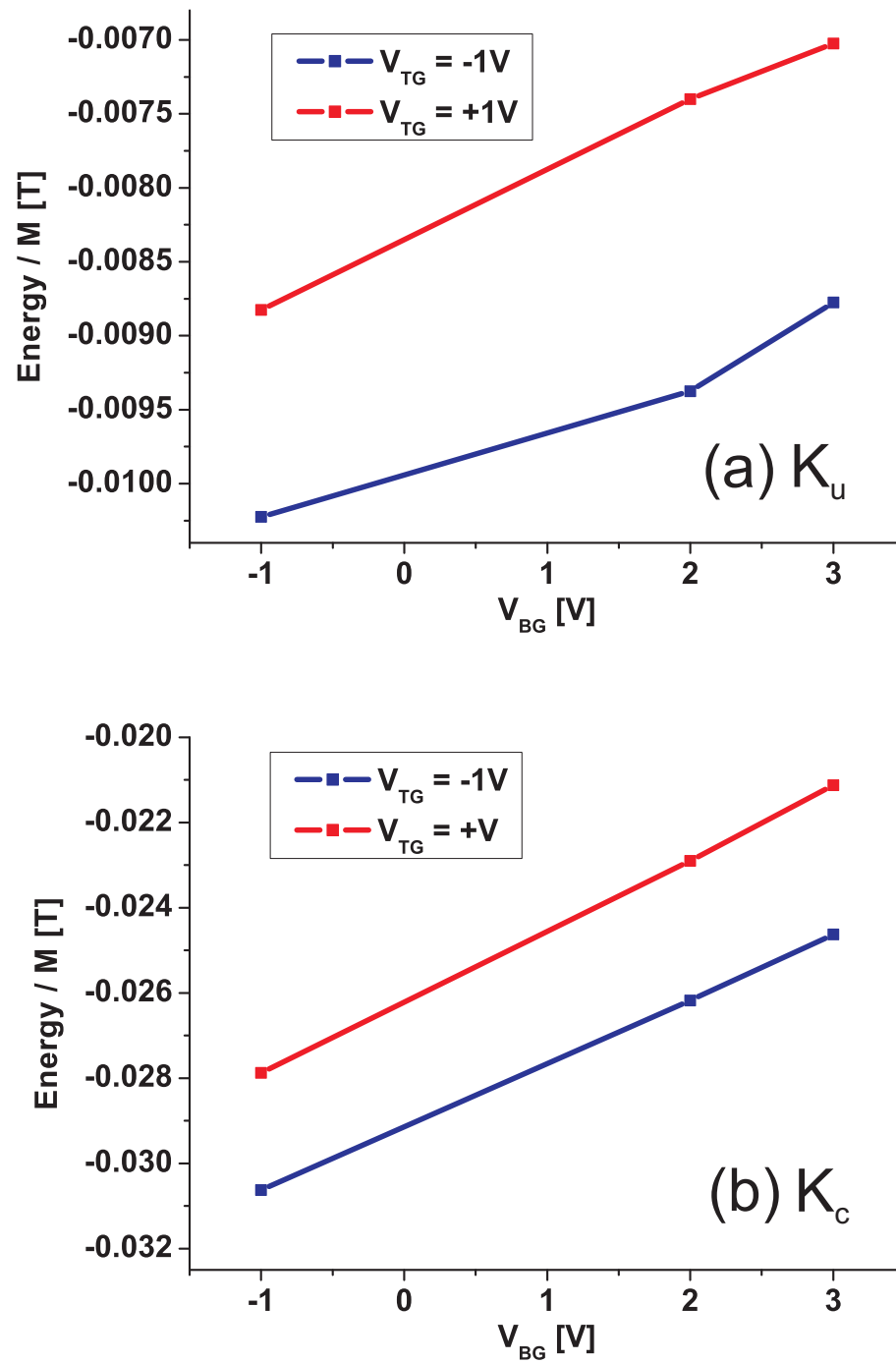


Figure 6.11: (a) Uniaxial and (b) cubic anisotropy constants for different gate voltages derived using equations from Section 2.3.4 in Chapter 2 for fixed V_{TG} .

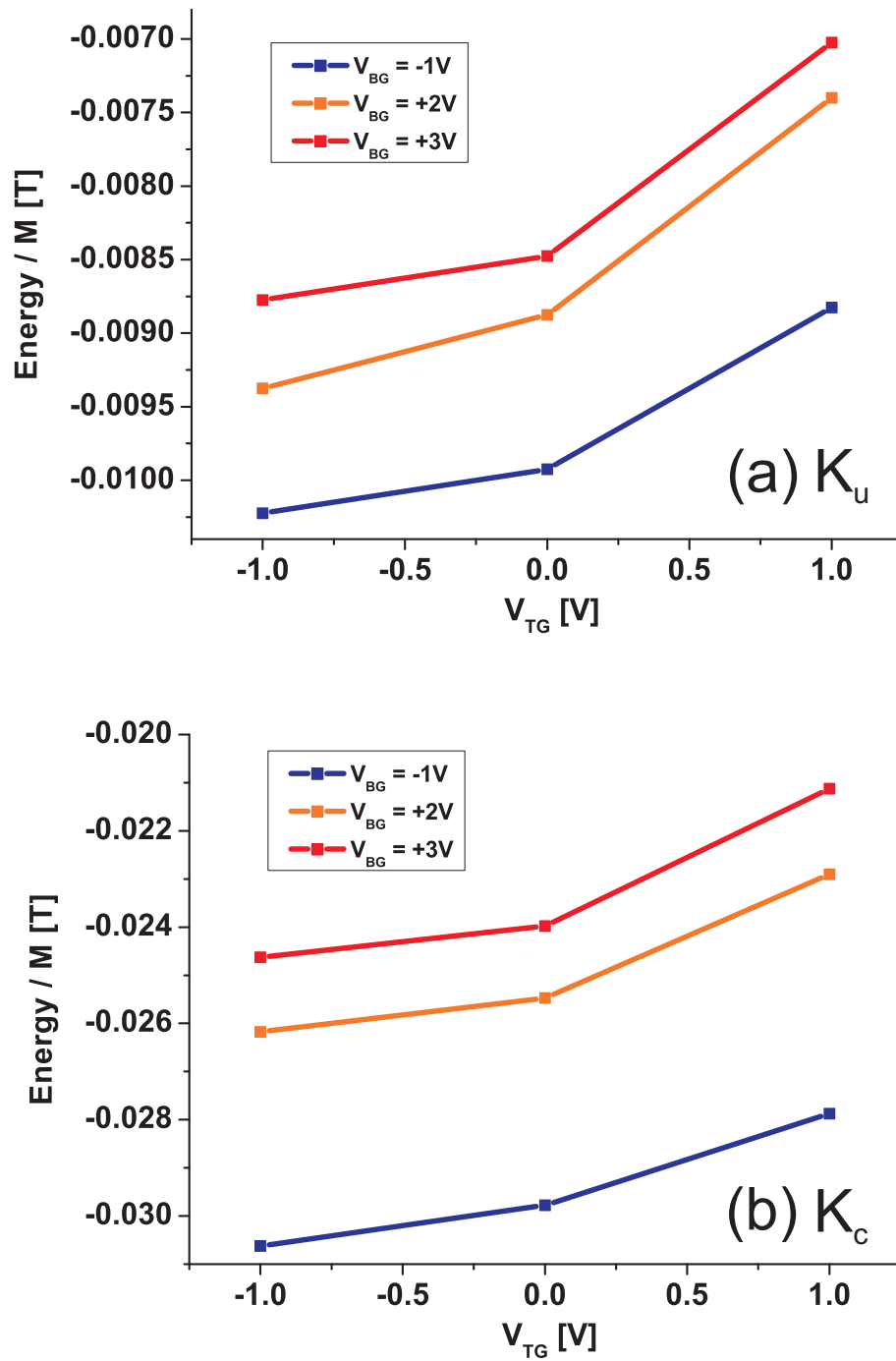


Figure 6.12: (a) Uniaxial and (b) cubic anisotropy constants for different gate voltages derived using equations from Section 2.3.4 in Chapter 2 for fixed V_{BG} .

of V_{TG} (as observed from the similar gradient of the change in K_c as well as the switching fields in Figure 6.9). The top-gate can then be exploited as a leverage to bias the values of K_c and K_u as the two gates act independently.

6.6 General remarks

Comparing the effects on AMR, switching fields and the anisotropy constants by gating with the back-gate (V_{BG}) and with the top-gate V_{TG} , the effects induced by the top-gate were not as significant as expected. In fact, the magnitudes of the effects by gating with V_{TG} from -1 V to +1 V were similar to that for V_{BG} from -1 V to +3 V. A typical capacitance achieved with the [EMIM][TFSI] ionic gel is $\sim 15 \mu\text{Fcm}^{-2}$ [69]. For this case, one would expect an induced change in the carrier density of $\sim 5 \times 10^{13} \text{ cm}^{-2}$ for a change of 2 V (say -1 V to +1 V in V_{TG}). This should theoretically be able to deplete the 5 nm (Ga,Mn)As layer fully since a 2.5% Mn-doped (Ga,Mn)As usually has a hole concentration of $\sim 10^{20} \text{ cm}^{-3}$. In our case, we should still be able to change the hole concentration by $\pm 50\%$ with the top-gate. One would then expect a much larger gating effect induced by the top-gate than by the back-gate (cf. Figure 5.2 in Chapter 5).

One possible reason for the diminished top-gating effect is the presence of the 2 nm insulating GaAs protective layer on top of the (Ga,Mn)As epilayer. Assuming a simple model of parallel-plate capacitors, including both the 0.7 nm [69] thick EDL layer with a dielectric constant of 24 [69] and the 2 nm thick insulating GaAs layer with a dielectric constant of 12.9 [63], the effective capacitance of this coupled layer drops to $\sim 4.8 \mu\text{Fcm}^{-2}$. This is about 1/3 of what was originally expected. This can thus account for the smaller than expected induced change in the hole concentration and consequently, the gating effects on the magnetic properties of (Ga,Mn)As by the EDL top-gate.

6.7 Summary and Conclusions

In this chapter, the results from the previous chapter have been reaffirmed with a similar device grown on the same wafer. Double-gating has been employed in an attempt to achieve a larger gating effect. Similar to the previous experiment, persistent magnetization switchings are observed with short voltage pulses, with the dominant effect being a suppression of the magnitude of K_c with depletion of the epilayer. An interesting but unexpected difference on the effect of gating on AMR is observed with the top and bottom gating: the magnitude of AMR increases with depletion of holes using the top-gate but decreases with depletion using the bottom-gate. This reflects the inhomogeneity of the (Ga,Mn)As epilayer used. In addition, the diminished gating effects for the electric double layer (EDL) gating is a result of the use of the 2 nm thick insulating GaAs protective layer on top of the (Ga,Mn)As. Overall, the effects achieved by electrical gating on the (Ga,Mn)As epilayer is enhanced using the double-gating method.

Chapter 7

Conclusions and Future Outlook

A summary of the experimental results in Chapters 4, 5 and 6 of this thesis is presented in the first half of this chapter. In the second half, potential research directions based on the results of this work are discussed.

7.1 Conclusions

Studies presented in this thesis are focused on the effects of electrical gating on the magnetic properties of (Ga,Mn)As diluted magnetic semiconductors. Chapter 4 outlines preliminary study done on an all-semiconductor epitaxial p-n junction field effect transistor (FET). More detailed examination of the effects of gating, in particular the persistent magnetization reversal with gate-voltage pulses, was carried out in Chapter 5. Finally in Chapter 6, a double-gated FET structure was fabricated and examined: a p-n junction back-gate coupled with an ionic-gel top-gate. Independent gate-actions on the magnetic properties of (Ga,Mn)As were observed.

7.1.1 P-N Junction gating

The main achievement of this study in Chapter 4 is the introduction of an all-semiconductor epitaxial (Ga,Mn)As p-n junction FET. The device was made from a 4 nm thick epilayer of $\text{Ga}_{0.92}\text{Mn}_{0.08}\text{As}$ grown on top of a 20 nm undoped AlAs barrier follow by a heavily n-doped epitaxial GaAs layer ($n = 2 \times 10^{18} \text{ cm}^{-3}$) which acts as the gate electrode. The general device characteristics and magnetic properties of

this back-gate FET device were measured. The magnetization vector is observed to lie in-plane and the effects of gating on anisotropic magnetoresistance (AMR) are observed. The Curie temperature of the device has been estimated to be between 35 K and 40 K through its AMR measured by out-of-plane magnetic field sweeps. Effects of in-plane and out-of-plane rotation AMR in a saturation magnetic field with gating are also examined. For in-plane rotation AMR, the magnitude of the AMR increases with increasing positive gate voltages, contrary to what is observed for the out-of-plane case. Systematic etching by oxide removal is also investigated which makes room for effective thinning of the sample and thus allowing for more effective gating.

7.1.2 Persistent magnetization reversal with voltage pulses

Chapter 5 provides more detailed examination of the effects of gating on a similar p-n junction back-gated FET. An improved wafer with a 2 nm GaAs protective layer (to protect the (Ga,Mn)As epilayer from unnecessary etching), low-doped $\text{Ga}_{0.975}\text{Mn}_{0.025}\text{As}$ (to provide a larger gating effect) and a graded barrier (to minimize leakage current) was used. A shift of T_C of ~ 2 K and enhanced AMR (which at saturation reaches $\sim 30\%$) is achieved with a depletion of a few volts. Persistent magnetization switchings with short electric field pulses are also shown. The switching fields are found to decrease in magnitude with increasing positive gate voltages (or depletion of the epilayer). By employing the $\mathbf{k} \cdot \mathbf{p}$ semiconductor theory approach, including strong spin-orbit coupling effects in the host semiconductor valence band, and accounting for the zinc-blende crystal structure of GaAs and focusing on the stronger K_c term, a change in sign of K_c at hole density of approximately $1.5 \times 10^{20} \text{ cm}^{-3}$ is observed. Below this density, the $[110]/[\bar{1}\bar{1}0]$ magnetization directions are favoured, consistent with experimental data.

7.1.3 Double-gating

In Chapter 6, the results obtained in Chapter 5 have been reaffirmed with a similar device grown on the same wafer. Double-gating – with an ionic-gel top-gate cou-

pled with a p-n junction back-gate – has been employed in an attempt to achieve larger gating effects. Similar to the previous experiment, persistent magnetization switchings are observed with short voltage pulses, with the dominant effect being a suppression of the magnitude of K_c with depletion of the epilayer. An interesting but unexpected difference on the effect of gating on AMR is observed with the top and back-gating: the magnitude of AMR increases with depletion of holes using the top-gate but decreases with depletion using the bottom-gate. This reflects the inhomogeneity of the (Ga,Mn)As epilayer used. In addition, the diminished gating effects for the electric double layer (EDL) gating is a result of the use of the 2 nm thick insulating GaAs protective layer on top of the (Ga,Mn)As. Overall, the effects achieved by electrical gating on the (Ga,Mn)As epilayer is enhanced in using the double-gating method.

7.2 Outlook and Future Work

Here, focus turns to potential future work based on the effects of electric gating on the magnetic properties of (Ga,Mn)As. Some of the experimental techniques used (for example ionic-gel gating) can also be extended to other material systems.

7.2.1 Voltage-pulse magnetization switching

Chapter 5 demonstrated the effects of gating on the magnetic crystalline anisotropy of (Ga,Mn)As. This can be utilized as an external electrical means to manipulate the direction of magnetization (also supported by another independent work by Chiba and co-workers [75]). The switching of magnetization between easy axes adds a non-volatile device function to the present device, where only the application of an electric field is required to control the direction of magnetization. In addition to manipulating the direction of magnetization with an electric field, the persistent magnetization switching shown with a voltage pulse can also form the basis of fast magnetization switching for a spin-transistor, as a low-power alternative to magnetization switching with a current-generated magnetic field (Oersted-Ampère field) via spin-transfer torque (STT) [79].

Apart from varying the carrier concentration in the DMS material, combined magneto- and electrostrictive effects can also be considered. An initial step to achieve a spin-transistor device could be coupled with the use of strain in a controllable and reversible way by mechanically coupling the samples to piezoelectric actuators [15,80]. The anisotropy can be pre-set to a tipping point which allows for fast magnetization switching with a gate-voltage pulse.

7.2.2 Electrolyte-gating

Further work can be done with the ionic gel gating on (Ga,Mn)As (also supported by recent similar work by Endo and co-workers [81]) such as the optimization of the technique as well as attaining a better understanding of the electrochemical reactions and other processes going on at the interface between (Ga,Mn)As and the electrolytes during gating. A larger modulation of holes can result in a larger modulation of magnetism, which is useful in the understanding of the mechanism of carrier-dependent magnetic properties in (Ga,Mn)As as well as other magnetic semiconductors. It can also be a very useful handle to investigate other physical phenomena such as the effects of gating in the vicinity of the metal-insulator transition, or the study of Rashba effects in spin-transistors.

Appendix A

Fabrication steps

A.1 Processes for fabrication of FET

1. Clean substrate by immersing it in an ultrasonic bath first in acetone, followed by IPA for 5 minutes each

A.1.1 Mesa

1. Pre-bake 15 minutes at 120 °C
2. Spinning of resist: UV-III photo-resist for 40 seconds at 5000 rpm
3. Pre-bake for 1 minute at 155 °C on a thermal hot plate
4. Photo-lithography with exposure for 2 minutes
5. Post-bake for 1 minute at 155 °C on a thermal hot plate
6. Resist development: 30 seconds at 20 °C in CD-26 developer. Rinse with water after and blow dry with N₂ gas
7. Wet etching using H₃PO₄:H₂O:H₂O₂ in the proportion of 1:40:10. Immerse sample in etchant for 10 seconds, then rinse thoroughly in deionized H₂O.

A.1.2 Bond Pads

1. Pre-bake 15 minutes at 120 °C
2. Spinning of resist: UV-III photo-resist for 40 seconds at 5000 rpm
3. Pre-bake for 1 minute at 155 °C on a thermal hot plate
4. Photo-lithography with exposure for 2 minutes
5. Post-bake for 1 minute at 155 °C on a thermal hot plate
6. Resist development: 30 seconds at 20 °C in CD-26 developer. Rinse with water after and blow dry with N₂ gas

7. Prepare samples for evaporation by: Removing waste resist left on surface using Oxygen Plasma for 30 seconds followed by HCl : H₂O (1:10) for 30 seconds, rinsed in de-ionized H₂O
8. Evaporation: Cr: 30 nm at rate 0.1 nm/s Au: 300 nm at rate 0.2 nm/s
9. Lift-off: 2 hours in a bath of acetone. After successful lift-off, rinse in IPA and blow dry with N₂ gas

A.1.3 Scribing and Packaging

1. Pre-bake for 5 minutes at 120 °C
2. Spinning of resist: PMMA A4 (MW = 950 K) for 40 seconds at 5000 rpm
3. Post-bake for 2 hours at 80 °C
4. Scribing
5. Packaging: Device glued with Ag Dag or UV-III onto 20 pins standard packages
6. Post-bake for 30 minutes at 80 °C
7. Bonding with Au wires

Appendix B

Publications

-
- [1] *Enhanced annealing, high Curie temperature, and low-voltage gating in (Ga,Mn)As: A surface oxide control study*, K. Olejník, **M. H. S. Owen**, V. Novák, J. Mašek, A. C. Irvine, J. Wunderlich and T. Jungwirth, *Physical Review B*, 78, 054403 (2008)
- [2] *Low-voltage control of ferromagnetism in a semiconductor pn junction*, **M. H. S. Owen**, J. Wunderlich, V. Novák, K. Olejník, J. Zemen, K. Vybírný, S. Ogawa, A. C. Irvine, A. J. Ferguson, H. Siringhaus, T. Jungwirth, *New Journal of Physics*, 11, 023008 (2009)

Bibliography

- [1] Ohno, H., Chiba, D., Matsukura, F., Omiya, T., Abe, E., Dietl, T., Ohno, Y., and Ohtani, K. *Nature* **408**(6815), 944–946 (2000).
- [2] Chiba, D., Yamanouchi, M., Matsukura, F., and Ohno, H. *Science* **301**(5635), 943–945 (2003).
- [3] Chiba, D., Matsukura, F., and Ohno, H. *Applied Physics Letters* **89**(16), 162505 (2006).
- [4] Olejník, K., Owen, M. H. S., Novák, V., Mašek, J., Irvine, A. C., Wunderlich, J., and Jungwirth, T. *Physical Review B* **78**, 054403 (2008).
- [5] Owen, M. H. S., Wunderlich, J., Novak, V., Olejnik, K., Zemen, J., Vyborny, K., Ogawa, S., Irvine, A. C., Ferguson, A. J., Siringhaus, H., and Jungwirth, T. *New Journal of Physics* **11**(6), 023008 (2009).
- [6] Hoddeson, L., Braun, E., Teichmann, J., and Weart, S. *Oxford University Press* (1992).
- [7] Edmonds, K. W., Wang, K. Y., Champion, R. P., Neumann, A. C., Farley, N. R. S., Gallagher, B. L., and Foxon, C. T. *Applied Physics Letters* **81**(26), 4991–4993 (2002).
- [8] Ku, K. C., Potashnik, S. J., Wang, R. F., Chun, S. H., Schiffer, P., Samarth, N., Seong, M. J., Mascarenhas, A., Johnston-Halperin, E., Myers, R. C., Gossard, A. C., and Awschalom, D. D. *Applied Physics Letters* **82**(14), 2302–2304 (2003).

- [9] Gould, C., Ruster, C., Jungwirth, T., Girgis, E., Schott, G. M., Giraud, R., Brunner, K., Schmidt, G., and Molenkamp, L. W. *Physical Review Letters* **93**(11), 117203 (2004).
- [10] Giddings, A. D., Khalid, M. N., Jungwirth, T., Wunderlich, J., Yasin, S., Campion, R. P., Edmonds, K. W., Sinova, J., Ito, K., Wang, K. Y., Williams, D., Gallagher, B. L., and Foxon, C. T. *Physical Review Letters* **94**(12), 127202 (2005).
- [11] Ruster, C., Gould, C., Jungwirth, T., Sinova, J., Schott, G. M., Giraud, R., Brunner, K., Schmidt, G., and Molenkamp, L. W. *Physical Review Letters* **94**(2), 027203 (2005).
- [12] Pappert, K., Schmidt, M. J., Humpfner, S., Ruster, C., Schott, G. M., Brunner, K., Gould, C., Schmidt, G., and Molenkamp, L. W. *Physical Review Letters* **97**(18), 186402 (2006).
- [13] Wunderlich, J., Jungwirth, T., Kaestner, B., Irvine, A. C., Shick, A. B., Stone, N., Wang, K. Y., Rana, U., Giddings, A. D., Foxon, C. T., Campion, R. P., Williams, D. A., and Gallagher, B. L. *Physical Review Letters* **97**(7), 077201 (2006).
- [14] Wunderlich, J., Irvine, A. C., Zemen, J., Holy, V., Rushforth, A. W., De-Ranieri, E., Rana, U., Vyborny, K., Sinova, J., Foxon, C. T., Campion, R. P., Williams, D. A., Gallagher, B. L., and Jungwirth, T. *Phys. Rev. B* **76**, 054424 (2007).
- [15] De-Ranieri, E., Rushforth, A. W., Vyborny, K., Rana, U., Ahmad, E., Campion, R. P., Foxon, C. T., Gallagher, B. L., Irvine, A. C., Wunderlich, J., and Jungwirth, T. *New Journal of Physics* **10**(6), 065003 (2008).
- [16] Furdyna, J. K. *J. Appl. Phys.* **64**, R29 (1988).
- [17] Munekata, H., Ohno, H., Vonmolnar, S., Segmuller, A., Chang, L. L., and Esaki, L. *Physical Review Letters* **63**(17), 1849–1852 (1989).

- [18] Ohno, H., Shen, A., Matsukura, F., Oiwa, A., Endo, A., Katsumoto, S., and Iye, Y. *Applied Physics Letters* **69**(3), 363–365 (1996).
- [19] Liu, X., Sasaki, Y., and Furdyna, J. K. *Physical Review B* **67**(20), 205204 (2003).
- [20] Jungwirth, T., Sinova, J., Masek, J., Kucera, J., and MacDonald, A. H. *Reviews of Modern Physics* **78**(3), 809–864 (2006).
- [21] Yu, Z. G. and Flatte, M. E. *Physical Review B* **66**(23), 235302 (2002).
- [22] Chiba, D., Takamura, K., Matsukura, F., and Ohno, H. *Applied Physics Letters* **82**(18), 3020–3022 (2003).
- [23] Yu, K. M., Walukiewicz, W., Wojtowicz, T., Denlinger, J., Scarpulla, M. A., Liu, X., and Furdyna, J. K. *Appl. Phys. Lett.* **86**, 042102 (2005).
- [24] Edmonds, K. W., Boguslawski, P., Wang, K. Y., Campion, R. P., Novikov, S. N., Farley, N. R. S., Gallagher, B. L., Foxon, C. T., Sawicki, M., Dietl, T., Nardelli, M. B., and Bernholc, J. *Physical Review Letters* **92**(3), 037201 (2004).
- [25] Maca, F. and Masek, J. *Physical Review B* **65**(23), 235209 (2002).
- [26] Blinowski, J. and Kacman, P. *Physical Review B* **67**(12), 121204 (2003).
- [27] Edmonds, K. W., Farley, N. R. S., Johal, T. K., van der Laan, G., Campion, R. P., Gallagher, B. L., and Foxon, C. T. *Physical Review B* **71**(6), 064418 (2005).
- [28] Masek, J., Kudrnovsky, J., and Maca, F. *Physical Review B* **67**(15), 153203 (2003).
- [29] Bliss, D. E., Walukiewicz, W., Ager, J. W., Haller, E. E., Chan, K. T., and Tanigawa, S. *Journal of Applied Physics* **71**(4), 1699–1707 (1992).
- [30] De Boeck, J., Oesterholt, R., Bender, H., Van Esch, A., Bruynseraede, C., Van Hoof, C., and Borghs, G. *J. Magn. Magn. Mater.* **156**, 148 (1996).

- [31] Champion, R. P., Edmonds, K. W., Zhao, L. X., Wang, K. Y., Foxon, C. T., Gallagher, B. L., and Staddon, C. R. *Journal of Crystal Growth* **247**(1-2), 42–48 (2003).
- [32] Hayashi, T., Hashimoto, Y., Katsumoto, S., and Iye, Y. *Applied Physics Letters* **78**(12), 1691–1693 (2001).
- [33] Potashnik, S. J., Ku, K. C., Chun, S. H., Berry, J. J., Samarth, N., and Schiffer, P. *Applied Physics Letters* **79**(10), 1495–1497 (2001).
- [34] Potashnik, S. J., Ku, K. C., Mahendiran, R., Chun, S. H., Wang, R. F., Samarth, N., and Schiffer, P. *Physical Review B* **66**(1), 012408 (2002).
- [35] Dietl, T., Ohno, H., and Matsukura, F. *Phys. Rev. B* **63**, 195205 (2001).
- [36] Bhattacharjee, A. K., Fishman, G., and Coqblin, B. *Physica B+C* **117-118**, 449 (1983).
- [37] Okabayashi, J., Kimura, A., Rader, O., Mizokawa, T., Fujimori, A., Hayashi, T., and Tanaka, M. *Phys. Rev. B* **58**, R4211 (1998).
- [38] Pashitskii, E. A. and Ryabchenko, S. M. *Fizika Tverdogo Tela* **21**(2), 545–547 (1979).
- [39] Champion, R. P., Edmonds, K. W., Zhao, L. X., Wang, K. Y., Foxon, C. T., Gallagher, B. L., and Staddon, C. R. *Journal of Crystal Growth* **251**(1-4), 311–316 (2003).
- [40] Ohno, H. *Journal of Magnetism and Magnetic Materials* **200**(1-3), 110–129 (1999).
- [41] Krstajic, P. M., Peeters, F. M., Ivanov, V. A., Fleurov, V., and Kikoin, K. *Physical Review B* **70**(19), 195215 (2004).
- [42] Dietl, T., Haury, A., and dAubigne, Y. M. *Physical Review B* **55**(6), R3347–R3350 (1997).

- [43] Dietl, T., Ohno, H., Matsukura, F., Cibert, J., and Ferrand, D. *Science* **287**(5455), 1019–1022.
- [44] Jungwirth, T., Atkinson, W. A., Lee, B. H., and MacDonald, A. H. *Physical Review B* **59**(15), 9818–9821 (1999).
- [45] Matsukura, F., Ohno, H., Shen, A., and Sugawara, Y. *Physical Review B* **57**(4), R2037–R2040 (1998).
- [46] Sawicki, M., Matsukura, F., Idziaszek, A., Dietl, T., Schott, G. M., Ruester, C., Gould, C., Karczewski, G., Schmidt, G., and Molenkamp, L. W. *Physical Review B* **70**(24), 245325 (2004).
- [47] Yu, K. M., Walukiewicz, W., Wojtowicz, T., Kuryliszyn, I., Liu, X., Sasaki, Y., and Furdyna, J. K. *Phys. Rev. B* **65**, 201303 (2002).
- [48] Sawicki, M., Wang, K. Y., Edmonds, K. W., Campion, R. P., Staddon, C. R., Farley, N. R. S., Foxon, C. T., Papis, E., Kaminska, E., Piotrowska, A., Dietl, T., and Gallagher, B. L. *Physical Review B* **71**(12), 121302 (2005).
- [49] Abolfath, M., Jungwirth, T., Brum, J., and MacDonald, A. H. *Physical Review B* **63**05(5), 054418 (2001).
- [50] Masmanidis, S. C., Tang, H. X., Myers, E. B., Li, M., De Greve, K., Vermeulen, G., Van Roy, W., and Roukes, M. L. *Physical Review Letters* **95**(18), 187206 (2005).
- [51] O’Handley, R. C. *Modern Magnetic Materials: Principles and Applications*. Wiley-Interscience, 1st edition, (2000).
- [52] Gould, C., Pappert, K., Schmidt, G., and Molenkamp, L. *Advanced Materials* **19**, 323 (2007).
- [53] Omiya, T., Matsukura, F., Dietl, T., Ohno, Y., Sakon, T., Motokawa, M., and Ohno, H. *Physica E* **7**, 976 (2000).

- [54] Edmonds, K. W., Champion, R. P., Wang, K. Y., Neumann, A. C., Gallagher, B. L., Foxon, C. T., and Main, P. C. *Journal of Applied Physics* **93**(10), 6787–6789 (2003).
- [55] Iye, Y., Oiwa, A., Endo, A., Katsumoto, S., Matsukura, F., Shen, A., Ohno, H., and Munekata, H. *Mat. Sci. Eng. B* **63**, 88 (1999).
- [56] Matsukura, F., Sawicki, M., Dietl, T., Chiba, D., and Ohno, H. *Physica E* **21**, 1032 (2004).
- [57] Baxter, D. V., Ruzmetov, D., Scherschligt, J., Sasaki, Y., Liu, X., Furdyna, J. K., and Mielke, C. H. *Phys. Rev. B* **65**, 212407 (2002).
- [58] Rushforth, A. W., Výborný, K., King, C. S., Edmonds, K. W., Champion, R. P., Foxon, C. T., Wunderlich, J., Irvine, A. C., Vašek, P., Novák, V., Olejník, K., Sinova, J., Jungwirth, T., and Gallagher, B. L. *Phys. Rev. Lett.* **99**, 147207 (2007).
- [59] Rushforth, A., Vyborny, K., King, C., Edmonds, K., Champion, R., Foxon, C., Wunderlich, J., Irvine, A., Novak, V., Olejnyk, K., Kovalev, A., Sinova, J., T.Jungwirth, and B.L.Gallagher. *Jour. Magn. Magn. Mat.* **321**, 1001 – 1008 (2009).
- [60] Döring, W. *Ann. Phys. (Leipzig)* **424**, 259 (1938).
- [61] Jungwirth, T., Abolfath, M., Sinova, J., Kučera, J., and MacDonald, A. H. *Appl. Phys. Lett.* **81**, 4029 (2002).
- [62] Wang, K. Y., Edmonds, K. W., Champion, R. P., Zhao, L. X., Foxon, C. T., and Gallagher, B. L. *Phys. Rev. B* **72**, 085201 (2005).
- [63] Sze, S. M. and Ng, K. K. *Physics of Semiconductor Devices*. Wiley-Interscience, 3rd edition, (2007).
- [64] Van Zeghbroeck, B. *Principles of Semiconductor Devices*. <http://ece-www.colorado.edu/~bart/book/>.

- [65] Weisheit, M., Fahler, S., Marty, A., Souche, Y., Poinsignon, C., and Givord, D. *Science* **315**(5810), 349–351 (2007).
- [66] Cho, J. H., Lee, J., Xia, Y., Kim, B., He, Y., Renn, M. J., Lodge, T. P., and Frisbie, C. D. *Nature Materials* **7**, 900–906 (2008).
- [67] Panzer, M. J. and Frisbie, C. D. *J. AM. CHEM. SOC.* **129**, 6599 (2007).
- [68] Cho, J. H., Lee, J., He, Y., Kim, B., Lodge, T. P., and Frisbie, C. D. *Advanced Materials* **20**, 686–690 (2008).
- [69] Xia, Y., Cho, J. H., Lee, J., Ruden, P. P., and Frisbie, C. D. *Advanced Materials* **21**, 2174 (2009).
- [70] Novák, V., Olejník, K., Wunderlich, J., Cukr, M., Výborný, K., Rushforth, A. W., Edmonds, K. W., Campion, R. P., Gallagher, B. L., Sinova, J., and Jungwirth, T. *Physical Review Letters* **101**, 077201 (2008).
- [71] Wang, K. Y., Campion, R. P., Edmonds, K. W., Sawicki, M., Dietl, T., Foxon, C. T., and Gallagher, B. L. In *Proceedings of the 27th International Conference on the Physics of Semiconductors*, de Walle, J. M. C. G. V., editor, volume 772 of *AIP Conference Proceedings*, 333. AIP, (2005).
- [72] Wang, K. Y., Edmonds, K. W., Campion, R. P., Gallagher, B. L., Farley, N. R. S., Foxon, T., Sawicki, M., Boguslawski, P., and Dietl, T. *J. Appl. Phys.* **95**, 6512 (2005).
- [73] Gennes, P. G. D. and Friedel, J. *J. Phys. Chem. Sol.* **4**, 71 – 77 (1958).
- [74] Fisher, M. E. and Langer, J. S. *Phys. Rev. Lett.* **20**, 665 (1968).
- [75] Chiba, D., Sawicki, M., Nishitani, Y., Nakatani, Y., Matsukura, F., and Ohno, H. *Nature* **455**, 515 (2008).
- [76] Matsukura, F., Ohno, H., and Dietl, T. In *Handbook of Magnetic Materials*, Buschow, K. H. J., editor, volume 14. Elsevier, Amsterdam (2002).

-
- [77] Jungwirth, T., Sinova, J., MacDonald, A. H., Gallagher, B. L., Novák, V., Edmonds, K. W., Rushforth, A. W., Champion, R. P., Foxon, C. T., Eaves, L., Olejník, K., Mašek, J., Yang, S. R. E., Wunderlich, J., Gould, C., Molenkamp, L. W., Dietl, T., and Ohno, H. *Phys. Rev. B* **76**, 125206 (2007).
- [78] Stolichnov, I., Riester, S. W. E., Trodahl, H. J., Setter, N., Rushforth, A. W., Edmonds, K. W., Champion, R. P., Foxon, C. T., Gallagher, B. L., and Jungwirth, T. *Nature Materials* **7**, 464 (2008).
- [79] Slonczewski, J. C. *J. Magn. Magn. Mater.* **159**, L1 (1996).
- [80] Rushforth, A. W., De-Ranieri, E., Zemen, J., Wunderlich, J., Edmonds, K. W., King, C. S., Ahmad, E., Champion, R. P., Foxon, C. T., Gallagher, B. L., Vyborny, K., KuCera, J., and Jungwirth, T. *Phys. Rev. B* **78**, 085314 (2008).
- [81] Endo, M., Chiba, D., Shimotani, H., Matsukura, F., Iwasa, Y., and Ohno, H. *Applied Physics Letters* **96**, 022515 (2010).